STUDY OF SPIN CURRENT EFFECT IN METALLIC ANTIFERROMAGNET AND HEAVY METAL HETEROSTRUCTURES

Yang Yumeng

NATIONAL UNIVERSITY OF SINGAPORE

2016

STUDY OF SPIN CURRENT EFFECT IN METALLIC ANTIFERROMAGNET AND HEAVY METAL HETEROSTRUCTURES

Yang Yumeng

(B. Sci., Sichuan University)

A THESIS SUBMITTED FOR THE DEGREE

OF DOCTOR OF PHILOSOPHY

DEPARTMENT OF ELECTRICAL AND

COMPUTER ENGINEERING

NATIONAL UNIVERSITY OF SINGAPORE

2016

Supervisions:
Professor Wu Yihong, Main Supervisor
Dr Yao Kui, Co-Supervisor

Examiners:
Associate Professor Liang Gengchiau
Associate Professor Zhu Chunxiang
Professor Teruo Ono, Kyoto University

DECLARATION

I hereby declare that this thesis is my original work and it has been written by me in its entirety. I have duly acknowledged all the sources of information which have been used in the thesis.

This thesis has also not been submitted for any degree in any university previously.

杨雨梦

Yang Yumeng

20 September 2016

ACKNOWLEDGMENTS

This dissertation is a compilation of countless hours of hard work, not just by me, but also by many others who have provided me valuable advice and help. The work presented in this dissertation could not be possible without them.

First, I would like to thank my supervisor, Prof. Wu Yihong for his guidance and support over the past few years. Looking back, I started out as a fresh graduate with little background in magnetism. It is Prof. Wu who spent a great deal of time teaching me step by step the fundamentals in the field of magnetism. His knowledge, passion, altitude and devotion in research has inspired me in many ways in the past and surely will benefit me in more ways in the future.

Second, I would like to thank my co-supervisor, Dr. Yao Kui from Institute of Materials Research and Engineering (IMRE) for his help in data analysis, and support in equipment access. In particular, the regular discussions with him over the years often inspired me to look at problems from another perspective, and reconsider the possible solutions. At the same time, I am also indebted to many staffs at IMRE for their kind support, especially Dr. Santiranjan Shannigrahi, Dr. Ji Wei and Dr. Meysam Sharifzadeh Mirshekarloo for their help in performing low temperature transport measurement and X-ray diffraction measurement.

Third, my great appreciation goes to all my group mates and colleagues in Information Storage Materials Laboratory for their consistent and tremendous help. I am grateful to Dr. Wu Baolei, Dr. Zhang Chi and Dr. Wang Ying for the training on the various equipment in the lab; Mr. Ruan Xiaofan,

Dr. Shimon and Dr. Wang Ying for the teaching of many useful software. I also feel lucky to have Mr. Xu Yanjun, Mr. Qi Long, Mr. Zhang Xiaoshan and Ms. Luo Ziyan as group mates to work together. I would also like to thank the lab technicians, Ms. Loh Fong Leong and Ms. Xiao Yun for their support in purchasing the necessary consumables and equipment.

Fourthly, I would like to thank the entertainment and accompany of many friends since I started my PhD: Mr. Sun Bo, Mr. Chen Gong, Mr. Teng Yanbo for sharing an apartment; Dr. Wu Yang, Dr. Qiu Xuepeng and Dr. Liu Xinming for occasionally playing basketball.

Last, I am proud to have my parents Yang Dongnan and Shen Tao, and my girlfriend Sun Yu, all of whom understood, trusted and supported me during my PhD period. Their caring love is indeed the greatest fortune in my life.

Table of Contents

Summary

Antiferromagnet (AF) has recently regained an increasing interest as a potential active element for spintronic devices. Featuring negligible stray field, large anisotropy and fast spin dynamics, the AFs can potentially lead to devices with improved performances as compared to their ferromagnet (FM) counterparts. Before reaping these benefits, a key question needs to be answered is whether the AF spin states can be altered and detected like the FM. Apart from current-induced Oersted field, spin transfer torque (STT) and spin orbit torque (SOT) can be potentially utilized to change the spin states of AFs. However, unlike FMs, experimental studies on the interactions between non-equilibrium spins or spin current (the origin of STT and SOT) with AFs are still quite limited.

In this dissertation, we present a systematic study of the interactions between spin current generated by Pt, a heavy metal (HM) with strong spin-orbit coupling, and FeMn, a commonly used AF, in both FeMn/Pt bilayers and $[FeMn/Pt]_n$ multilayers. First, a large field-like SOT effective field of 2.05×10^{-5} - 2.44×10^{-5} Oe (A^{-1} cm^2) is observed in FeMn/Pt bilayers with a FeMn thickness of 2 - 5 nm, as revealed by 2nd order planar Hall effect (PHE) measurements. The large magnitude of the effective field corroborates the spin Hall origin, considering the much smaller uncompensated net moment in FeMn. The efficient absorption of spin current by FeMn is further affirmed by the fact that spin current generated by Pt in NiFe/FeMn/Pt trilayers can only travel through FeMn within a thickness of 1 – 4 nm.

Second, a sizable spin Hall magnetoresistance (SMR) is observed in FeMn/Pt bilayers, which further confirms the presence of SOT effect

considering the common origin of SMR and SOT. The dependence of SMR on FeMn thickness is different from that of NiFe thickness dependence in NiFe/Pt bilayers, which is attributed to the thickness dependent net magnetization in FeMn. Through analysis of the Pt thickness dependence of SMR, we were able to extract the spin Hall angle and spin diffusion length of Pt as well as the real part of spin mixing conductance of FeMn/Pt interface, and the values are 0.2, 1.1 nm, and $5.5 \times 10^{14}\ \Omega^{-1}\ \mathrm{m}^{-2}$, respectively.

In the last part of this dissertation, we extend the study to $[\mathrm{FeMn/Pt}]_n$ multilayers with ultrathin FeMn and Pt layers. It is found that multilayers with properly chosen thickness combinations exhibit global FM order above room temperature. We further demonstrate that a large field-like SOT effective field can be induced by a charge current passing through the multilayers without the need for an additional thick HM layer. The SOT effect can be accounted for by the combined action of spin current generation in Pt layers and absorption in the neighboring FeMn layers. The SOT is able to rotate the magnetization of the multilayer by 360° without the need for any external field.

The findings obtained in this work shall stimulate further studies on spin current transport and related phenomenon in AFs with different types of crystalline and spin structures, which have potential applications in next-generation spintronic devices.

List of Tables

List of Figures

List of Symbols and Abbreviations

AF	Antiferromagnet
AFM	Atomic force microscopy
AHE	Anomalous Hall effect
AMR	Anisotropic magnetoresistance
CMOS	Complementary metal-oxide
DMS	Dilute magnetic semiconductor
FM	Ferromagnet
GMR	Giant magnetoresistance
HDD	Hard drive disk
HM	Heavy metal
MOKE	Magnetic Kerr effect
MRAM	Magnetoresistive randam access memory
MTJ	Magnetic tunnel junction
OHE	Ordinary Hall effect
OMR	Ordinary magnetoresistance
OOMMF	Object oriented micromagnetic framework
PHE	Planar Hall effect
SHE	Spin Hall effect
SMR	Spin Hall magnetoresistance
SOC	Spin orbit coupling
SOT	Spin orbit torque
STT	Spin transfer torque
TMR	Tunneling magnetoresistance
VSM	Vibrating sample magnetometer

H_A	Anisotropy field
H_{DL}	Antidamping-like effective field
H_c	Coercivity
T_C	Curie temperature
j	Current density
H_I	Current induced magnetic field
P_C	Current spin polarization
m_e	Electron mass
H_{eb}	Exchange bias
J	Exchange coupling constant
H_{ex}	Exchange coupling field
H_{FL}	Field-like effective field
E	Free energy density
γ	Gyromagnetic ratio
T_N	Néel temperature
H_{Oe}	Oersted field
$\hbar$	Planck constant
R	Resistance
ρ	Resistivity
M_s	Saturation magnetization
μ	Spin-dependent electrochemical potential
λ	Spin diffusion length
θ_{SH}	Spin Hall angle
G_{MIX}	Spin mixing conductance
d	Thickness

List of Publications

Journal publications:

1. Y. Yang, Y. Xu, X. Zhang, Y. Wang, S. Zhang, R.-W. Li, M. S. Mirshekarloo, K. Yao, and Y. H. Wu, *Fieldlike spin-orbit torque in ultrathin polycrystalline FeMn films*, Physical Review B 93, 094402 (2016).
2. Y. Xu, Y. Yang, K. Yao, B. Xu, and Y. H. Wu, *Self-current induced spin-orbit torque in FeMn/Pt multilayers*, Scientific Reports 6, 26180 (2016)
3. Y. Yang, Y. Xu, K. Yao, and Y. H. Wu, *Thickness dependence of spin Hall magnetoresistance in FeMn/Pt bilayers*, AIP Advances 6, 065203 (2016);

Conference publications:

1. Y. Yang, B. L. Wu, K. Yao, S. Shannigrahi, B. Zong, Y. H. Wu, *Investigation of magnetic proximity effect in Ta/YIG bilayer Hall bar structure*, 58th Annual Conference on Magnetism and Magnetic Materials, Denver, Colorado, 4 – 8 November, 2013 (Poster).
2. Y. Yang, X. Zhang, Y. Wang, K. Yao, Y. H. Wu, *Investigation of Spin-orbit Effect in Pt/NiFe/Ta, Pt/NiFe/Pt and Ta/NiFe/Ta Trilayers*, 59th Annual Conference on Magnetism and Magnetic Materials, Honolulu, Hawaii, 3 – 7 November, 2014 (Poster).
3. Y. Yang, X. Zhang, Y. Xu, S. Zhang, R. -W. Li, K. Yao and Y. H. Wu, *Spin orbit torque effect in Pt/FeMn bilayers*, IEEE International Magnetics Conference, Beijing, China, 11 – 15 May, 2015 (Oral).
4. Y. Yang, Y. Xu, S. Zhang, R. -W. Li, K. Yao, and Y. H. Wu, *Field-like spin orbit torque in ultra-thin polycrystalline FeMn films*, International Union

of Materials Research Societies- International Conference on Electronic Materials, Singapore, 4 – 8 July, 2016 (Oral).

Other journal publications:

1. Y. Wang, Y. Yang, Z. Zhao, C. Zhang, and Y. H. Wu, *Local electron field emission study of two-dimensional carbon*, Applied Physics Letters 103, 033115 (2013).
2. B. L. Wu, Y. Yang, Z. B. Guo, Y. H. Wu, and J. J. Qiu, *Suppression of superconductivity in Nb by IrMn in IrMn/Nb bilayers*, Applied Physics Letters 103, 152602 (2013).
3. Y. Yang, B. L. Wu, K. Yao, S. Shannigrahi, B. Zong, and Y. Wu, *Investigation of magnetic proximity effect in Ta/YIG bilayer Hall bar structure*, Journal of Applied Physics 115, 17C509 (2014).
4. Z. X. Chen, Z. Fang, Y. Wang, Y. Yang, A. Kamath, X. P. Wang, N. Singh, G. -Q. Lo, D. -L. Kwong, and Y. H. Wu, *Impact of Ni Concentration on the Performance of Ni Silicide/*HfO_2*/TiN Resistive RAM (RRAM) Cells*, Journal of Electronic Materials 43, 4193 (2014).
5. Y. Wang, Y. Yang, and Y. H. Wu, *Dynamic control of local field emission current from carbon nanowalls*, Journal of Vacuum Science & Technology B 32, 051803 (2014).
6. Y. Wang, J. Chai, S. Wang, L. Qi, Y. Yang, Y. Xu, H. Tanaka, and Y. H. Wu, *Electrical oscillation in Pt/VO2 bilayer strips*, Journal of Applied Physics 117, 064502 (2015).

Other conference publications:

5. Y. H. Wu, Y. Wang, Y. Yang and C. Zhang, *Edge-contact and field emission study of two-dimensional carbon using a nanoprobe*, IOP Workshop 2013, Beijing, China, 18 – 19 July, 2013.

Chapter 1 Introduction

1.1 Ferromagnet spintronics

As the continuous downscaling of complementary metal-oxide-semiconductor (CMOS) technology begins to face significant challenges,[1] over the past decades, considerable research efforts have been made to explore device technologies that can serve as an alternative for or complementary to the CMOS technology. One of the possible pathways is spintronics, which makes use of spin degree of freedom of electron rather than charge only as in conventional electronic devices. While the study of spin-related phenomena in semiconductors and metals dates back to 1970s,[2] it was the discovery of giant magnetoresistance (GMR) effect in 1988[3,4] that formally started a new research field called spintronics. As illustrated in Fig. 1.1, the GMR effect has its origin in spin-dependent transport in ferromagnet (FM)/non-magnet (NM) superlattice structures. The resistance of the multilayer is low when magnetizations of the FM layers are aligned in parallel and high when they are aligned in anti-parallel. As the difference is much higher than that caused by the anisotropic magneto-resistance (AMR) effect in a single layer of FM, it was termed “giant” magneto-resistance. The discovery of GMR immediately attracted the interest of hard disk (HDD) industry because of its immense potential as a sensitive sensor. A variation of the GMR structure, which is more suitable for low-field applications, is the exchange-biased spin-valve (SV). The SV, which was invented by IBM in 1991,[5] was quickly developed into a viable technology and adopted in the hard disk drives in 1997.[6] This has enabled the areal density of HDD to increase by a compound annual growth rate of about 60% for almost two decades.[7,8] In addition to magnetic sensors, efforts have also been made to exploit the SV technology for applications in magnetic random access memory (MRAM),[9] in which the parallel and anti-parallel alignments of two FM layers separated by an NM layer are used to store “1” and “0” in a non-volatile fashion. Compared to other types of non-volatile memories, the MRAM is fast and has almost infinite number of read-write cycles.

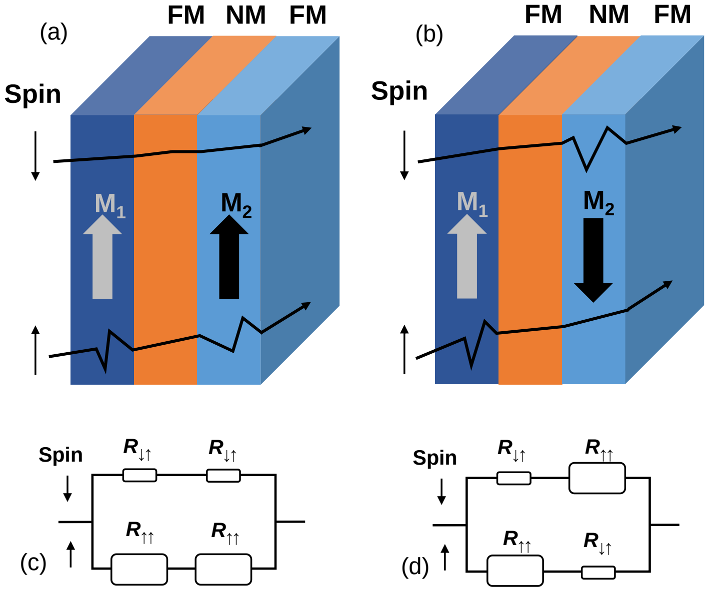

FIG. 1.1 (a) and (b), schematics of current in GMR device with two FM layers of (a) parallel magnetization configuration and (b) antiparallel magnetization configuration; (c) and (d), simplified equivalent circuit of the device in parallel configuration (c) and antiparallel configuration (d). Figure adapted from Ref. [8].

Stimulated by the discovery of GMR effect, there was a renewed interest in magnetic tunnel junctions (MTJ), which was originally discovered by M. Jullière in Fe/Ge-O/Co junctions in 1975.[10] The original device had a tunnel magnetoresistance (TMR) ratio of about 14% at 4.2 K. By replacing the Ge-O barrier with amorphous aluminum oxide, T. Miyazaki[11] and J. Moodera[12] found a TMR ratio of 18% and 11.8% in Fe/AlO_x/Fe and in CoFe/AlO_x/Co junctions, respectively, in 1995. Follow-up improvement on the electrodes materials and barrier formation process successfully boosted the TMR to 70%.[13] In addition to its large TMR ratio, the current-perpendicular-to-plane (CPP) design of MTJ brings it significant advantages as both a sensing and memory device as compared to the current-in-plane (CIP) spin-valves. The advantages of MTJ were further boosted with the advent of MTJs using crystalline MgO barrier. In 2001, a number of theoretical predictions[14,15] suggested extremely high TMR in MTJs in lattice-matched and well-ordered Fe/MgO/Fe junctions due to excellent "spin filter" property of the Fe/MgO interface. Soon after these theoretical works, two groups[16,17] reported experimental realization of crystalline MgO-based MTJs with a TMR ratio of 180% and 220% at room temperature, respectively. Nowadays, more than a few hundred percent of the TMR ratio can be readily achieved in MgO-based MTJ with various electrodes,[18-21] with the highest TMR ratio up to 604%.[22] With its large signal and good impedance compatibility with CMOS, the MgO-based MTJ is enroute to become a universal building block for spintronic applications.

Another significant development in the field of spintronics is the theoretical prediction of spin transfer torque (STT) in magnetic materials and structures with non-collinear magnetization configuration in 1996 by J. C. Slonczewski[23] and L. Berger[24] and subsequent experimental verifications by several groups.[25-27] This development was significant because, up till then, Oersted field was the only mechanism for magnetization switching in spintronic devices. The situation changed completely with the emergence of STT, which made it possible for the first time to switch the magnetization of a magnet by a current directly without the need to convert it to an Oersted field. Although the STT has been realized in a variety of systems including point contacts,[25,27] nanopillars,[28,29] nanowires,[30] spin valves,[31,32] and MTJs,[33,34] its underlying principle is the same, which is best understood using the trilayer structure shown in Fig. 1.2. The typical trilayer structure consists of a fixed and a free FM layer separated by a non-magnetic conductor. When electric current passes through the fixed FM layer, it becomes spin polarized with the electron spin polarization determined by the magnetization direction of the fixed layer. Upon entering the free layer (*i.e.*, electrons move from fixed layer to free layer), the non-equilibrium electron spin will precess around the exchange field from the local magnetic moment of the free layer. During this process, the transverse non-equilibrium moment will be averaged out quickly. Based on the principle of momentum conservation, the transverse moment of polarized electron is absorbed by the free FM, leading to the rotation of its magnetization. To switch back to the original state, one just needs to change the current direction such that electrons reflected back from the fixed layer will cause the switching of the free layer.

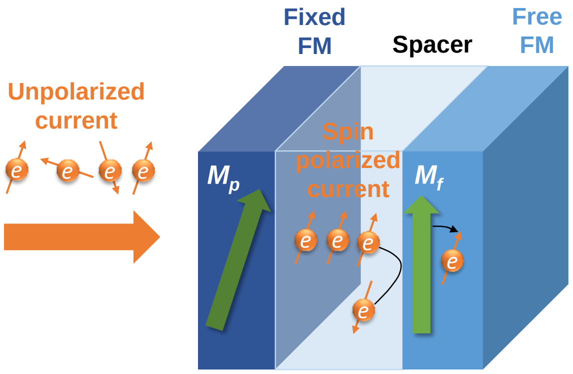

FIG. 1.2 Schematics of STT effect in non-collinear magnetic multilayers with a structure of FM/NM/FM. Figure adapted from Ref. [35].

After the observation of STT in various types of structures with in-plane magnetic anisotropy (IMA), particularly MTJ, it was soon realized that MTJ with perpendicular magnetic anisotropy (PMA) is the best candidate for STT-based devices due to its low switching current, reduced process variation, and excellent down scaling capability.[7,36] However, the demonstration of STT in PMA based MTJs was hindered by the lack of suitable material that can simultaneously give stable PMA, large TMR, and low switching current. Back then, the three main classes of PMA materials are $L1_0$-ordered (Co, Fe)–Pt alloys,[37] rare earth transition metal alloys[38] and Co/(Pt, Pd) multilayers.[39] The first class of materials has high switching current due to large damping constant;[35,40,41] the second group cannot withstand the high annealing temperature for MgO crystallization; and the last category suffers from small TMR ratio limited by the small spin polarization. Situation changed drastically in 2010 when two groups[41,42] demonstrated independently interfacial PMA between CoFeB and MgO, which fulfils all the three conditions in Ta/CoFeB/MgO based high performance MTJs. The CoFeB/MgO is expected to be the workhorse for STT-MRAM, which is on the verge of commercialization.

Despite the great potential of MgO-based PMA MTJs, the drawback of this type of two-terminal STT device is that it is difficult to optimize writing and reading process simultaneously in a same device.[43] This is because, on one hand, one needs a relatively thicker barrier to achieve larger readout signal, and on the other hand, a thick barrier demands a larger switching current, which causes stress to the MgO barrier and degrades the overall reliability of the device. One possible approach to mitigate the issue is to separate the writing and reading current path; this has led to the development of three terminal devices in which writing is based on spin-orbit torque (SOT) replacing STT.

The SOT arises from non-equilibrium spin density induced by either local or non-local spin-orbit interaction, or the so-called (ISGE).[44,45] The presence of ISGE requires an FM with either bulk or structure inversion asymmetry (SIA).[46-49] In these material structures, a charge current passing through an FM or an FM/heavy metal (HM) heterostructure generates a non-equilibrium spin density through the ISGE, which in turn exerts a torque on the local magnetization of the FM through either *s*-*d* (in the case of a transition metal) or *p*-*d* (in the case of dilute magnetic semiconductor) exchange coupling. As the ISGE is originated from spin-orbit coupling (SOC), the resultant torque is referred to as SOT. Unlike STT, which requires non-collinear magnetization configurations, the SOT can be realized in structures with a uniform magnetization; this greatly simplifies the structure and device design when investigating and exploiting the SOT effect for spintronic applications.

Although SOC induced spin polarization of electrons has been studied extensively in semiconductors,[50-52] the investigations of SOC induced non-equilibrium spin density in FMs and the resultant SOT on local magnetization have only been reported recently. Manchon and Zhang[46,53] predicted theoretically that, in the presence of a Rashba SOC, the SOT is able to switch the magnetization of magnetic two-dimensional electron gas at a current density of about $10^4 – 10^6$ A cm^{-2}, which is lower than or comparable to the critical current density of typical STT devices.[40] The first experimental observation of SOT was reported by Chernyshov *et al.* for $Ga_{0.94}Mn_{0.06}As$

dilute magnetic semiconductor (DMS) grown epitaxially on GaAs (001) substrate.[47] The compressive strain from lattice mismatch results in a Dresselhaus-type SOC that is linear in momentum. When a charge current passes through the DMS layer below its Curie temperature, the resultant SOT was able to switch the magnetization with the assistance of an external field and crystalline anisotropy. The lack of bulk inversion asymmetry (BIA) in transition metal FM has prompted researchers to explore the SOT effect in FM heterostructures with SIA. Miron *et al.* reported the first observation of a current-induced SOT in a thin Co layer sandwiched by a Pt and an AlO_x layer.[48] Due to the asymmetric interfaces with Pt and AlO_x, electrons in the Co layer experience a large Rashba effect, leading to sizable current-induced SOT. In addition to the Rashba SOT, spin current from the Pt layer due to spin Hall effect (SHE) also exerts a torque on the FM layer through transferring the spin angular momentum to the local magnetization. Although the exact mechanism still remains debatable, both types of torques are generally present in the FM/HM bilayers. The former is field-like, while the latter is of anti-damping nature similar to the STT. To date, the SOT effect has been reported in several FM/HM bilayers with different FMs such as CoFeB,[54-59] Co,[60-62] NiFe[63-65] and HMs such as Pt, Ta, and W. An average effective field strength of 4×10^{-6} Oe (A^{-1} cm^2) has been obtained, except for the $[Pd/Co]_n/Ta$ multilayer[66] which was reported to exhibit a very large effective field strength to current density ratio in the range of 10^{-5} Oe (A^{-1} cm^2). In the last case, the spin Hall current from Ta layer alone is unable to account for the large effective field, indicating possible contributions arising from the Pd/Co interfaces internally, though the exact mechanism is not clear. In the early works, an external field was needed to assist the magnetization switching of FM/HM bilayer with PMA, but recently several groups[67-71] have demonstrated completely field-free switching of magnetization in carefully designed structures, which paves the way for the adoption of SOT in real device applications.

Before ending this section, we would like to emphasize how spintronics can help the device technology. As the CMOS is scaled down, the computer operating power increases from both the increase in static leakage (standby) power and in device packing density. Fig. 1.3(a) presents the state-of-the-art computer memory hierarchy. The working memories such as SRAM cache and DRAM main memory are volatile. As is expected, the sub-threshold leakage increases exponentially upon the dimension of transistors consisting of the memories are scaled down, and thus causes a large increase in static current leakage.

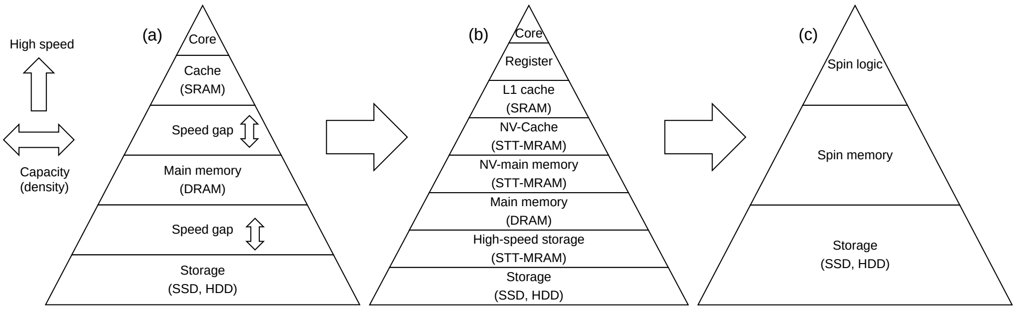

FIG. 1.3 (a) the conventional memory hierarchy; (b) non-volatile memory hierarchy of first generation using STT-MRAM; and (c) second generation in which logic is also made non-volatile using spintronics. Figure adapted from Ref. [72]

On the other hand, the integration of a fast, energy efficient non-volatile (NV) memory technology with CMOS can help alleviate this problem. Among the various technologies, spintronic devices are strong candidates for non-volatile memory due to the inherent hysteresis in ferromagnetic materials, and its compatibility with the standard CMOS process. Nowadays, the STT-

MRAM is right on the verge of commercialization. Fig. 1.3(b) proposes a possible new memory hierarchy in which the last level (LL) cache is constructed by non-volatile STT-MRAM. The structure can largely solve the power dissipation problem because of the elimination of the large static current by shutting down the power supply of the non-volatile cache memory at standby. Another bottleneck to notice is the speed gap between the SRAM cache and the DRAM main memory and that between the DRAM main memory and the storage (SSD, HDD) [see Fig. 1.3(a)]. In Fig. 1.3(b), the two speed gaps are filled with NV-main memory and high-speed storage to boost performance, both being based on STT-MRAM. The use of these STT-MRAM in NV-main memory as DRAM cache and in high-speed storage as storage cache can effectively solve the speed gap problem, and largely improve the computer performance. The table below gives a comparison on some technical specifications of existing non-spintronic and emerging spintronic memory technologies (STT-MRAM). Finally, Fig. 1.3(c) depicts the next step, an extreme non-volatile computer system. In this second generation system, logic is also made non-volatile by using spintronics.

TABLE 1.1 Comparison on some technical specifications of existing non-spintronic and emerging spintronic memory technologies (STT-MRAMs) [adapted from Ref. 73].

Technology	SRAM	DRAM	Flash (SSD)	STT-MRAM
Energy/bit (fJ)	100	1000	10^6	100
Write speed (ns)	1	20	1000	1 – 10
Read speed (ns)	1	30	10	1 – 10
Density (area in F2)	>30	6 – 10	4 – 8	10 – 30
Endurance (cycles)	Very high	Very high	Low	Very high
Non-volatile	No	No	Yes	Yes
Standby power	Leakage current	Refresh current	None	None

1.2 Antiferromagnet spintronics

For a very long time, other than being used as a pinning layer for FMs, AFs do not play an "active" role in spintronic devices due to their lack of net moment and almost zero response to weak external magnetic field. Due to its large magnetic anisotropy, the field required to change its spin configuration is several orders of magnitude larger than that of typical FMs. However, when looking from a different perspective, AF-based devices could offer several advantages as compared to their FM counterparts if they can be realized. First, the absence of stray field allows to pack the devices with a much higher density. Second, the insensitivity of AF to external field or thermal fluctuation promises the realization of more stable devices at a much smaller size. Third, the faster spin dynamics in AF can potentially lead to devices with much higher operation speed. If AF based devices is successfully realized, these promising properties of AF can further improve the devices in terms of density and speed. Therefore, it has stimulated studies[74-77] to re-examine the possibility of AF-based spintronics, in which the AFs will play more active roles, instead of just serving as a pining layer for FMs.

So far, the efforts have been made on both fronts, *i.e.*, how to write and read AF spin states. The most straightforward way to read the AF spin state is to use the AMR effect.[78] The AMR, commonly present in FM, is also observable in AFs,[79] because the AMR is a function of the microscopic magnetic moment vector, or in other words, it is the direction of the spin axis rather than the direction of the macroscopic magnetization that determines the magnitude of AMR. For FMs, the magnetization and spin axis are the same, whereas in AFs, although the macroscopic magnetization is zero, the spin axis can still be defined, and this ensures the existence of the AMR effect.[76] For example, an ohmic AMR ratio of 1% has been observed in epitaxial FeRh films for two distinct spin axis alignments at room temperature.[80] In another proof-of-concept experiment on IrMn/oxide/Pt tunnel junction, a tunnel AMR ratio of >100% has been observed at low temperature.[81] Several follow-up experiments have further demonstrated the feasibility of using AMR to detect the AF spin state.[82-85]

Compared to read operation, "writing" of AF poses more challenges. In the aforementioned case of FeRh, field-cooling from above T_N, in analogy to the heat-assisted technique in magnetic recording, is adopted to change the AF spin axis.[80,85] Alternatively, in the case of AF tunnel junctions, the AF spins are rotated indirectly via the exchange spring effect with FM by the external field.[81-84] The requirement of an additional magnetic field or heating process is apparently undesirable for practical applications. To circumvent this limitation, Nunez and MacDonald[86] proposed the first microscopic model, predicting that the transport current can also exert torque onto the sub-lattices of AFs, in analogy to STT in FMs. Although the AF sub-lattices are staggered, non-equilibrium spin densities can still be induced by a charge current in AF. The induced non-equilibrium spin density with polarization perpendicular to the local moment direction can produce an effective magnetic field and induces local moment precession. Subsequently, *ab-initio* method,[87,88] microscopic or macroscopic treatment based on staggered spin states or anti-parallel coupled spin sub-lattices,[89-95] unexclusively demonstrate the existence of STT in AF materials. Furthermore, it has been suggested that the non-zero

STT can cause reorientation of AF spin configuration,[92,95] domain wall motion,[90,91] and stable oscillation or precession of the Néel vector,[93,94] in analogy to those caused by STT in FM. The critical current density required for inducing these effects in AF is predicted to be on the order of 10^5 A cm^{-2},[86] smaller than that of the FM materials as mentioned above, because of the absence of shape anisotropy and the fact that STT can act through the entire volume of AF. Early experimental efforts on exploring STT in AFs have been focused mainly on exchange biased spin-valve, involving FM/NM/FM/AF heterostructures with either FeMn or IrMn as the AF element.[96-99] By applying DC current of different magnitude and direction, the exchange bias (H_{eb}) at the FM-AF interface can be altered, which suggests partial canting of the spin sub-lattices in AF layer, in qualitative agreement with the theoretical predictions. The Joule heating effect is excluded in these studies since the change of H_{eb} depends also on the current polarity, instead of only on the magnitude. Despite these observations, reports on direct experimental detection of STT effect in AF are elusive.

After the realization of the SOT-driven magnetization switching in FM based heterostructures, it was predicted that in AFs with broken bulk or structural inversion symmetry, the spin-axis can be reoriented by an electrical current induced non-equilibrium effective field, the so-called “Néel order spin orbit torque”.[100] This together with other theoretical proposals of AF-based pure spin current devices[101-104] have triggered extensive experimental examinations of AF in the past two years, particularly, on the following aspects: i) if AFs can transport spin current, ii) if AFs can generate spin current by themselves, and iii) how the AF magnetization will respond to the spin current generated either inside or outside the AF.

The first category of studies often involves AF oxides, such as NiO and CoO. It has been demonstrated in spin pumping experiments that, in FM/AF/HM heterostructures,[105-108] spin current can travel efficiently across AF in a relatively large length scale up to tens of nm without significant loss. Moreover, at temperatures near the Néel temperature (T_N) of AF, an enhancement of spin current across the AF layer was inferred from the inverse spin Hall effect signal from the HM,[109,110] which suggests the possibility of using AF as a spin current "booster". These observations were explained as being caused either by spin fluctuation[109-113] near critical temperature or spin current induced coherent Néel order dynamics[114] in the entire AF volume. Other mechanisms involving evanescent AF spin wave mode[115] or incoherent diffusive thermal AF magnons[116] as spin "carrier" were also proposed recently.

In the second category of investigations, relatively large spin Hall angle (comparable to that of Pt) was observed in metallic AFs such as IrMn, PdMn and PtMn,[117] which was attributed to either the large SOC of heavy metal element (Ir, Pd, Pt) or the non-collinear AF spin configuration.[118] The large SHE in AF makes it possible for AF to function as both a pining layer as in conventional exchange bias structures and the HM layer in SOT devices, as demonstrated recently by different groups in IrMn, PdMn, and PtMn based AF/FM bilayers.[119-123] More importantly, by replacing HM with AF, an in-plane exchange bias field (H_{eb}) can also be induced from post field annealing process. In this way, the symmetry of the magnetic energy landscape of PMA FM is broken, and thus leading to deterministic magnetization switching without an in-plane assist field. It is worth pointing out that it was only demonstrated this year that the FM magnetization can be switched deterministically by SHE in both PtMn[67] and IrMn[70] with carefully designed in-plane H_{eb}.

Compared to the first two categories, the experimental reports falling into the last category are quite limited. One approach to manipulate AF spins by spin current is to search for AF materials with intrinsic inversion asymmetry, in analogy to DMS for the FM case.[47] SOT-induced electrical switching of the spin-axis in CuMnAs epitaxial films with local inversion asymmetry from Mn pairs has been demonstrated recently.[124] By applying millisecond current pulses in a specific direction, the spin-axis can be reversibly rotated and the signal as probed by AMR can reach a level of 10%. However, deposition of such kind of unconventional material using molecular beam epitaxy is not straightforward; in addition, its non-compatibility with existing metal spintronics processes may pose problems towards device applications. An alternative approach is to adopt AF/HM heterostructures, in analogy to FM/HM heterostructures.[48] In this case, the spin current is generated from HM, and therefore it is not necessary to find AFs with inversion asymmetry. The choice of commonly used AFs will facilitate the device fabrication, and is thus more suitable for practical applications.

1.3 Motivation of this work

The beginning of this work coincides with the emerging interest in both SOT and AF spintronics. Therefore, the motivation here is quite straightforward, *i.e.*, to study how the spin current can interact with AF. In particular, it is interested to study if SOT effect is present in AF/HM heterostructures and, if it indeed exists, whether it can be used to manipulate the AF spin sub-lattices. To better understand the motivation of this work in the relatively brief history of AF spintronics, a summary of the major experimental progresses on this topic, as discussed above, is given in Fig. 1.4.

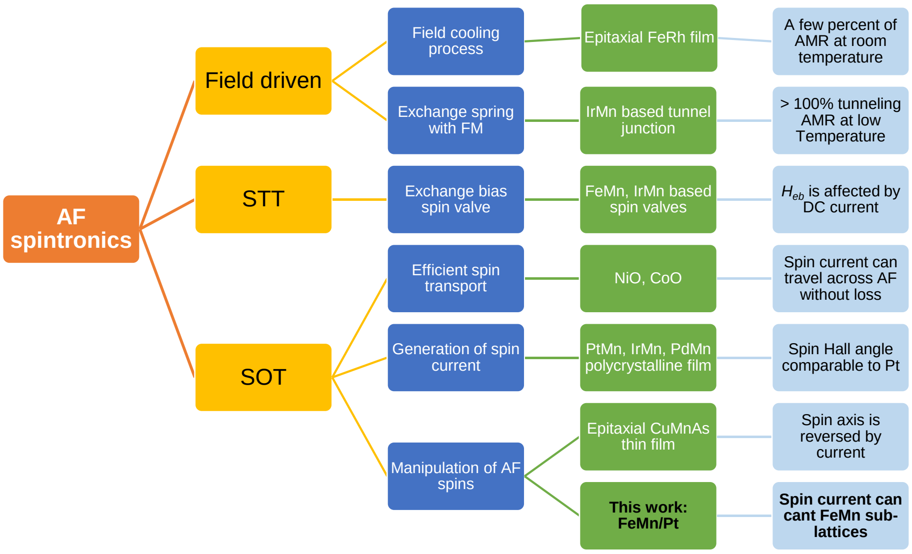

FIG. 1.4 Summary of the major experimental progresses in recent years on AF spintronics.

Among the various AF materials, FeMn was chosen based on the following three considerations. First, from the application point of view, it is more desirable to investigate AFs that have already been widely studied as pinning layers in metallic spintronic devices. FeMn is known to have a moderate pinning field with a relatively small critical thickness (~3 - 4 nm); the latter is important for studying SOT effect in AF/HM bilayers. Second, other than many other metallic AFs that have been reported to have a large SHE, the spin Hall angle of FeMn is negligible, at least two orders of magnitude smaller than those of common HMs.[117,125] This can facilitate the analysis of spin current transport in AF/HM heterostructures as one only needs to consider the spin current generated from the HM. Third, FeMn is also the “softest” among the Mn-based AF alloys. Therefore, it would be easier to detect it if there is any SOT effect. Similar to many reports on FM/HM bilayers, Pt, the most commonly used HM, was used as the SHE metal to generate spin current. This will make the data analysis more straightforward as the only difference here is the replacement of FM by an AF.

The work began with the examination of the SOT effect in FeMn/Pt bilayers. The emphasis was placed on whether SOT is present in the bilayer, and if so how to quantify it. SHE and macro-spin model are invoked to explain the experimental observations. In addition to FeMn/Pt bilayers, we have also investigated spin current transport in NiFe/FeMn/Pt trilayers.

The second part of the work is focused on the study of thickness dependence of spin Hall magnetoresistance (SMR) in FeMn/Pt bilayers. Both SMR and SOT are widely studied in FM/HM bilayers. And although the origin of SMR is still somewhat debatable, it is generally agreed that they are complementary phenomena with a common origin: both originate from the spin current generated in the HM layer, with the former related to spin current reflection and the latter related to transmission at FM/HM interfaces.[126,127] Therefore, the SMR, if any observed in the FeMn/Pt bilayers, would further confirm the existence of SOT in these bilayers as discussed in the first part of this thesis. To the best of our knowledge, SMR in metallic AF/HM heterostructures has yet to be reported.

In the last part, we extend the investigation to $[\mathrm{FeMn/Pt}]_n$ multilayers. We report the realization of a new type of ferromagnetic material – $[\mathrm{FeMn/Pt}]_n$ multilayers and further demonstrate that the magnetization of FeMn/Pt multilayer can be reversibly switched by SOT without any external field. This was stimulated by the observation of both SOT in FeMn/Pt and proximity effect at FeMn/Pt interfaces. The realization of SOT-driven switching in such kind of structure can largely facilitate device design since it does not have any constraint in the total FM thickness, which will certainly open new opportunities for SOT-based devices.

1.4 Thesis organization

In this chapter, a brief introduction was given to FM and AF spintronics, in particular the recently emerged SOT-driven magnetization switching and progresses in AF spintronics. In Chapter 2, some theoretical background will be provided on ferromagnetism and antiferromagnetism, magneto-transport phenomenon, spin current, SOC, SOT, SMR, micromagnetic simulation, macro-spin model, and drift-diffusion formalism, all of which are necessary for understanding spin and spin-dependent charge transport in FM/HM or AF/HM heterstructures.

Chapter 3 presents a detailed description of the sample fabrication and characterization techniques, including process flow of optical lithography, sputtering, structural and magnetic characterization, and magneto-transport measurement.

Chapter 4 presents the investigation of the SOT effect in FeMn/Pt bilayers. The field-like effective field is extracted from 2nd order planar Hall effect measurements. A large field-like effective field was found at small FeMn thickness, nearly two orders of magnitude larger than that of NiFe/Pt bilayers, which can be understood as originated from the reduced net moment in FeMn; the latter was confirmed by the magnetometry measurements. The experimental observations can be accounted for reasonably well by a macro-spin model in which thin FeMn layers are assumed to be consisting of two uncompensated sub-lattices with unequal magnetizations. In addition to bilayers, NiFe/FeMn/Pt trilayers were also investigated. By quantifying the effective field in NiFe from trilayers with different FeMn thicknesses, the spin diffusion length of FeMn can be estimated through the drift-diffusion formalism. The results confirmed that spin current is indeed absorbed by FeMn to induce the SOT.

Chapter 5 discusses the thickness dependence of SMR in FeMn/Pt to further confirm the existence of SOT in the bilayers. It starts with the presentation of the SMR results from samples with different Pt and FeMn thicknesses. The non-monotonic dependence of SMR on the thicknesses of both FeMn and Pt is analyzed following the spin Hall and drift-diffusion formalism. The difference between FeMn and NiFe thickness dependence is discussed in detail, which highlights the importance of thickness-dependent magnetic properties of ultrathin AF films. Finally, the correlation of SMR ratio with SOT effective field is discussed and used to affirm the conclusions drawn in Chapter 4.

Chapter 6 presents the study of magnetic properties and SOT effect in ultra-thin $[\text{FeMn/Pt}]_n$ multilayers. First, the magnetic properties of the multilayers obtained from magnetometry measurements are presented and its origin is discussed from fitting of the *M*-*T* curves. Next, the field-like SOT effective field is extracted from 2nd order PHE measurements. The observed SOT effective field is around 4 times larger than that of NiFe with a same equivalent thickness, which is attributed to the asymmetry between top and bottom FeMn/Pt interfaces, and the local generation of spin current in the Pt layers and absorption by the neighboring FeMn layers. Finally, the current induced magnetization switching results are presented and discussed in detail.

Chapter 7 concludes this thesis and gives some suggestions for future work based on the findings obtained in this work.

References

[1] W. Arden, M. Brillouët, P. Cogez, M. Graef, B. Huizing, and R. Mahnkopf, International Technical Roadmap for Semiconductors (2010).

[2] I. Žutić, J. Fabian, and S. D. Sarma, Rev. Mod. Phys. **76**, 323 (2004).

[3] M. N. Baibich, J. M. Broto, A. Fert, F. Nguyen Van Dau, F. Petroff, P. Etienne, G. Creuzet, A. Friederich, and J. Chazelas, Phys. Rev. Lett. **61**, 2472 (1988).

[4] G. Binasch, P. Grünberg, F. Saurenbach, and W. Zinn, Phys. Rev. B **39**, 4828 (1989).

[5] B. Dieny, V. S. Speriosu, S. S. P. Parkin, B. A. Gurney, D. R. Wilhoit, and D. Mauri, Phys. Rev. B **43**, 1297 (1991).

[6] A. Fert, Rev. Mod. Phys. **80**, 1517 (2008).

[7] J.-G. Zhu and C. Park, Materials Today **9**, 36 (2006).

[8] C. Chappert, A. Fert, and F. N. V. Dau, Nat. Mater. **6**, 813 (2007).

[9] J. M. Daughton, J. Appl. Phys. **81**, 3758 (1997).

[10] M. Jullière, Phys. Lett. **54A**, 225 (1975).

[11] T. Miyazaki and N. Tezuka, J. Magn. Magn. Mater. **139**, 231 (1995).

[12] J. S. Moodera, L. R. Kinder, T. M. Wong, and R. Meservey, Phys. Rev. Lett. **74**, 3273 (1995).

[13] D. Wang, C. Nordman, J. M. Daughton, Z. Qian, and J. Fink, IEEE Trans. Magn. **40**, 2269 (2004).

[14] W. H. Butler, X. G. Zhang, T. C. Schulthess, and J. M. MacLaren, Phys. Rev. B **63**, 054416 (2001).

[15] J. Mathon and A. Umerski, Phys. Rev. B **63**, 220403(R) (2001).

[16] S. S. Parkin, C. Kaiser, A. Panchula, P. M. Rice, B. Hughes, M. Samant, and S. H. Yang, Nat. Mater. **3**, 862 (2004).

[17] S. Yuasa, T. Nagahama, A. Fukushima, Y. Suzuki, and K. Ando, Nat. Mater. **3**, 868 (2004).

[18] S. Ikeda, J. Hayakawa, Y. M. Lee, R. Sasaki, T. Meguro, F. Matsukura, and H. Ohno, Jpn. J. Appl. Phys. **44**, L1442 (2005).

[19] D. D. Djayaprawira, K. Tsunekawa, M. Nagai, H. Maehara, S. Yamagata, N. Watanabe, S. Yuasa, Y. Suzuki, and K. Ando, Appl. Phys. Lett. **86**, 092502 (2005).

[20] S. Yuasa, A. Fukushima, H. Kubota, Y. Suzuki, and K. Ando, Appl. Phys. Lett. **89**, 042505 (2006).

[21] K. Tsunekawa, D. D. Djayaprawira, S. Yuasa, M. Nagai, H. Maehara, S. Yamagata, E. Okada, NaokiWatanabe, Y. Suzuki, and K. Ando, IEEE Trans. Magn. **42**, 103 (2006).

[22] S. Ikeda, J. Hayakawa, Y. Ashizawa, Y. M. Lee, K. Miura, H. Hasegawa, M. Tsunoda, F. Matsukura, and H. Ohno, Appl. Phys. Lett. **93**, 082508 (2008).

[23] J. C. Slonczewski, J. Magn. Magn. Mater. **159**, L1 (1996).

[24] L. Berger, Phys. Rev. B **54** (1996).

[25] M. Tsoi, A.G.M. Jansen, J. Bass, W.C. Chiang, M. Seck, V. Tsoi, and P. Wyder, Phys. Rev. Lett. **80**, 4281 (1998).

[26] J. Z. Sun, J. Magn. Magn. Mater. **202**, 157 (1999).

[27] E. B. Myers, D. C. Ralph, J. A. Katine, R. N. Louie, and R. A.

Buhrman, Science **285**, 867 (1999).

28 B. Ozyilmaz, A. D. Kent, D. Monsma, J. Z. Sun, M. J. Rooks, and R. H. Koch, Phys. Rev. Lett. **91**, 067203 (2003).

29 B. Ozyilmaz, A. D. Kent, J. Z. Sun, M. J. Rooks, and R. H. Koch, Phys. Rev. Lett. **93**, 176604 (2004).

30 N. Vernier, D. A. Allwood, D. Atkinson, M. D. Cooke, and R. P. Cowburn, Europhysics Letters (EPL) **65**, 526 (2004).

31 F. J. Albert, J. A. Katine, and R. A. Buhrman, Appl. Phys. Lett. **77**, 3809 (2000).

32 J. A. Katine, F. J. Albert, and R. A. Buhrman, Phys. Rev. Lett. **84**, 3149 (2000).

33 G. D. Fuchs, N. C. Emley, I. N. Krivorotov, P. M. Braganca, E. M. Ryan, S. I. Kiselev, J. C. Sankey, D. C. Ralph, R. A. Buhrman, and J. A. Katine, Appl. Phys. Lett. **85**, 1205 (2004).

34 Y. Huai, F. Albert, P. Nguyen, M. Pakala, and T. Valet, Appl. Phys. Lett. **84**, 3118 (2004).

35 A. Brataas, A. D. Kent, and H. Ohno, Nat. Mater. **11**, 372 (2012).

36 J. Z. Sun, Phys. Rev. B **62**, 570 (2000).

37 H. Yoda, T. Kishi, T. Nagase, M. Yoshikawa, K. Nishiyama, E. Kitagawa, T. Daibou, M. Amano, N. Shimomura, S. Takahashi, T. Kai, M. Nakayama, H. Aikawa, S. Ikegawa, M. Nagamine, J. Ozeki, S. Mizukami, M. Oogane, Y. Ando, S. Yuasa, K. Yakushiji, H. Kubota, Y. Suzuki, Y. Nakatani, T. Miyazaki, and K. Ando, Current Applied Physics **10**, e87 (2010).

38 M. Nakayama, T. Kai, N. Shimomura, M. Amano, E. Kitagawa, T. Nagase, M. Yoshikawa, T. Kishi, S. Ikegawa, and H. Yoda, J. Appl. Phys. **103**, 07A710 (2008).

39 B. Carvello, C. Ducruet, B. Rodmacq, S. p. Auffret, E. Gautier, G. Gaudin, and B. Dieny, Appl. Phys. Lett. **92**, 102508 (2008).

40 D. C. Ralph and M. D. Stiles, J. Magn. Magn. Mater. **320**, 1190 (2008).

41 S. Ikeda, K. Miura, H. Yamamoto, K. Mizunuma, H. D. Gan, M. Endo, S. Kanai, J. Hayakawa, F. Matsukura, and H. Ohno, Nat. Mater. **9**, 721 (2010).

42 D. C. Worledge, G. Hu, D. W. Abraham, J. Z. Sun, P. L. Trouilloud, J. Nowak, S. Brown, M. C. Gaidis, E. J. O'Sullivan, and R. P. Robertazzi, Appl. Phys. Lett. **98**, 022501 (2011).

43 P. Gambardella and I. M. Miron, Phil. Trans. R. Soc. A **369**, 3175 (2011).

44 S. D. Ganichev, E. L. Ivchenko, V. V. Bel'kov, S. A. Tarasenko, M. Sollinger, D. Weiss, W. Wegscheider, and W. Prett, Nature **417**, 156 (2002).

45 E. L. Ivchenko and S. Ganichev, *Spin Physics in Semiconductors*. (Springer, New York, 2008), p.245.

46 A. Manchon and S. Zhang, Phys. Rev. B **78**, 212405 (2008).

47 A. Chernyshov, M. Overby, X. Liu, J. K. Furdyna, Y. Lyanda-Geller, and L. P. Rokhinson, Nat. Phys. **5**, 656 (2009).

48 I. M. Miron, G. Gaudin, S. Auffret, B. Rodmacq, A. Schuhl, S. Pizzini, J. Vogel, and P. Gambardella, Nat. Mater. **9**, 230 (2010).

49 A. Manchon, H. C. Koo, J. Nitta, S. M. Frolov, and R. A. Duine, Nat.

Mater. **14**, 871 (2015).

[50] S. O. Valenzuela and M. Tinkham, Nature **442**, 176 (2006).

[51] J. Wunderlich, B. Kaestner, J. Sinova, and T. Jungwirth, Phys. Rev. Lett. **94**, 047204 (2005).

[52] V. Sih, R. C. Myers, Y. K. Kato, W. H. Lau, A. C. Gossard, and D. D. Awschalom, Nat. Phys. **1**, 31 (2005).

[53] A. Manchon and S. Zhang, Phys. Rev. B **79**, 094422 (2009).

[54] L. Liu, C. F. Pai, Y. Li, H. W. Tseng, D. C. Ralph, and R. A. Buhrman, Science **336**, 555 (2012).

[55] K. Garello, I. M. Miron, C. O. Avci, F. Freimuth, Y. Mokrousov, S. Blugel, S. Auffret, O. Boulle, G. Gaudin, and P. Gambardella, Nat. Nanotechnol. **8**, 587 (2013).

[56] J. Kim, J. Sinha, M. Hayashi, M. Yamanouchi, S. Fukami, T. Suzuki, S. Mitani, and H. Ohno, Nat. Mater. **12**, 240 (2013).

[57] G. Yu, P. Upadhyaya, Y. Fan, J. G. Alzate, W. Jiang, K. L. Wong, S. Takei, S. A. Bender, L.-T. Chang, Y. Jiang, M. Lang, J. Tang, Y. Wang, Y. Tserkovnyak, P. K. Amiri, and K. L. Wang, Nat Nano **9**, 548 (2014).

[58] X. Qiu, K. Narayanapillai, Y. Wu, P. Deorani, D. H. Yang, W. S. Noh, J. H. Park, K. J. Lee, H. W. Lee, and H. Yang, Nat. Nanotechnol. **10**, 333 (2015).

[59] C.-F. Pai, L. Liu, Y. Li, H. W. Tseng, D. C. Ralph, and R. A. Buhrman, Appl. Phys. Lett. **101**, 122404 (2012).

[60] L. Liu, O. J. Lee, T. J. Gudmundsen, D. C. Ralph, and R. A. Buhrman, Phys. Rev. Lett. **109**, 096602 (2012).

[61] I. M. Miron, K. Garello, G. Gaudin, P. J. Zermatten, M. V. Costache, S. Auffret, S. Bandiera, B. Rodmacq, A. Schuhl, and P. Gambardella, Nature **476**, 189 (2011).

[62] U. H. Pi, K. Won Kim, J. Y. Bae, S. C. Lee, Y. J. Cho, K. S. Kim, and S. Seo, Appl. Phys. Lett. **97**, 162507 (2010).

[63] X. Fan, J. Wu, Y. Chen, M. J. Jerry, H. Zhang, and J. Q. Xiao, Nat. Commun. **4**, 1799 (2013).

[64] T. Nan, S. Emori, C. T. Boone, X. Wang, T. M. Oxholm, J. G. Jones, B. M. Howe, G. J. Brown, and N. X. Sun, Phys. Rev. B **91**, 214416 (2015).

[65] L. Liu, T. Moriyama, D. C. Ralph, and R. A. Buhrman, Phys. Rev. Lett. **106**, 036601 (2011).

[66] M. Jamali, K. Narayanapillai, X. Qiu, L. Loong, A. Manchon, and H. Yang, Phys. Rev. Lett. **111**, 246602 (2013).

[67] S. Fukami, C. Zhang, S. DuttaGupta, A. Kurenkov, and H. Ohno, Nat. Mater. **15**, 535 (2016).

[68] A. van den Brink, G. Vermijs, A. Solignac, J. Koo, J. T. Kohlhepp, H. J. Swagten, and B. Koopmans, Nat. Commun. **7**, 10854 (2016).

[69] L. You, O. Lee, D. Bhowmik, D. Labanowski, J. Hong, J. Bokor, and S. Salahuddin, Proc. Natl. Acad. Sci. USA **112**, 10310 (2015).

[70] Y. W. Oh, S. H. Chris Baek, Y. M. Kim, H. Y. Lee, K. D. Lee, C. G. Yang, E. S. Park, K. S. Lee, K. W. Kim, G. Go, J. R. Jeong, B. C. Min, H. W. Lee, K. J. Lee, and B. G. Park, Nat. Nanotechnol. **advance online publication** (2016).

[71] Y.-C. Lau, D. Betto, K. Rode, J. M. D. Coey, and P. Stamenov, Nat. Nanotechnol. **11**, 756 (2016).

[72] Y. Nishi, *Advances in Non-volatile Memory and Storage Technology*. (Woodhead Publishing, UK, 2014), p.464.

[73] K. L. Wang, J. G. Alzate, and P. Khalili Amiri, J. Phys. D: Appl. Phys. **46**, 074003 (2013).

[74] A. H. MacDonald and M. Tsoi, Phil. Trans. R. Soc. **369**, 3098 (2011).

[75] E. V. Gomonay and V. M. Loktev, Low Temp. Phys. **40**, 17 (2014).

[76] T. Jungwirth, X. Marti, P. Wadley, and J. Wunderlich, Nat. Nanotechnol. **11**, 231 (2016).

[77] V. Baltz, A. Manchon, M. Tsoi, T. Moriyama, T. Ono, and Y. Tserkovnyak, arXiv:1606.04284 (2016).

[78] T. R. McGuire and R. I. Potter, IEEE Trans. Magn. **11**, 1018 (1975).

[79] A. B. Shick, S. Khmelevskyi, O. N. Mryasov, J. Wunderlich, and T. Jungwirth, Phys. Rev. B **81**, 212409 (2010).

[80] X. Marti, I. Fina, C. Frontera, J. Liu, P. Wadley, Q. He, R. J. Paull, J. D. Clarkson, J. Kudrnovsky, I. Turek, J. Kunes, D. Yi, J. H. Chu, C. T. Nelson, L. You, E. Arenholz, S. Salahuddin, J. Fontcuberta, T. Jungwirth, and R. Ramesh, Nat. Mater. **13**, 367 (2014).

[81] B. G. Park, J. Wunderlich, X. Marti, V. Holy, Y. Kurosaki, M. Yamada, H. Yamamoto, A. Nishide, J. Hayakawa, H. Takahashi, A. B. Shick, and T. Jungwirth, Nat. Mater. **10**, 347 (2011).

[82] D. Petti, E. Albisetti, H. Reichlová, J. Gazquez, M. Varela, M. Molina-Ruiz, A. F. Lopeandía, K. Olejník, V. Novák, I. Fina, B. Dkhil, J. Hayakawa, X. Marti, J. Wunderlich, T. Jungwirth, and R. Bertacco, Appl. Phys. Lett. **102**, 192404 (2013).

[83] Y. Y. Wang, C. Song, B. Cui, G. Y. Wang, F. Zeng, and F. Pan, Phys. Rev. Lett. **109**, 137201 (2012).

[84] X. Martí, B. G. Park, J. Wunderlich, H. Reichlová, Y. Kurosaki, M. Yamada, H. Yamamoto, A. Nishide, J. Hayakawa, H. Takahashi, and T. Jungwirth, Phys. Rev. Lett. **108**, 017201 (2012).

[85] T. Moriyama, N. Matsuzaki, K.-J. Kim, I. Suzuki, T. Taniyama, and T. Ono, Appl. Phys. Lett. **107**, 122403 (2015).

[86] A. Núñez, R. Duine, P. Haney, and A. MacDonald, Phys. Rev. B **73**, 214426 (2006).

[87] P. Haney, D. Waldron, R. Duine, A. Núñez, H. Guo, and A. MacDonald, Phys. Rev. B **75**, 174428 (2007).

[88] Y. Xu, S. Wang, and K. Xia, Phys. Rev. Lett. **100**, 226602 (2008).

[89] R. Duine, P. Haney, A. Núñez, and A. MacDonald, Phys. Rev. B **75**, 014433 (2007).

[90] K. M. D. Hals, Y. Tserkovnyak, and A. Brataas, Phys. Rev. Lett. **106**, 107206 (2011).

[91] E. Tveten, A. Qaiumzadeh, O. Tretiakov, and A. Brataas, Phys. Rev. Lett. **110**, 127208 (2013).

[92] H. V. Gomonay and V. M. Loktev, Phys. Rev. B **81**, 144427 (2010).

[93] H. V. Gomonay, R. V. Kunitsyn, and V. M. Loktev, Phys. Rev. B **85**, 134446 (2012).

[94] Y. V. Gulyaev, P. E. Zilberman, and E. M. Epshtein, J. Exp. Theor. Phys. **114**, 296 (2012).

[95] J. Linder, Phys. Rev. B **84**, 094404 (2011).

[96] S. Urazhdin and N. Anthony, Phys. Rev. Lett. **99**, 046602 (2007).

[97] Z. Wei, A. Sharma, A. Nunez, P. Haney, R. Duine, J. Bass, A.

MacDonald, and M. Tsoi, Phys. Rev. Lett. **98**, 116603 (2007).

98 X.-L. Tang, H.-W. Zhang, H. Su, Z.-Y. Zhong, and Y.-L. Jing, Appl. Phys. Lett. **91**, 122504 (2007).

99 N. Dai, N. Thuan, L. Hong, N. Phuc, Y. Lee, S. Wolf, and D. Nam, Phys. Rev. B **77**, 132406 (2008).

100 J. Železný, H. Gao, K. Výborný, J. Zemen, J. Mašek, A. Manchon, J. Wunderlich, J. Sinova, and T. Jungwirth, Phys. Rev. Lett. **113**, 157201 (2014).

101 H. B. M. Saidaoui, A. Manchon, and X. Waintal, Phys. Rev. B **89**, 174430 (2014).

102 R. Cheng, J. Xiao, Q. Niu, and A. Brataas, Phys. Rev. Lett. **113**, 057601 (2014).

103 R. Cheng, M. W. Daniels, J.-G. Zhu, and D. Xiao, Phys. Rev. B **91**, 064423 (2015).

104 R. Cheng, D. Xiao, and A. Brataas, Phys. Rev. Lett. **116**, 207603 (2016).

105 C. Hahn, G. de Loubens, V. V. Naletov, J. Ben Youssef, O. Klein, and M. Viret, EPL (Europhysics Letters) **108**, 57005 (2014).

106 T. Moriyama, S. Takei, M. Nagata, Y. Yoshimura, N. Matsuzaki, T. Terashima, Y. Tserkovnyak, and T. Ono, Appl. Phys. Lett. **106**, 162406 (2015).

107 H. Wang, C. Du, P. C. Hammel, and F. Yang, Phys. Rev. Lett. **113**, 097202 (2014).

108 H. Wang, C. Du, P. C. Hammel, and F. Yang, Phys. Rev. B **91**, 220410(R) (2015).

109 W. Lin, K. Chen, S. Zhang, and C. L. Chien, Phys. Rev. Lett. **116**, 186601 (2016).

110 Z. Qiu, J. Li, D. Hou, E. Arenholz, A. T. N'Diaye, A. Tan, K. Uchida, K. Sato, S. Okamoto, Y. Tserkovnyak, Z. Q. Qiu, and E. Saitoh, Nat. Commun. **7**, 12670 (2016).

111 Y. Ohnuma, H. Adachi, E. Saitoh, and S. Maekawa, Phys. Rev. B **89**, 174417 (2014).

112 T. Moriyama, M. Nagata, K. Tanaka, K.-J. Kim, H. Almasi, W. G. Wang, and T. Ono, arXiv:1411.4100 (2014).

113 L. Frangou, S. Oyarzun, S. Auffret, L. Vila, S. Gambarelli, and V. Baltz, Phys. Rev. Lett. **116**, 077203 (2016).

114 S. Takei, T. Moriyama, T. Ono, and Y. Tserkovnyak, Phys. Rev. B **92**, 020409(R) (2015).

115 R. Khymyn, I. Lisenkov, V. S. Tiberkevich, A. N. Slavin, and B. A. Ivanov, Phys. Rev. B **93**, 224421 (2016).

116 S. M. Rezende, R. L. Rodríguez-Suárez, and A. Azevedo, Phys. Rev. B **93**, 054412 (2016).

117 W. Zhang, M. B. Jungfleisch, W. Jiang, J. E. Pearson, A. Hoffmann, F. Freimuth, and Y. Mokrousov, Phys. Rev. Lett. **113**, 196602 (2014).

118 H. Chen, Q. Niu, and A. H. MacDonald, Phys. Rev. Lett. **112**, 017205 (2014).

119 V. Tshitoyan, C. Ciccarelli, A. P. Mihai, M. Ali, A. C. Irvine, T. A. Moore, T. Jungwirth, and A. J. Ferguson, Phys. Rev. B **92**, 214406 (2015).

120 H. Reichlová, D. Kriegner, V. Holý, K. Olejník, V. Novák, M. Yamada,

K. Miura, S. Ogawa, H. Takahashi, T. Jungwirth, and J. Wunderlich, Phys. Rev. B **92**, 165424 (2015).

[121] Y. Ou, S. Shi, D. C. Ralph, and R. A. Buhrman, Phys. Rev. B **93**, 220405(R) (2016).

[122] W. Zhang, W. Han, S.-h. Yang, Y. Sun, Y. Zhang, B. Yan, and S. S. P. Parkin, arXiv:1602.00670v1 (2015).

[123] W. Zhang, M. B. Jungfleisch, F. Freimuth, W. Jiang, J. Sklenar, J. E. Pearson, J. B. Ketterson, Y. Mokrousov, and A. Hoffmann, Phys. Rev. B **92**, 144405 (2015).

[124] P. Wadley, B. Howells, J. Železný, C. Andrews, V. Hills, R. P. Campion, V. Novák, K. Olejník, F. Maccherozzi, S. S. Dhesi, S. Y. Martin, T. Wagner, J. Wunderlich, F. Freimuth, Y. Mokrousov, J. Kuneš, J. S. Chauhan, M. J. Grzybowski, A. W. Rushforth, K. W. Edmonds, B. L. Gallagher, and T. Jungwirth, Science **351**, 587 (2016).

[125] C. Du, H. Wang, F. Yang, and P. C. Hammel, Phys. Rev. B **90**, 140407(R) (2014).

[126] J. Liu, T. Ohkubo, S. Mitani, K. Hono, and M. Hayashi, Appl. Phys. Lett. **107**, 232408 (2015).

[127] C. O. Avci, K. Garello, J. Mendil, A. Ghosh, N. Blasakis, M. Gabureac, M. Trassin, M. Fiebig, and P. Gambardella, Appl. Phys. Lett. **107**, 192405 (2015).

Chapter 2 Theoretical Background

In Chapter 1, a brief introduction is given to FM and AF spintronics. In this chapter, some theoretical backgrounds are provided on the topics that are relevant to this work.

2.1 Magnetism moment

Magnetic moment is fundamental to magnetism, which is closely related to the angular momentum of elementary particles. There are two distinct sources of the electron angular momentum: 1) orbital motion of electrons around the nucleus and 2) intrinsic spin angular momentum of electrons. The orbital moment arises from the electron circulating in its orbit, which can be equivalently regarded as a current loop where the current direction is opposite to the sense of circulation due to the negative electron charge. The proportional coefficient between the magnetic moment and the orbital angular momentum is known as the gyromagnetic ratio: $\gamma = e/(2m_e) \approx 0.88\times10^{11}\,\mathrm{C/kg}$, where e is the charge of a proton, m_e is the electron rest mass. The second source is the intrinsic electron spin angular momentum, which is equal to $\hbar/2$ according to the Dirac equation, where $\hbar$ is the Planck constant. This brings every electron an intrinsic magnetic moment of $e\hbar/2m_e$, which can only take one of two distinct orientations relative to a magnetic field. As a consequence, the gyromagnetic ratio of the electron's spin angular momentum is twice of that of orbital angular momentum.

2.2 Magnetic response of a material

Depending on how a material responds to an external magnetic field, it can be categorized as diamagnetic, paramagnetic, ferromagnetic, and antiferromagnetic, and

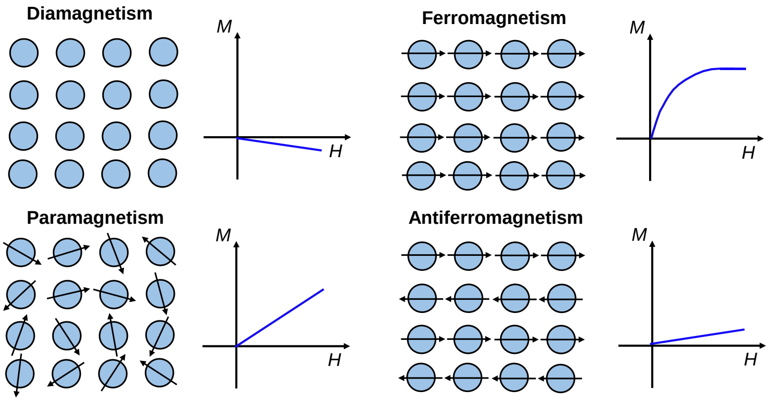

FIG. 2.1 Schematics of the spin configuration at zero field of diamagnetism, paramagnetism, ferromagnetism and antiferromagnetism, and their typical magnetic responses (*M*-*H* loops). Figure adapted from Ref. [1].

more quantitatively, it is characterized by the sign and magnitude of the susceptibility (χ). All materials show some degree of diamagnetism, which arises from a weak induced magnetic moment in the direction opposite to the externally applied magnetic field. As can be seen from Fig. 2.1, its magnetic susceptibility is small and negative (-10^{-5} – -10^{-6}), and typical examples of diamagnetic materials are water, silica and superconductors. On the contrary, paramagnetism refers to substance that can produce magnetic moment (stronger than diamagnetism) in the direction of the external field. It has a moderate susceptibility of 10^{-5} – 10^{-3}, and aluminum, magnesium and sodium are the typical examples of paramagnetic materials. Both diamagnetism and paramagnetism do not retain the magnetic properties once the external field is removed. As far as spintronic applications are concerned, the two most important types of materials are ferromagnet and antiferromagnet which are discussed below.

2.2.1 Ferromagnetism (FM) and antiferromagnetism (AF)

Ferromagnetism has its origin in quantum mechanical exchange interaction, which results in long range ordering of electron spins. The exchange interaction can be described phenomenologically by the Heisenberg model. According to this model, the exchange interaction between two spins is described by the Hamiltonian: $H = -2J\vec{S}_1 \cdot \vec{S}_2$,[2] where $\vec{S}_1$ and $\vec{S}_2$ are operators of two adjacent spins, and J is the exchange coupling constant. Based on energy minimization consideration, a positive J value prefers parallel alignment of the spins and thus leads to an FM order. A ferromagnet exhibits spontaneous magnetization, which is divided into small domains and within each domain, all the magnetic moments are aligned in the same direction. Magnetizations of different domains can be aligned by an external field, and the resultant magnetization is called saturation magnetization (M_s). After the field is removed, majority of the magnetic moments would stay fixed (remanent magnetization M_r), while a small portion will relax to random directions. If the field is further increased in the opposite direction, the FM will become demagnetized at a field called coercive field (H_c). The FM experiences a transition to paramagnetic phase above a certain temperature called "Curie temperature" (T_C). The magnetic susceptibility of FMs below T_C are high ($> 10^{-3}$), and the typical FMs are Fe, Ni, Co and their alloys.

On the other hand, an AF order is formed when J is negative, which favors an anti-parallel alignment of the adjacent spins based on the Heisenberg

Hamiltonian. In practical materials, an AF can consist of more than two sub-lattices, resulting in triangular, spiral, or canted spin alignment. The number of sub-lattices is determined by the number of magnetic ions in the primitive cell.[3] For example, $N = 2$ for MnF_2 and NiF_2, $N = 3$ for PtMn, IrMn, PdMn, and $N = 4$ for FeMn. A phenomenological treatment of AF based on the two sub-lattice model is proposed by L. Néel.[4] According to this model, AF can be considered as consisted of sub-lattices with spins situated on identical lattice sites and are antiparallel to each other. Table 2.1 summarizes some common AF materials. Similar to the FM, AF order also disappears above a critical temperature named as Néel temperature (T_N), transiting to a paramagnetic state. The transition is accompanied by a small peak in the magnetic susceptibility.

TABLE 2.1 Summary of the properties of some common AFs [adapted from Ref. 5].

Name	Structure	Néel temperature T_N (K)	Sub-lattice magnetization $\mu_0 M$ (T)
Cr	Spin density wave	311	0.20
Mn	Complex	96	0.20
NiO	Néel	524	0.54
αFe_2O_3	Canted	958	0.92
MnF_2	Néel	67	0.78
FeMn	Néel	510	0.53
$IrMn_3$	Néel	690	0.50

2.2.2 Exchange bias in FM/AF bilayers

When an FM is in contact with an AF, an exchange bias would appear at the interface, a phenomenon that was discovered more than 5 decades ago.[6] The exchange bias at the FM/AF interface is usually established through a magnetic annealing and cooling process, in which the sample is first heated up to above the Néel temperature of the AF, and then cooled to room temperature in the presence of a magnetic field with a strength of one to a few Tesla. As a consequence, the FM hysteresis loop is shifted in the field axis by an amount called exchange bias field (H_{eb}). When the AF's anisotropy is small, the AF spins will be rotated together with the FM spin, resulted in an increase in the FM's coercivity (H_c). The exchange bias in FM/AF bilayers is a very complex issue. Despite intensive studies, the phenomenon itself is still not well understood.[7] A simple picture based on fully compensated interface is illustrated in Fig. 2.2.

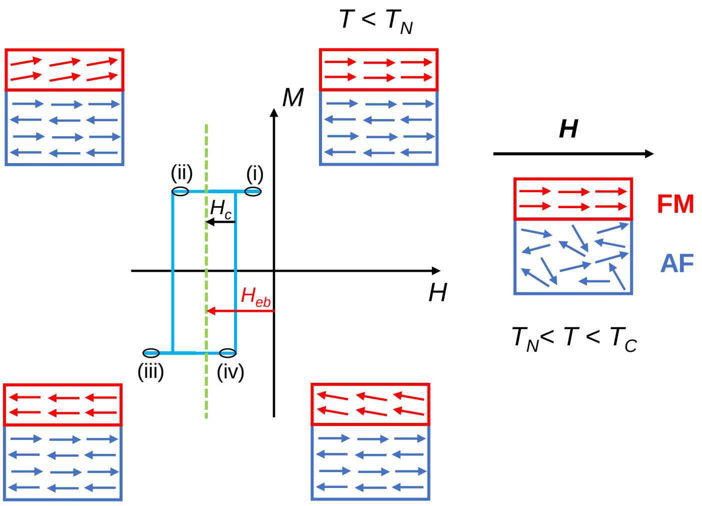

FIG. 2.2 Schematic diagram of the spin configuration of FM-AF bilayer at different stages (i) - (v) of exchange biased hysteresis loop. Figure adapted from Ref. [7].

Similar to other magnetic related phenomenon, the exchange bias effect is also dependent on the temperature, *i.e.*, it vanishes above a critical temperature called blocking temperature (T_B). In contrast to T_N which is the critical temperature of losing short range exchange coupling (H_{ex}) within the sub-lattice, T_B is the temperature at which the AF lost its long range AF anisotropy (H_A). Since H_{ex} is often orders of magnitude larger than H_A, T_B is lower than T_N in most cases. In this sense, the magnetic state between T_B and T_N can be considered as a superpara-antiferromagnetic state, in analogy to the superparamagnetic state in FM. The exchange bias effect originated from AF is widely used in modern spintronic devices to pin the magnetization of the adjacent FM layer.

2.2.3 Magnetic domains

Ferromagnetic materials consist of small magnetic domains. The domain structure at equilibrium state can be simulated by minimizing the total energy associated with different types of interactions. For a standalone ferromagnet, the typical energy terms include exchange energy (E_{ex}), anisotropy energy (E_{an}), Zeeman energy (E_{zeeman}) and magnetostatic energy (E_{demag}), *i.e.*,

$$E_{total} = E_{ex} + E_{an} + E_{zeeman} + E_{demag} \tag{2.1}$$

The exchange energy arises from the exchange coupling interaction of the neighboring spins (see the Heisenberg Hamiltonian in Section 2.2.1). In the case of FM, it induces parallel alignment of neighboring spins. In a continuous medium approximation, the exchange energy can be approximated by:

$$E_{ex} = \int_V \frac{J}{{M_s}^2} (|\nabla M_x|^2 + |\nabla M_y|^2 + |\nabla M_z|^2) dV \tag{2.2}$$

where dV is the volume element, M_x, M_y, M_z are the x, y, z components of $\vec{M}(\vec{r})$.

The anisotropy energy itself can have difference sources. The most fundamental type is the crystalline anisotropy which is caused by the interaction between crystal field and electron spin. In other words, the interaction of the spins with the crystal field favors some preferential directions (“easy axis”) over the others (“hard axis”) for the magnetization to be aligned. In most practical cases dealing with polycrystalline materials, the anisotropy is induced by an applied field during thin film deposition; therefore, it is sufficient to consider a uniaxial anisotropy, which is described by the following energy term:

$$E_{an} = \int_V K_u [1 - (\frac{M_x}{M_s})^2] dV \tag{2.3}$$

where K_u is the anisotropy constant. Note that in this expression, the easy axis is assumed to be in x-axis, and higher order terms are neglected.

In the presence of an external magnetic field $\vec{H}$, Zeeman energy is induced and is given by:

$$E_{zeeman} = -\int_V \vec{M}(\vec{r}) \cdot \vec{H} dV \tag{2.4}$$

As can be seen, Zeeman energy favors the magnetization to be aligned with the magnetic field.

Lastly, the magnetostatic energy originates from the long range dipole interaction inside the FM. This energy term favors magnetic flux closure and therefore competes directly with the exchange energy term. The magnetostatic energy term can be expressed as:

$$E_{demag} = -\frac{1}{2} \int_V \vec{M}(\vec{r}) \cdot \vec{H}_{demag} dV \tag{2.5}$$

where $\vec{H}_{demag}$ is the demagnetization field given by $H_{demag} = -\frac{1}{4\pi} \int_V \frac{(\vec{r} - \vec{r}\,')\nabla \cdot \vec{M}(\vec{r}\,')}{|\vec{r} - \vec{r}\,'|^3} dV + \frac{1}{4\pi} \oint_A \frac{(\vec{r} - \vec{r}\,')\vec{M}(\vec{r}\,') \cdot \vec{n}(\vec{r}\,')}{|\vec{r} - \vec{r}\,'|^3} dA$ with dA the area element, $\vec{n}(\vec{r})$ the unit outward normal at position $\vec{r}\,'$. The first term for H_{demag} evaluates the field inside the entire volume, and the second term evaluates over the whole surface.

The dynamic evolution of magnetization is governed by the Landau-Lifshitz-Gilbert equation:

$$\frac{d\vec{m}}{dt} = -|\gamma|\vec{m}\times\vec{H}_{eff} + \frac{\alpha}{M_s}\left(\vec{m}\times\frac{d\vec{m}}{dt}\right) \tag{2.6}$$

where $\vec{H}_{eff}$ is the total effective field, γ is the Gilbert gyromagnetic ratio, and α is the damping constant. $\vec{H}_{eff}$ can be calculated from the total free energy density [Eq. (2.1)] using $\vec{H}_{eff} = -\frac{\partial E_{total}}{\partial \vec{M}}$. For AF, the generalized method is similar to that of FM as discussed above. The main difference is that in the case of AF, separate equations need to be used for the individual spin sub-lattices.

Both the static and dynamic magnetization can be calculated using openly accessible software such as the object oriented micromagnetic framework (OOMMF),[8] LLG Micromagnetics Simulator,[9] Nmag[10] and MuMax.[11] In this work, OOMMF was employed to simulate the magnetization distribution in patterned NiFe Hall bars for the calculation of planar Hall effect signal. OOMMF is an open-source micromagnetic simulation program developed and maintained by the National Institute of Standards and Technology (NIST). It is a finite element method based program that solves the LLG equation iteratively and obtains the time evolution of the magnetic configurations in FM. In practice, to simulate the magnetic configurations in a patterned magnetic structure, the FM element is first meshed into finite unit cells in each direction and then the magnetization direction in each cell is calculated numerically using the LLG equation. The physical input parameters are the exchange constant, the uniaxial anisotropy constant and the saturation magnetization. It should be noted that the cell sizes in x, y and z-directions strongly influence the simulation time and accuracy, and therefore, it is necessary to find a balance between precision and simulation time. Typically, the cell size is chosen to be comparable to the characteristic exchange length $l_{ex} = \sqrt{\frac{2A}{\mu_0 M_s^2}}$, which is usually on the order of a few nanometers.

2.2.4 Macro-spin model

Although the micromagnetic modelling is able to produce the spatial distribution of magnetization in various types of magnetic elements, it is usually very time consuming and also sensitive to the choice of parameters. In contrast, a macro-spin model is more useful in capturing the essential physics and is often sufficient for understanding the basic behavior of an FM or AF under an external field. In this section, we introduce the macro-spin model for both FM and AF, which will be used for interpretation of the experimental results in the following chapters.

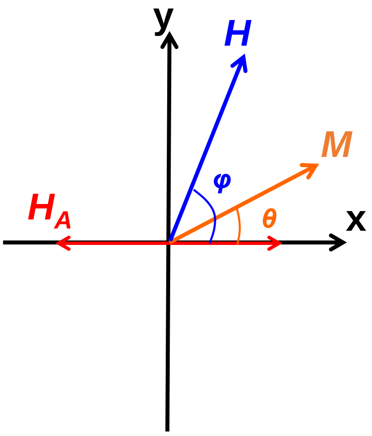

FIG. 2.3 Schematics of macro-spin model for FM with a uniform magnetization distribution.

a) FM under an external field

As illustrated in Fig. 2.3, a simple method to model an FM layer is the so-called macro-spin model, in which the FM is represented by a single element with uniform magnetization $\vec{M}$. Upon application of an external magnetic field H, $\vec{M}$ rotates coherently to align with the field. In other words, the FM is treated as a single magnetic domain. The macro-spin model can satisfactorily reproduced many experimental observations, for instance, the FM hysteresis loop. To determine the static equilibrium state of $\vec{M}$ in response to a particular H value at a specific direction, the free energy of an FM is minimized with respect to the magnetization direction. In the simplest case, the free energy of an FM can be written as the sum of anisotropy and Zeeman energy (ignoring all other energy terms):[12]

$$\begin{aligned} E &= -\vec{M}\cdot\vec{H} + K_u \sin^2\theta \\ &= -HM_s \cos(\varphi-\theta) + K_u \sin^2\theta \end{aligned} \tag{2.7}$$

where K_u is the uniaxial anisotropy constant, M_s is the saturation magnetization for $\vec{M}$, θ is the angle between the easy axis direction and $\vec{M}$, and φ is the angle between the easy axis and applied field directions. Note that the easy axis of FM in this example is fixed along the x-axis, and the demagnetization energy term is ignored for simplicity. The energy minimization requires:

$$\frac{\partial E}{\partial \theta} = -HM_s \sin\left(\varphi\text{-}\theta\right) + 2K_u \sin\theta\cos\theta = 0 \tag{2.8}$$

$$\text{and } \frac{\partial^2 E}{\partial \theta^2} > 0 \tag{2.9}$$

In general, one can find the solutions numerically for different φ values. In what follows, we consider two special cases for which the analytical solutions exist.

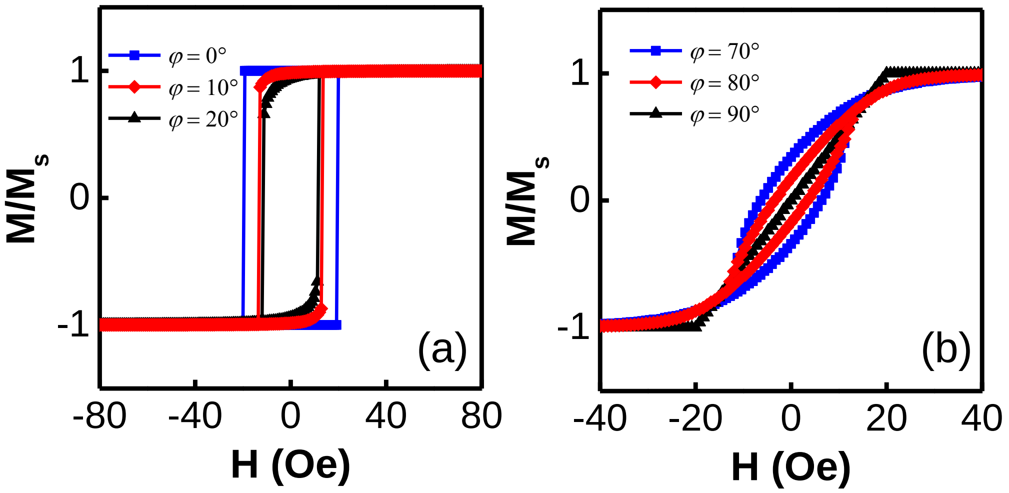

FIG. 2.4 (a) Simulated *M-H* curve with φ = 0˚, 10˚, 20˚. (b) Simulated *M-H* curve with φ = 70˚, 80˚, 90˚. The parameter used is: H_A = 10 Oe.

1) Case 1: $\varphi = 0$ (*i.e.*, the external field is applied in *x*-direction)

In this case, Eqs. (2.8) and (2.9) become:

$$HM_s \sin\theta + 2K_u \sin\theta\cos\theta = 0 \tag{2.10}$$

$$HM_s \cos\theta + K_u \cos 2\theta > 0 \tag{2.11}$$

We further divide both sides of the equation by M_s and define the anisotropy field as $H_A = K_u / M_s$, and the non-trivial solution can thus be obtained as $\theta = 0$ or $\theta = \pi$. This yields the square shaped hysteresis loop as illustrated in Fig. 2.4(a) (line with square).

2) Case 2: $\varphi = \pi / 2$ (*i.e.*, the external field is applied in *y*-direction)

In this case, Eqs. (2.8) and (2.9) become:

$$-HM_s \cos\theta + 2K_u \sin\theta\cos\theta = 0 \tag{2.12}$$

$$-HM_s \sin\theta + K_u \cos 2\theta > 0 \tag{2.13}$$

These two equations give the non-trivial solution as $\sin\theta = \dfrac{H}{2H_A}$ when $H \le 2H_A$, otherwise $\theta = \pi/2$; and yield the diagonal shaped hysteresis loop in Fig. 2.4(b) (line with triangle). For an arbitrary φ value, the numerically calculated loops are presented in Figs. 2.4(a) and (b).

b) AF under an external field

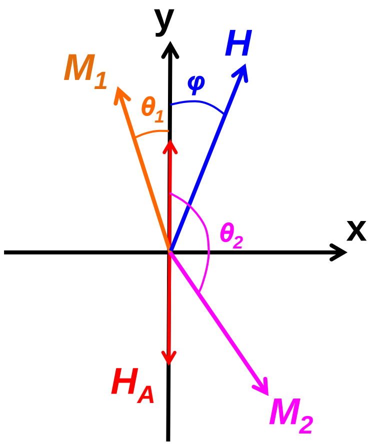

FIG. 2.5 Schematics of macro-spin model of AF with two sub-lattice magnetizations.

In analogy to FM, the spin configuration of AF under an external field can also be calculated using the macro-spin model. As illustrated in Fig. 2.5, for simplicity, the AF layer is assumed to be composed of two collinear sub-lattices with magnetizations $\vec{M}_1$ and $\vec{M}_2$, respectively, which are antiparallel exchange-coupled to each other at zero external field. When an external field is applied, $\vec{M}_1$ and $\vec{M}_2$ will deviate from their original anti-parallel configuration due to the finiteness of exchange coupling; their directions at the equilibrium state can thus be determined by minimization of the total energy density:[3]

$$\begin{aligned} E &= -(\vec{M}_1+\vec{M}_2)\vec{H}+K_u(\sin^2\theta_1+\sin^2\theta_2)+J\vec{M}_1\vec{M}_2 \\ &= JM_s{}^2\cos(\theta_1-\theta_2)-HM_s\cos(\varphi-\theta_1)-HM_s\cos(\varphi-\theta_2) \\ &+K_u(\sin^2\theta_1+\sin^2\theta_2) \end{aligned} \tag{2.14}$$

where J is the sub-lattice exchange constant, K_u is the uniaxial anisotropy constant, M_s is the saturation magnetization for $\vec{M}_1$ and $\vec{M}_2$, θ_1, θ_2 are the angles between y-direction and $\vec{M}_1$, $\vec{M}_2$, respectively, and φ is the angle between y-direction and applied field. The exchange and anisotropy field are defined as $H_{ex}=JM_s$ and $H_A=K_u/M_s$, respectively. Here, we assume that $|\vec{M}_1|=|\vec{M}_2|=M_s$. The energy minimization method requires:

$$\frac{\partial E}{\partial\theta_1}=-JM_s{}^2\sin(\theta_1-\theta_2)-HM_s\sin\left(\varphi\text{-}\theta_1\right)+2K_u\sin\theta_1 cos\theta_1=0 \tag{2.15}$$

$$\frac{\partial E}{\partial\theta_2}=-JM_s{}^2\sin(\theta_1-\theta_2)-HM_s\sin\left(\varphi\text{-}\theta_2\right)+2K_u\sin\theta_2 cos\theta_2=0 \tag{2.16}$$

$$\text{and } \frac{\partial^2E}{\partial\theta_1^2}>0,\ \frac{\partial^2E}{\partial\theta_1^2}\frac{\partial^2E}{\partial\theta_2^2}-\left[\frac{\partial^2E}{\partial\theta_1\partial\theta_2}\right]^2>0 \tag{2.17}$$

Similarly, we discuss two special cases for which there exist analytical solutions.

1) Case 1: $\varphi=0$ (*i.e.*, the external field is applied in y-direction)

In this case, when H is small, $\vec{M}_1$ and $\vec{M}_2$ should remain in the original direction, *i.e.*, $\theta_1=0$, $\theta_2=\pi$. When H increases to a critical value, spin flop will occur, leading to a configuration such that $\theta_1=-\theta_2$. The equilibrium state of $\vec{M}_1$ and $\vec{M}_2$ can be found by substituting $\varphi=0$ and $\theta_1=-\theta_2$ into Eq. (2.15); this leads to

$$\frac{\partial E}{\partial \theta_1} = -JM_S{}^2 \sin(\theta_1 - \theta_2) + HM_S \sin\theta_1 + 2K_u \sin\theta_1 cos\theta_1 = 0 \tag{2.18}$$

The nontrivial solution of Eq. (2.18) is

$$\cos\theta_1 = \frac{H}{2H_{ex} - 2H_A} \tag{2.19}$$

The second derivative is

$$\frac{\partial^2 E}{\partial \theta_1^2} = -4JM_S{}^2 \cos 2\theta_1 + 2HM_S \cos\theta_1 + 4K_u \cos 2\theta_1 \tag{2.20}$$

Substituting Eq. (2.19) into Eq. (2.20), we obtain

$$\frac{\partial^2 E}{\partial \theta_1^2} = \frac{4M_s\left[-H^2 + (2H_{ex} - 2H_A)^2\right]}{2H_{ex} - 2H_A} \tag{2.21}$$

From Eqs. (2.19) and (2.21), we can derive the equilibrium values of θ_1 and θ_2 which are given by

$$\cos\theta_1 = \cos\theta_2 = \frac{H}{2H_{ex} - 2H_A} \tag{2.22}$$

The corresponding energy minimum is

$$E = \frac{M_s\left[-H^2 + (2H_A - H_{ex})(2H_{ex} - 2H_A)\right]}{2H_{ex} - 2H_A} \tag{2.23}$$

Compare this energy term with the energy at antiparallel configuration (*i.e.*, $\theta_1 = 0$, $\theta_2 = \pi$),

$$E_0 = -JM_s{}^2 = -M_s H_{ex} \tag{2.24}$$

one obtains the field range for spin-flopped configuration (*i.e.*, $E \le E_0$)

$$\sqrt{2H_A(2H_{ex} - 2H_A)} \le H \le 2H_{ex} - 2H_A \tag{2.25}$$

At field $H < \sqrt{2H_A(2H_{ex} - 2H_A)}$, $\vec{M}_1$ and $\vec{M}_2$ remain in the anti-parallel configuration.

2) Case 2: $\varphi = \pi/2$ (*i.e.*, the external field is applied in *x*-direction)

In this case, as the angle between applied external field and *y*-direction is $\pi/2$, we can assume that during the sweeping process of the external field, condition $\theta_1 = \pi - \theta_2$ maintains all the time. Substitute $\varphi = \pi/2$ and $\theta_1 = \pi - \theta_2$ into Eq. (2.15), we obtain

$$\frac{\partial E}{\partial \theta_1} = 2JM_s^2 \sin\theta_1 \cos\theta_1 - HM_s \cos\theta_1 + 2K_u \sin\theta_1 cos\theta_1 = 0 \tag{2.26}$$

The nontrivial solution of Eq. (2.26) is

$$\sin\theta_1 = \frac{H}{2H_{ex} + 2H_A} \tag{2.27}$$

Substitute Eq. (2.27) into the second derivative

$$\frac{\partial^2 E}{\partial \theta_1^2} = 2JM_s^2 \cos 2\theta_1 + 2HM_s \sin\theta_1 + 2K_u \cos 2\theta_1 \tag{2.28}$$

one obtains

$$\frac{\partial^2 E}{\partial \theta_1^2} = \frac{M_s\left[-H^2 + (2H_{ex} + 2H_A)^2\right]}{2H_{ex} + 2H_A} \tag{2.29}$$

From Eqs. (2.27) and Eq. (2.29), θ_1 and θ_2 at equilibrium state are derived as $\sin\theta_1 = \frac{H}{2H_{ex} + 2H_A}$. When $H \geq 2H_{ex} + 2H_A$, the AF layer becomes saturated at the direction of external field.

In the above two cases, the overall magnetization of AF along external field direction is given by $\vec{M} = \vec{M}_1 + \vec{M}_2$. Figs. 2.6(a) and (b) show the calculated *M-H* curves for the two special cases as well as other cases with different φ values, *i.e.*, φ = 2.5°, 5°, 80° and 85°, respectively. Fig. 2.6(a) shows that, when the applied field is nearly parallel to the *y*-direction, the magnetization of AF is small at a small external field

($H \le \sqrt{2H_A(2H_{ex}-2H_A)}$), then increases almost linearly with increasing external field ($\sqrt{2H_A(2H_{ex}-2H_A)} \le H \le 2H_{ex}-2H_A$) and finally becomes almost saturated at $H \ge 2H_{ex}-2H_A$. Spin flop occurs at field $H \ge H_{sf} = \sqrt{2H_A(2H_{ex}-2H_A)}$ when φ is near 0°, while such behavior becomes less obvious when φ becomes larger and finally vanishes when it approaches 90° as shown in Fig. 2.6(b).

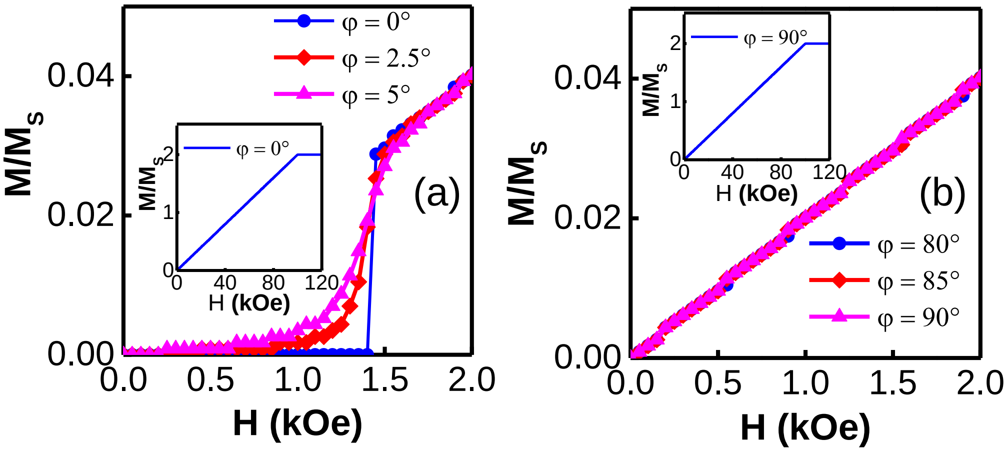

FIG. 2.6 (a) Simulated magnetization of AF when φ is near 0°; (b) Simulated magnetization of AF when φ is near 90°. The insets in (b) and (c) show the *M-H* curve at large field range. The parameters used are: H_A = 10 Oe, H_{ex} = 50 kOe.

2.3 Spin and spin-dependent charge transport

2.3.1 Spin current

Before proceeding to the discussion of transport phenomenon in magnetic materials, it is desirable to clarify the concepts of spin current and charge current. Electrons have an intrinsic degree of freedom, *i.e.*, the spin. It is a quantum mechanical observable described by the spin angular momentum operator as follow:

$$\vec{S} = \frac{\hbar}{2}\vec{\sigma} \tag{2.30}$$

where $\hbar$ is Planck's constant, and $\vec{\sigma}$ is the Pauli matrix with $\vec{\sigma}_x = \begin{pmatrix} 0 & 1 \\ 1 & 0 \end{pmatrix}, \vec{\sigma}_y = \begin{pmatrix} 0 & -i \\ i & 0 \end{pmatrix}, \vec{\sigma}_z = \begin{pmatrix} 1 & 0 \\ 0 & 1 \end{pmatrix}$. The electron spin is directly related to the magnetic moment

$$\vec{\mu} = -g\mu_B \frac{\vec{S}}{\hbar} \tag{2.31}$$

where g is electron g-factor and μ_B is the Bohr magneton. As can be seen from Eq. (2.31), the magnetic moment of electron is antiparallel to its spin angular momentum. The flow of the electron spin angular momentum leads to a spin current (j_s), whereas the flow of charges leads to an electric charge current (j_c):

$$j_c = j_\uparrow + j_\downarrow, j_s = -\frac{\hbar}{2e}(j_\uparrow - j_\downarrow) \tag{2.32}$$

As shown in Eq. (2.32) below, a charge current is the sum of spin up and spin down electrons, whereas the spin current is their difference. The pre-factor $-\frac{\hbar}{2e}$ in the spin current is due to the fact that one electron carries a spin angular momentum of $\frac{\hbar}{2}$, and it carries a charge of $-e$.

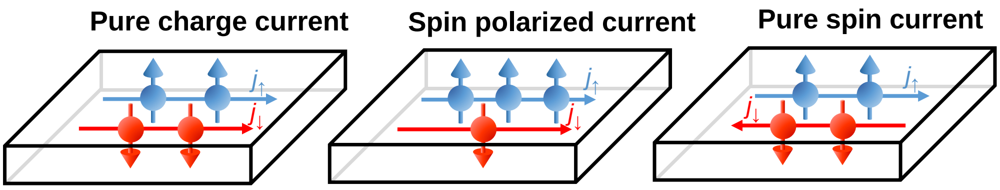

FIG. 2.7 Schematics of charge current, spin polarized current and pure spin current. Figure adapted from Ref. [13].

Fig. 2.7 illustrates three types of current. In the first case, where both $j_\uparrow$ and $j_\downarrow$ are equal and propagate in the same direction, there is a net charge transport without a net spin transport. Therefore, this is called charge current.

This is often the situation in paramagnetic conductor without spin-orbit coupling. In the second case, where the current density of one type of spin is larger than the other (here $j_\uparrow > j_\downarrow$), both charge and spin current are present. Therefore, it is called a spin-polarized current which widely exists in ferromagnetic conductors. In the last case, where $j_\uparrow$ and $j_\downarrow$ are equal but propagate in the opposite direction; this results in a net spin transport without a net charge current. Therefore, it is called pure spin current, corresponding to a pure flow of spin angular momentum.

2.3.2 Anisotropic magnetoresistance (AMR)

In metals, the field-dependent longitudinal resistance change is called ordinary magnetoresistance (OMR).[14] The resistance increases as the external magnetic field ($\vec{H}$) increases, which is due to the cycloidal motion of electrons by the field induced Lorentz force. The resistance change scales with $\left|\vec{H}\right|^2$, and is larger when the field is perpendicular to the current flow ($\vec{H} \perp \vec{j}$) and smaller when the field and current flow are parallel to each other ($\vec{H} \parallel \vec{j}$). OMR is generally present in in all types of metals including nonmagnetic (NM), FM and AF.

In FM metals, additional interactions take place between the magnetization ($\vec{M}$) and conduction electrons, which gives rise to the dominant contribution to the observed MR effect, *i.e.*, the anisotropic magnetoresistance (AMR).[15] For AMR, the resistivity is maximum ($\rho_\parallel$) when $\vec{M} \parallel \vec{j}$ and minimum ($\rho_\perp$) when $\vec{M} \perp \vec{j}$. It arises from the scattering between the *s* electrons and 3*d* orbitals near the Fermi surface. As illustrated in Fig. 2.8, the scattering cross-section is larger when $\vec{M} \parallel \vec{j}$ and smaller when $\vec{M} \perp \vec{j}$, which gives the resistivity change upon reorienting the magnetization direction. Phenomenologically, the AMR can be described by the following expression:

$$\rho_{xx} = \rho_{\perp} + (\rho_{\parallel} - \rho_{\perp})\cos^2\varphi \sin^2\theta \tag{2.33}$$

where $\rho_{\parallel}$ and $\rho_{\perp}$ correspond to the case when $\vec{M}$ is parallel or perpendicular to $\vec{j}$, respectively, and θ and φ are the polar and azimuthal angle of $\vec{M}$ with respect to $+z$ and $+x$ direction, respectively.

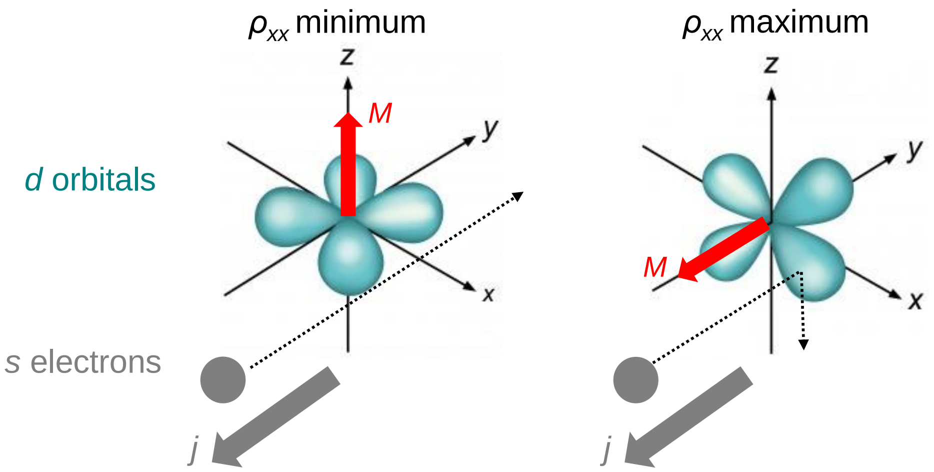

FIG. 2.8 Schematics of the origin of the AMR and PHE in FM. For $\vec{M} \parallel \vec{j}$, the larger scattering cross-section gives higher resistance (right); for $\vec{M} \perp \vec{j}$, the smaller scattering cross-section gives lower resistance (left).

In addition, geometrical confinement can also contributes to the MR effect, known as the geometrical size effect (GSE). It has been reported in polycrystalline Co thin films, *i.e.*, $\rho_y > \rho_z$,[16] which should be equal to each other based on the above AMR consideration. One explanation is that when the film thickness is lower than the mean free path of electrons, the plane perpendicular to $\vec{M}$ where electrons can travel with lower resistance, is unconstrained along x but constrained along z when $\vec{M} \parallel \vec{y}$. This slightly increases the resistance as compared to the situation when $\vec{M} \parallel \vec{z}$, where both x and y are unconstrained. Another MR effect in FM metals is called the spin-disorder MR,[17] which results in a decrease in the resistance almost linearly proportional to $\vec{H}$, regardless of its direction. The suppression of spin disorder is induced by low energy magnons, which consequently diminishes the electron-magnon scattering.

2.3.3 Hall effect

Besides the longitudinal magnetoresistance, the longitudinal charge current can also induce a transverse spin and/or charge accumulation, due to off-diagonal elements in the conductivity tensor. These effects are in general named after Edwin Hall, who discovered that the Lorentz force bends the current carrying charges towards the transverse edges of the conductor when a perpendicular magnetic field is applied. To equilibrate the Lorentz force, a net transverse voltage builds up between the two edges. This is commonly referred as the ordinary Hall effect (OHE).[18]

In FM, in addition to OHE, the presence of $\vec{M}$ can induce an anomalously large transverse voltage, which is usually called anomalous Hall effect (AHE).[19] The AHE depends on the out-of-plane component of the magnetization ($M_z = |\vec{M}|\cos\theta$). It is usually much larger as compared to OHE (which depends on $\vec{H}$), because of the large carrier density and small OHE coefficient in metals. However, although it is generally believed that the side jump, skew scattering and intrinsic effects are equally valid for the emergence of the AHE in FM,[20] the origin of the AHE is still under debate since the role and relative weightage of each mechanism on the AHE are difficult to be quantified.

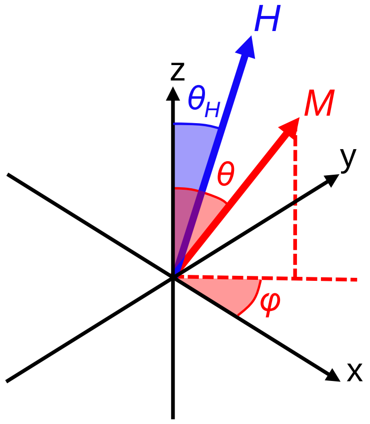

FIG. 2.9 Schematics of the magnetization and external field directions.

Another Hall effect in FM is the planar Hall effect (PHE). Despite "Hall effect" in its name, it actually has the same origin as AMR.[15] It is the transverse manifestation of AMR when the scattering of conduction electrons from the *d*-orbitals have a transverse preferential direction depending on the in-plane component of $\vec{M}$ with respect to $\vec{j}$. Due to this in-plane angle dependence, the name "planar" was coined to the effect. Following the coordinate notion in Fig.2.9, by considering all three effects we can write the following general formula (in terms of directly measurable parameters) to describe the angular dependence of the transverse (Hall) resistance:

$$R_H = \frac{V_H}{I} = R_{AHE}\cos\theta + R_{PHE}\sin^2\theta\sin 2\varphi + R_{OHE}H\cos\theta_H \qquad (2.34)$$

where θ_H is the external field angle with respect to the z axis, R_{AHE}, R_{PHE}, and R_{OHE} are the coefficient for AHE, PHE and OHE, respectively. It should be noticed that in this work, OHE (or OMR) is several orders of magnitude smaller than AHE and PHE (or AMR) within the field range used throughout the study (less than 30 kOe), therefore, it is safe to neglect their contribution in the discussion presented later.

2.4 Spin orbit coupling

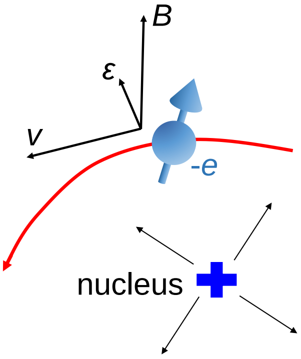

FIG. 2.10 Semi-classical picture of spin orbit coupling.

Spin orbit coupling (SOC) is a relativistic effect. A simple semi-classical picture of SOC is illustrated in Fig. 2.10: an electron (with charge -*e*) orbiting around a nucleus with a velocity ($\vec{v}$) experiences the presence of an effective magnetic field $\vec{B}_{eff} = -\frac{\vec{v}\times\vec{\varepsilon}}{c}$ in its rest-frame, with *c* the speed of light, $\vec{\varepsilon}$ the radial electric field created by the nucleus. Induced by this effective field, the electron possesses a momentum-dependent Zeeman energy:

$$H_{SOC} = -\vec{\mu}\cdot\vec{B}_{eff} = -\left(-\frac{e}{m_e c}\vec{S}\right)\cdot\left(-\frac{\vec{v}\times\vec{\varepsilon}}{c}\right) \tag{2.35}$$

where $\vec{\mu}$ is the magnetic moment and is associated to the spin angular momentum $\vec{S}$ by Eq. (2.31). In solids, the electric field can be replaced by $\vec{\varepsilon} = \vec{\nabla}V(r)/e$, where $V(r)$ is the Coulomb potential energy. For the centrally symmetric case in Fig. 2.10, $V(r)$ can be written as $V(r) = -e^2/r$, and therefore $\vec{\varepsilon}$ has the form of $\vec{\varepsilon} = (e/r^3)\vec{r}$. Substitute $\vec{\varepsilon}$ into Eq. (2.35), it can be obtained:

$$H_{SOC} = \frac{e^2}{m_e c^2 r^3} [\vec{S} \cdot (\vec{r} \times \vec{v})] \tag{2.36}$$

The factor $(\vec{r} \times \vec{v})$ can be replaced by the orbital angular momentum $\vec{L}$, and thus Eq. (2.36) becomes:

$$H_{SOC} = \frac{e^2}{m_e^2 c^2 r^3} \vec{S} \cdot \vec{L} \tag{2.37}$$

The more correct derivation after taking into the relativistic correction into consideration yields the insertion of a factor of two as follow:[21]

$$H_{SOC} = \frac{e^2}{2m_e^2 c^2 r^3} \vec{S} \cdot \vec{L} \tag{2.38}$$

For more general case in solids, SOC is given by:[21]

$$H_{SOC} = \frac{1}{2m_e^2 c^2} [\vec{\nabla} V(\vec{r}) \times \vec{p}] \cdot \vec{S} \tag{2.39}$$

where $V(\vec{r}) = V_{cr}(\vec{r}) + V_{ap}(\vec{r})$ is the total potential including periodic crystal potential $V_{cr}(\vec{r})$ and aperiodic potential $V_{ap}(\vec{r})$ induced by impurities, external electric field, confinement and boundaries.[22] One then tries to eliminate $V_{cr}(\vec{r})$ as much as possible and to describe the charge carriers in terms of the band structure.

2.4.1 The Rashba effect

In quantum well (or certain metallic surfaces) with structural inversion asymmetry along the growth direction $\vec{z}$, the spin sub-bands are split in energy. Such band splitting was explained by Rashba considering an electric field $\vec{\varepsilon} = \varepsilon_z \vec{z}$ resulting in an effective SOC of the form:[23]

$$H_{Rashba} = \frac{\alpha_R}{\hbar} (\vec{z} \times \vec{p}) \cdot \vec{\sigma} \tag{2.40}$$

where $\alpha_R = \frac{g\mu_B\varepsilon_z}{2m_e c^2}$ is the Rashba constant dependent on material properties. In two-dimensional (2D) systems with electrons confined to move in the *xy*-plane, Eq. (2.40) can be further simplified to:[23]

$$H_{Rashba} = \frac{\alpha_R}{\hbar}(k_y\sigma_x - k_x\sigma_y) \tag{2.41}$$

The Rashba effect aligns the spins of conduction electrons on the Fermi surface to a certain configuration. Upon applying an external electric field, the Fermi surface is shifted in *k* space, which gives rise to non-equilibrium spin densities. In FMs, these spin polarizations of *s* electrons further interact with the magnetic ordered *d* electrons through *s*-*d* coupling, acting as exerting an effective magnetic field onto them. The effective field can be expressed as:[24,25]

$$\delta\vec{H}_{eff} = -\frac{J_{sd}}{g\mu_B}\delta\vec{S} \tag{2.42}$$

where $\delta\vec{S}$ is the non-equilibrium spin polarizations, J_{sd} is the exchange constant between *s* and *d* electrons. In this way, $\vec{M}$ can be manipulated by the Rashba effect through applying a current over FM.

2.4.2 The spin Hall effect

The spin Hall effect is the conversion of a flow of charge current into a flow of pure spin current, *i.e.*, a net spin flow without charge flow, transverse to the charge current flow direction. It was first predicted by D’yakonov and Perel’ back in 1971,[26] and was rediscovered by Hirsch in 1999.[27] Phenomenologically, SHE is expressed as follows:

$$\vec{j}_s = \theta_{SH}\vec{\sigma}\times\vec{j}_c \tag{2.43}$$

where θ_{SH} is the spin Hall angle defined as $\theta_{SH} = \frac{\sigma_s}{\sigma_c}\frac{e}{\hbar}$ with σ_s, σ_c as spin

Hall conductivity and charge conductivity, respectively. Unlike Rashba effect, SHE can be present in bulk materials. Table 2.2 summarizes the experimentally reported θ_{SH} values in different metals.

TABLE 2.2 Summary of the spin Hall angles for common metals obtained experimentally. Table adapted from Ref. [28].

Material	Temperature (K)	θ_{SH} (%)	σ_s $(\frac{\hbar}{e}\frac{10^3}{\Omega m})$
Al	4.2	0.02 ± 0.01	17
Au	293	0.33 – 11	5.3 – 37
Bi	3	> 0.8	0.0247
Mo	293	-0.05	-2.3 ± 0.5
Nb	10	-0.87 ± 0.2	-10 ± 2
Pd	293	0.64 – 1.4	20 – 37
Pt	293	1.2 – 8	20.51 – 570
Ta	293	-12 – -2	-63 – -0.4
W	293	-33	-127 ± 23

The SHE in solids can have either extrinsic or intrinsic origin.[28,29] The former originates from either skew scattering or side jump mechanism. The skew scattering is caused by asymmetric scattering of electrons by a central potential in the presence of spin orbit interaction, such as impurities. It can be understood phenomenologically as the defection of electron by an effective magnetic field gradient when it passes by the nucleus of the impurity atom. As shown schematically in Fig. 2.11 (a) for a 2D case, depending on the spin direction (up or down), the field gradient will deflect electrons towards two sides of the original incident direction; this will lead to SHE. On the other hand, side jump is originating from the anomalous form of the velocity operator in spin orbit coupled systems, which is spin-dependent [see Fig. 2.11(b)]. Although this displacement caused by a single scattering event due to the anomalous velocity is on the order of Å, multiple scattering events add up, leading to spin accumulation at the edges of a conductor on a global scale as observed experimentally.

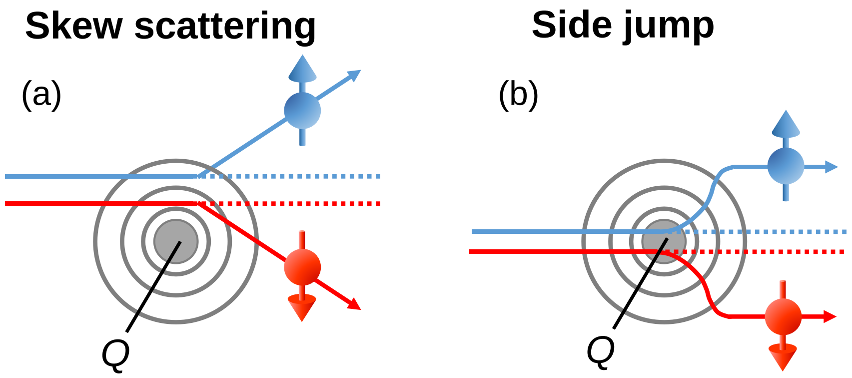

FIG. 2.11 (a) Skew scattering at an impurity with charge Q; (b) Side jump scattering at an impurity with charge Q resulting in a spin dependent displacement. Figure adapted from Ref. [13].

In the case of intrinsic SHE, the spin dependent transverse displacement is not caused by scattering, but comes from the electronic band structure. Such intrinsic contribution can be expressed in terms of Berry curvature $\Omega_n^z(\vec{k})$:[28,30]

$$\sigma_s = \frac{e}{\hbar}\sum_{\vec{k}} \Omega^z(\vec{k}) = \frac{e}{\hbar}\sum_{\vec{k}}\sum_{n} f_{\vec{k}n}\Omega_n^z(\vec{k}) \qquad (2.44)$$

where $f_{\vec{k}n}$ is the Fermi distribution function for the n^{th} band at $\vec{k}$. $\Omega_n^z(\vec{k})$ can be viewed as the effective magnetic field in k space generated by a Dirac magnetic monopole. $\Omega_n^z(\vec{k})$ is defined as $\Omega_n^z(\vec{k}) = \nabla \times A_n^z(\vec{k})$, where $A_n^z(\vec{k}) = -\mathrm{Im}\langle u_k | \nabla_k | u_k \rangle$ is the Berry vector potential, u_k the carrier wavefunction. In analogy to electrodynamics, the Berry curvature can thus be viewed as the effective magnetic field in *k*-space generated by a Dirac magnetic monopole. Associated with it is the line integral of Berry vector potential $\phi = \oint A_n^z(\vec{k}) \cdot d\vec{k}$ called Berry phase. According to Stokes's theorem, it can be alternatively written as a surface integral of Berry curvature $\phi = \int \Omega_n^z(\vec{k}) \cdot dk_x dk_y$. Once an electric field (or charge current) is applied, it causes a linear variation in $\vec{k}$. In this case, a closed path is realized when $\vec{k}$ sweeps the entire Brillouin zone.[30] The carriers travel in such a closed path experiences a phase change, and feels an effective magnetic field given by the flux of the monopole through the surface subtended by the path. This magnetic field in turn induces spin dependent anomalous transverse velocity for carriers, and leads to the separation of spins in the transverse direction, *i.e.* the so-called SHE. Following the Berry curvature mechanism, the intrinsic spin Hall conductivity has been calculated for 4*d* and 5*d* metals.[31,32] The results turned out to follow Hund's rule, *i.e.*, the spin Hall conductivity is positive for more than half-filling and negative for less than half-filling of the *d*-bands.

2.5 Spin orbit torque

As discussed above, spin current can be generated either inside an FM with bulk inversion asymmetry or in FM/HM hetero-structure. In both cases, the spin angular momentum is transferred from the conduction electrons to the FM magnetization. The transfer can be understood as the absorption of the transverse component of non-equilibrium spin densities ($\vec{\sigma} \perp \vec{M}$) by the magnetization, and thus exerts on a torque onto it. Since it utilizes SOC to create non-equilibrium spin densities or spin current, the resultant torque is named as spin orbit torque (SOT).

To the best of our knowledge, the first experimental observation of SOT was reported by Chernyshov et al.[33] for $Ga_{0.94}Mn_{0.06}As$ dilute magnetic semiconductor (DMS) with a Curie temperature of 80 K. The $Ga_{1-x}Mn_xAs$ layer grown epitaxially on GaAs (001) substrate is compressively strained, which results in a bulk inversion asymmetry. In metallic FMs, such intrinsic bulk inversion asymmetry is difficult to realize. Miron et al.[34] reported the first observation of a current-induced SOT in a thin Co layer sandwiched by a Pt and an AlO_x layer. One explanation is based on the surface inversion asymmetry, which comes from the difference in the Co interfaces with Pt and AlO_x. The electrons in the Co layer thus experiences a large Rashba effect, leading to sizable current-induced SOT. On the other hand, the presence of Pt also gives rise to pure spin current generated from SHE. In addition to the Rashba effect, spin current diffused from the Pt layer can also exert a torque on the FM layer. Nevertheless, following the first report, the SOT has been demonstrated in a wide variety of FM/HM systems with FMs such as CoFeB,[35-39] Fe,[40] NiFe,[41] etc. and HMs such as Pt and Ta.

As discussed in Sec 2.2.3, the magnetization of FM can be described by the general LLG equation [see Eq. (2.6)], including precession and damping terms. Despite the debatable origin of SOT, it is usually phenomenologically expressed as field-like and antidamping-like terms in the LLG equation:[39,42]

$$\frac{d\vec{m}}{dt} = -|\gamma|\vec{m}\times\vec{H}_{eff} + \frac{\alpha}{M_s}\left(\vec{m}\times\frac{d\vec{m}}{dt}\right) + a_j\vec{m}\times(\vec{m}\times\vec{\sigma}) + b_j\vec{m}\times\vec{\sigma} \qquad (2.45)$$

where a_j and b_j correspond to the antidamping-like and field-like torque coefficient, respectively. $\vec{H}_{eff}$ can calculated from the free energy density using $\vec{H}_{eff} = -\frac{\partial E_{total}}{\partial \vec{M}}$. In this way, the current induced SOT effective field is decomposed into two terms $\vec{H}_{SOT} = \vec{H}_{DL} + \vec{H}_{FL}$, where $\vec{H}_{DL} = a_j \vec{m} \times \vec{\sigma}$ is the antidamping-like effective field, and $\vec{H}_{FL} = b_j \vec{\sigma}$ is the field-like effective field. As can be seen, the $\vec{H}_{DL}$ depends on the local magnetization direction whereas $\vec{H}_{FL}$ only depends on the spin polarization direction of the spin current. In principle, the magnitude of a_j and b_j may depend on the angle of $\vec{M}$ and $\vec{\sigma}$, while generally they are treated as constant for simplicity in both theoretical and experimental works. To determine the SOT effective fields, various methods have been proposed, including but not limited to, field sweeping second harmonic method,[43,44] 2nd order PHE method,[38,41] angle-dependent MR or Hall measurement.[40,42] The first method is more suitable for perpendicular anisotropy FM due to the approximation used in the derivation, while the others are proposed for FM with in-plane anisotropy. In this dissertation, the FeMn/Pt bilayers or FeMn/Pt multilayers are of in-plane anisotropy, therefore the main method we adopted to quantify SOT is the second order PHE measurement. A detailed description on the experimental method will be discussed in Chapter 3.

Another point to note is that recent experimental results have found that SHE may play a bigger role than Rashba effect in FM/HM bilayers,[36,40,41,45] especially when the FM layer is thick. One consideration is that without the third oxide layer, the inversion asymmetry in the structure is weak since the work function between metals are generally close to each other as compared to that between metal and oxide.[46] Another consideration is based on the interfacial nature of Rashba effect, whose magnitude is expected to decrease as the thickness of FM increases. This has been further supported by the fact that the observed effective field directions are opposite to each other in Pt and Ta based bilayers with a same FM,[40,41] in consistency with the opposite spin Hall angle for the two HMs. Considering the fact the structures in this work are also metallic ones similar to that in Ref. [41], to simplify the treatments, the discussion and analysis in this dissertation (Chapter 4 - 6) are carried out mainly based on the SHE scenario.

2.6 Spin Hall magnetoresistance

In addition to SOT, an unconventional MR effect has also been reported in FM/HM bilayers, particularly YIG/HM.[47-49] One possible explanation of the effect is associated with the simultaneous actions of SHE and its inverse effect [inverse spin Hall effect (ISHE)].[50] This explanation has been working well with many experimental observations.[48,51-64] As depicted in Fig. 2.12, when the spin current generated from HM reaches the FM/HM interface, depending on the angle between $\vec{M}$ and $\vec{\sigma}$, a certain portion of the spin current is reflected back into HM with the remaining traveling across the interface and absorbed by FM. The reflection is maximum when $\vec{M} \parallel \vec{\sigma}$ and minimum when $\vec{M} \perp \vec{\sigma}$. The absorbed spin current interacts with $\vec{M}$, leading to SOT as discussed in the last section. The reflected spin current $j_s^{(ref.)}$ is converted to a charge current $j_c^{(ISHE)}$ in HM through ISHE which flows in the opposite direction of the original current j_c. As a consequence, the longitudinal resistance of HM is modulated by the direction of $\vec{M}$, leading to the appearance of SMR given by $\rho_{xx} = \rho_0 - \Delta\rho(\vec{m}\cdot\vec{\sigma})^2$, where ρ_{xx} is the longitudinal resistivity, $\vec{m}$ the unit vector of magnetization, ρ_0 the isotropic longitudinal resistivity, and $\Delta\rho$ the

SMR induced resistivity change. If we assume the charge current is in x-direction, $\vec{\sigma}$ lies in y-direction, and the SMR can be rewritten as:

$$\rho_{xx} = \rho_0 - \Delta\rho \sin^2\varphi \sin^2\theta \tag{2.46}$$

As can be seen, SMR has an angle dependence on magnetic field which is qualitatively different from the conventional AMR in Eq. (2.33). Therefore, the widely adopted experimental method to distinguish the two effects is the angle-dependent MR measurement, which will be discussed in Chapter 3.

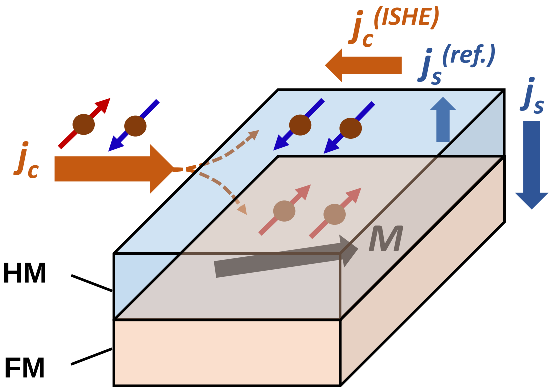

FIG. 2.12 Schematics of the SMR effect based on the simultaneous actions of SHE and ISHE in FM/HM bilayers.

Other than YIG based structures, SMR has also been reported in a variety of FM/HM bilayers with the FMs including both ferromagnetic insulators such as $CoFe_2O_4$,[59] $NiFe_2O_4$,[51] Fe_3O_4[60] and $LaCoO_3$[65] and FM metals, *e.g.*, Co,[61] CoFeB,[63] and NiFe,[66] and the HMs including Pt, Pd, Ta, and Ru. Besides FMs, it has also been observed in $SrMnO_3$/Pt in which $SrMnO_3$ is an AF insulator.[67] In addition to ISHE, magnetic proximity effect[47] and interfacial AMR from spin dependent scattering at FM/HM interface,[68] and Hanle effect in HM itself,[69] may also give rise to similar experimental observations. But so far, most experimental results seem to support the ISHE mechanism. As will be discussed in the later chapters, we have observed both SOT and SMR in FeMn/Pt based systems, which corroborate well with the analysis based on the SHE/ISHE scenario.

2.7 Drift-diffusion formalism

The spin transport in FM/HM bilayers can be modelled semi-classically using the drift-diffusion formalism.[70] The main idea is that SHE in the HM layer drives spins with different polarization direction to accumulate at opposite surfaces of the HM; this results in difference in electrochemical potential for spin-up and spin-down electrons. The difference in electrochemical potential in turn causes electrons to drift so that the net spin current will be zero at the surfaces. In the case of FM/HM bilayers, the spin current will be zero at only one surface and at the other surface a finite amount of spin current will be absorbed by the FM layer. The driving force causing the drift is given by $\vec{F} = -\nabla \mu_{\uparrow(\downarrow)}$, where $\mu_{\uparrow(\downarrow)}$ is the spin-dependent electrochemical potential, and is defined as $\mu_{\uparrow(\downarrow)} = \mu_{ch,\uparrow(\downarrow)} - e\phi$. Here $\mu_{ch,\uparrow(\downarrow)}$ and ϕ are the spin-dependent chemical potential and electric potential, respectively. For small deviations from the equilibrium, $\mu_{ch,\uparrow(\downarrow)} = n_{\uparrow(\downarrow)} / N_{\uparrow(\downarrow)}$, where $n_{\uparrow(\downarrow)}$ is the carrier density, and $N_{\uparrow(\downarrow)}$ is the (spin-resolved) density of states at the Fermi energy. Following these definitions and after taking into account SHE and its Onsager's reciprocal ISHE, the current density (both charge and spin) in the HM layer of the FM/HM bilayers can be rewritten as:[50]

$$\begin{pmatrix} \vec{j}_c \\ \vec{j}_{sx} \\ \vec{j}_{sy} \\ \vec{j}_{sz} \end{pmatrix} = \sigma \begin{pmatrix} 1 & \theta_{SH}\vec{x}\times & \theta_{SH}\vec{y}\times & \theta_{SH}\vec{z}\times \\ \theta_{SH}\vec{x}\times & 1 & 0 & 0 \\ \theta_{SH}\vec{y}\times & 0 & 1 & 0 \\ \theta_{SH}\vec{z}\times & 0 & 0 & 1 \end{pmatrix} \begin{pmatrix} -\nabla\mu_0/e \\ -\nabla\mu_{sx}/(2e) \\ -\nabla\mu_{sy}/(2e) \\ -\nabla\mu_{sz}/(2e) \end{pmatrix} \tag{2.47}$$

where $\vec{j}_{si}$ is the spin current polarized in *i*-direction ($i = x$, y or z), $\vec{j}_s^{\,j}$ is the spin current following in *j*-direction ($j = x$, y or z), σ is the conductivity of HM, θ_{SH} is the spin Hall angle of HM, $\mu_0 = e\phi$ is the charge chemical potential, $\vec{\mu}_s = \vec{\mu}_\uparrow - \vec{\mu}_\downarrow$ is the spin accumulation and $\vec{\mu}_s = (\mu_{sx}, \mu_{sy}, \mu_{sz})^T - \mu_0\vec{I}$ with $\vec{I}$ the unity vector. The external electric field, $\vec{\varepsilon} = \varepsilon_x\vec{x}$, is applied in *x*-direction (charge current $j_c^0 = \sigma\varepsilon_x$). In the case of thin film, due to the finite spin diffusion length of HM (usually on the order of nm), there is only net SHE spin current flow in *z*-direction with polarization in *y*-direction. In this case, Eq. (2.47) can be simplified as:

$$\begin{pmatrix} j_{sx}^z \\ j_{sy}^z \\ j_{sz}^z \end{pmatrix} = -\frac{\sigma}{2e}\partial_z \begin{pmatrix} \mu_{sx} \\ \mu_{sy} \\ \mu_{sz} \end{pmatrix} - \begin{pmatrix} 0 \\ \theta_{SH} j_c\vec{x} \\ 0 \end{pmatrix} \tag{2.48}$$

The spin accumulation follows the diffusion equation $\nabla^2\vec{\mu}_s = \frac{\vec{\mu}_s}{\lambda_N{}^2}$ where λ_N is the spin diffusion length of HM expressed as $\lambda_N = \sqrt{D\tau_{sf}}$ in terms of the charge diffusion constant and spin-flip relaxation time. Therefore, the general solution of $\vec{\mu}_s$ is given by:

$$\begin{pmatrix} \mu_{sx}(z) \\ \mu_{sy}(z) \\ \mu_{sz}(z) \end{pmatrix} = \begin{pmatrix} A_x \\ A_y \\ A_z \end{pmatrix} \exp(-z/\lambda_N) + \begin{pmatrix} B_x \\ B_y \\ B_z \end{pmatrix} \exp(z/\lambda_N) \tag{2.49}$$

In the case of FM/HM bilayers, the boundary conditions for j_s^z in the HM can be assumed as follows:

$$\vec{j}_s^z(z=0)=0 \tag{2.50}$$

$$\vec{j}_s^z(z=d_N)=\vec{j}_s^z|_{FM/HM} \tag{2.51}$$

$$e\vec{j}_s^z|_{FM/HM}=G_r\vec{m}\times(\vec{m}\times\vec{\mu}_s)+G_i(\vec{m}\times\vec{\mu}_s) \tag{2.52}$$

where $G_{MIX} = G_r+iG_i$ is the complex spin-mixing interface conductance per unit area of the FM/HM interface, d_N is the thickness of HM, $\vec{j}_s^z|_{FM/HM}=(j_{sx}^z(d_N), j_{sy}^z(d_N), j_{sz}^z(d_N))^T$ is the spin current density at the FM/HM interface. Eq. (2.50) is readily understood as the spin current vanishes at the sample surface. Eq. (2.51) states that the spin current is continuous across the FM/HM interface. Eq. (2.52) is based on the consideration that the spin accumulation inside FM of the FM/HM interface is governed by spin mixing conductance. The real part G_r represents the spin transmission efficiency at the interface (transverse component of spin current with $\vec{\sigma}\perp\vec{M}$), while the imaginary part G_i can be interpreted as an effective exchange field acting on the spin accumulation. Substitute Eq. (2.50) and Eq. (2.51) of into Eq. (2.49), the coefficient vectors $\vec{A}$ and $\vec{B}$ can be expressed in terms of j_{sx}^z, j_{sy}^z, j_{sz}^z:

$$A_x=B_x=-\frac{e\lambda_N j_{sx}^z(d_N)}{\sigma\sinh(d_N/\lambda_N)} \tag{2.53}$$

$$\begin{aligned}A_y&=-\frac{e\lambda_N\{j_{sy}^z(d_N)-\theta_{SH}j_c[1-\exp(d_N/\lambda_N)]\}}{\sigma\sinh(d_N/\lambda_N)},\\ B_y&=-\frac{e\lambda_N\{j_{sy}^z(d_N)-\theta_{SH}j_c[1-\exp(-d_N/\lambda_N)]\}}{\sigma\sinh(d_N/\lambda_N)}\end{aligned} \tag{2.54}$$

$$A_z=B_z=-\frac{e\lambda_N j_{sz}^z(d_N)}{\sigma\sinh(d_N/\lambda_N)} \tag{2.55}$$

Further substitution of the above expressions of $\vec{A}$ and $\vec{B}$ into Eq. (2.52) using

Eq. (2.49), the spin accumulation inside HM can be derived as:

$$\frac{\vec{\mu}_s(z)}{\mu_s^0} = -\vec{y}\frac{\sinh\frac{2z-d_N}{2\lambda_N}}{\sinh\frac{d_N}{2\lambda_N}} + [\vec{m}\times(\vec{m}\times\vec{y})\mathrm{Re} + (\vec{m}\times\vec{y})\mathrm{Im}]\frac{2\lambda_N G_{MIX}}{\sigma + 2\lambda_N G_{MIX}\coth\frac{d_N}{\lambda_N}}\frac{\cosh\frac{z-d_N}{\lambda_N}}{\sinh\frac{d_N}{\lambda_N}} \tag{2.56}$$

with $\mu_s^0 = \vec{\mu}_s(0) = (2e\lambda_N/\sigma)j_{s0}^{SH}\tanh(d_N/2\lambda_N)$ the spin accumulation at the interface in the absence of spin transfer ($G_{MIX}=0$), and $j_{s0}^{SH} = \theta_{SH}j_c^0$ the spin current generated in HM before diffusion. The spin current distribution in HM is thus:

$$\frac{\vec{j}_s^z(z)}{j_{s0}^{SH}} = -\vec{y}\frac{\cosh\frac{2z-d_N}{2\lambda_N} - \cosh\frac{d_N}{2\lambda_N}}{\cosh\frac{d_N}{2\lambda_N}} - [\vec{m}\times(\vec{m}\times\vec{y})\mathrm{Re} + (\vec{m}\times\vec{y})\mathrm{Im}]\frac{2\lambda_N G_{MIX}\tanh\frac{d_N}{2\lambda_N}}{\sigma + 2\lambda_N G_{MIX}\coth\frac{d_N}{\lambda_N}}\frac{\sinh\frac{z-d_N}{\lambda_N}}{\sinh\frac{d_N}{\lambda_N}} \tag{2.57}$$

When considering SMR, the spin current is further converted into an opposite charge current via ISHE. The total longitudinal charge current in HM thus becomes:

$$\frac{\vec{j}_{xx}(z)}{j_c^0} = 1 + \theta_{SH}^2[\frac{\cosh\frac{2z-d_N}{2\lambda_N}}{\cosh\frac{d_N}{2\lambda_N}} + \left(1-m_y^2\right)\times\mathrm{Re}\frac{2\lambda_N G_{MIX}\tanh\frac{d_N}{2\lambda_N}}{\sigma + 2\lambda_N G_{MIX}\coth\frac{d_N}{\lambda_N}}\frac{\sinh\frac{z-d_N}{\lambda_N}}{\sinh\frac{d_N}{\lambda_N}}] \tag{2.58}$$

Averaging this charge current over the entire film thickness lead to the SMR ratio expressed as:[50]

$$\frac{\Delta R}{R_{xx}} = \theta_{SH}^2 \frac{\lambda_N}{d_N} \mathrm{Re} \frac{2\lambda_N G_{MIX} \tanh^2 \frac{d_N}{2\lambda_N}}{\sigma + 2\lambda_N G_{MIX} \coth \frac{d_N}{\lambda_N}} \tag{2.59}$$

As can be seen from Eq. (2.56), SMR is mainly related to spin transport parameters of HM such as its spin Hall angle, spin diffusion length, and spin mixing conductance at the FM/HM interface. This is applicable for the case of an insulating FM system, where the conduction electrons cannot travel into FM. When the FM is metallic, Eq. (2.59) must be modified by taking into account the charge current shunting as well as the longitudinal spin current ($\vec{\sigma} \parallel \vec{M}$) absorption by the metallic FM. In this case, the boundary condition Eq. (2.52) should be modified as[71]

$$e\vec{j}_s^{\,z}|_{FM/HM} = e(j_\uparrow - j_\downarrow)\vec{m} - G_r \vec{m} \times (\vec{m} \times \vec{\mu}_s) - G_i (\vec{m} \times \vec{\mu}_s) \tag{2.60}$$

In a similar manner, the SMR ratio can be derived and is given by[62]

$$\begin{aligned}\frac{\Delta R}{R_{xx}} = {\theta_{SH}}^2 \frac{\lambda_N}{d_N} \frac{\tanh^2(d_N / 2\lambda_N)}{1+\xi} [&\frac{g_r}{1+g_r \coth(d_N / 2\lambda_N)} \\ &- \frac{g_F}{1+g_F \coth(d_N / 2\lambda_N)}]\end{aligned} \tag{2.61}$$

with $g_r = \rho_N \lambda_N \mathrm{Re}[G_{MIX}]$, and $g_F = \frac{(1-{P_C}^2)\rho_N \lambda_N}{\rho_F \lambda_F \coth(d_F / \lambda_F)}$. Here, ρ_N, ρ_F, λ_N, λ_F, and d_N, d_F are the resistivity, spin diffusion length and thickness of HM and FM, respectively, $P_C = \frac{j_\uparrow - j_\downarrow}{j_\uparrow + j_\downarrow}$ is the current spin polarization of FM, and $\xi = \rho_N d_F / \rho_F d_N$ is the current shunting factor. Now, the SMR is also related to the spin transport parameters in FM such as its current polarization and spin diffusion length. The above results suggest that SMR serves as a sensitive tool to investigate the spin current interaction with the FM layer. In this dissertation, we extend the study to AF materials, and detailed results and discussion will be presented in Chapter 5.

The current-induced effective field scales linearly with the spin current $\vec{j}_s^z|_{FM/HM}$ at the FM/HM interface and is given by:[72]

$$\Delta H_i = -\frac{\hbar}{2ed_F M_s}(\vec{m}\times \vec{j}_s^z|_{FM/HM})_i \tag{2.62}$$

Substituting Eq. (2.57) and Eq. (2.58) into Eq. (2.62), one obtains the antidamping-like and field-like effective field as follows:[72]

$$H_{DL} = -\theta_{SH}\frac{\hbar}{2e}\frac{j_c}{M_s d_F}(1-\frac{1}{\cosh(d_N/\lambda_N)})\times\frac{(1+g_r)g_r+g_i^2}{(1+g_r)^2+g_i^2} \tag{2.63}$$

$$H_{FL} = -\theta_{SH}\frac{\hbar}{2e}\frac{j_c}{M_s d_F}(1-\frac{1}{\cosh(d_N/\lambda_N)})\times\frac{g_i}{(1+g_r)^2+g_i^2} \tag{2.64}$$

with $g_r = \mathrm{Re}[G_{MIX}]\rho\lambda_N\coth(\frac{d_N}{\lambda_N})$ and $g_i = \mathrm{Im}[G_{MIX}]\rho\lambda_N\coth(\frac{d_N}{\lambda_N})$. As can be seen, the antidamping-like torque is mainly related to the absorption of transverse spin current (G_r), whereas the field-like torque is related to the effective exchange field (G_i). Using the same notion for g_r and g_i, Eq. (2.59) can be re-written as:[73]

$$\frac{\Delta R}{R_{xx}} = \theta_{SH}^2\frac{\lambda_N}{d_N}\tanh(d_N/2\lambda_N)(1-\frac{1}{\cosh(d_N/\lambda_N)})\times\frac{g_r(1+g_r)+g_i^2}{(1+g_r)^2+g_i^2} \tag{2.65}$$

As expected, the SOT and SMR correlate closely with each other. This correlation will be discussed in FeMn/Pt bilayers in Chapter 4 and 5, respectively.

2.8 Summary

In this chapter, the physical background of ferromagnetism and antiferromagnetism is first discussed, including the LLG equation and the macro-spin model. In addition, since majority of the results presented in the dissertation is obtained using electrical measurements, magneto-transport related phenomena such as MR, AHE, PHE are also introduced. More importantly, an emphasis is placed on spin current, spin orbit coupling, spin orbit torque and spin Hall magnetoresistance, which are directly related to this work. A detailed treatment of SOT and SMR based on the drift-diffusion model is introduced. These theoretical backgrounds will be useful for developing an understanding of the experimental results to be presented in chapters 4 - 6.

References

[1] I. R. Harris and A. J. Williams, *Materials Science and Engineering*. (Eolss, Oxford, 2009).

[2] J. M. D. Coey, *Magnetism and Magnetic Materials*. (Cambridge University Press, New York, 2010), pp.128.

[3] A. G. Gurevich and G. A. Melkov, *Magnetization oscillations and waves*. (CRC press, Bacon Raton, 1996), p.59.

[4] L. Néel, Science **174**, 985 (1971).

[5] J. M. D. Coey, *Magnetism and Magnetic Materials*. (Cambridge University Press, New York, 2010), pp.195.

[6] W. H. Meiklejohn and C. P. Bean, Phys. Rev. **102**, 1413 (1956).

[7] J. Nogués and I. K. Schuller, J. Magn. Magn. Mater. **192**, 203 (1999).

[8] M. J. Donahue and D. G. Porter, *OOMMF User's Guide, Version 1.2a5*. (http://math.nist.gov/oommf).

[9] M. R. Scheinfein, *LLG Micromagnetics Simulator*. (http://llgmicro.home.mindspring.com/index.htm).

[10] T. Fischbacher, M. Franchin, G. Bordignon, and H. Fangohr, IEEE Trans. Magn. **43**, 2896 (2007).

[11] A. Vansteenkiste, J. Leliaert, M. Dvornik, M. Helsen, F. Garcia-Sanchez, and B. Van Waeyenberge, AIP Adv. **4**, 107133 (2014).

[12] C. Tannous and J. Gieraltowski, Eur. J. Phys. **29**, 475 (2008).

[13] F. D. Czeschka, PhD dissertation, Universität München, 2011.

[14] C. L. Chien, J. Q. Xiao, and J. S. Jiang, J. Appl. Phys. **73**, 5309 (1993).

[15] T. R. McGuire and R. I. Potter, IEEE Trans. Magn. **11**, 1018 (1975).

[16] W. Gil, D. Görlitz, M. Horisberger, and J. Kötzler, Phys. Rev. B **72**, 134401 (2005).

[17] B. Raquet, M. Viret, E. Sondergard, O. Cespedes, and R. Mamy, Phys. Rev. B **66** (2002).

[18] E. H. Hall, Amer. J. Math. **2**, 287 (1879).

[19] R. Karplus and J. M. Luttinger, Physical Review **95**, 1154 (1954).

[20] N. Nagaosa, J. Sinova, S. Onoda, A. H. MacDonald, and N. P. Ong, Rev. Mod. Phys. **82**, 1539 (2010).

[21] J. D. Patterson and B. C. Bailey, *Solid-State Physics: Introduction to the Theory*. (Springer, Berlin, 2007).

[22] H.-A. Engel, E. I. Rashba, and B. Halperin, *Handbook of Magnetism and Advanced Magnetic Materials*. (John Wiley & Sons, 2007).

[23] E. I. Rashba, Sov. Phys. Solid State **1**, 368 (1959).

[24] A. Manchon and S. Zhang, Phys. Rev. B **78**, 212405 (2008).

[25] A. Manchon and S. Zhang, Phys. Rev. B **79**, 094422 (2009).

[26] M. I. D'yakonov and V. I. Perel', Sov. Phys. JETP Lett. **13**, 467 (1971).

[27] J. E. Hirsch, Phys. Rev. Lett. **83**, 1834 (1999).

[28] A. Hoffmann, IEEE Trans. Magn. **49**, 5172 (2013).

[29] J. Sinova, S. O. Valenzuela, J. Wunderlich, C. H. Back, and T. Jungwirth, Rev. Mod. Phys. **87**, 1213 (2015).

[30] D. Xiao, M.-C. Chang, and Q. Niu, Rev. Mod. Phys. **82**, 1959 (2010).

[31] G. Y. Guo, S. Murakami, T. W. Chen, and N. Nagaosa, Phys. Rev.

Lett. **100**, 096401 (2008).

32 T. Tanaka, H. Kontani, M. Naito, T. Naito, D. S. Hirashima, K. Yamada, and J. Inoue, Phys. Rev. B **77**, 165117 (2008).

33 A. Chernyshov, M. Overby, X. Liu, J. K. Furdyna, Y. Lyanda-Geller, and L. P. Rokhinson, Nat. Phys. **5**, 656 (2009).

34 I. M. Miron, G. Gaudin, S. Auffret, B. Rodmacq, A. Schuhl, S. Pizzini, J. Vogel, and P. Gambardella, Nat. Mater. **9**, 230 (2010).

35 L. Liu, C. F. Pai, Y. Li, H. W. Tseng, D. C. Ralph, and R. A. Buhrman, Science **336**, 555 (2012).

36 K. Garello, I. M. Miron, C. O. Avci, F. Freimuth, Y. Mokrousov, S. Blugel, S. Auffret, O. Boulle, G. Gaudin, and P. Gambardella, Nat. Nanotechnol. **8**, 587 (2013).

37 G. Yu, P. Upadhyaya, Y. Fan, J. G. Alzate, W. Jiang, K. L. Wong, S. Takei, S. A. Bender, L.-T. Chang, Y. Jiang, M. Lang, J. Tang, Y. Wang, Y. Tserkovnyak, P. K. Amiri, and K. L. Wang, Nat Nano **9**, 548 (2014).

38 X. Fan, H. Celik, J. Wu, C. Ni, K. J. Lee, V. O. Lorenz, and J. Q. Xiao, Nat. Commun. **5**, 3042 (2014).

39 C. O. Avci, K. Garello, C. Nistor, S. Godey, B. Ballesteros, A. Mugarza, A. Barla, M. Valvidares, E. Pellegrin, A. Ghosh, I. M. Miron, O. Boulle, S. Auffret, G. Gaudin, and P. Gambardella, Phys. Rev. B **89**, 214419 (2014).

40 K. Masashi, S. Kazutoshi, F. Shunsuke, M. Fumihiro, O. Hideo, M. Takahiro, C. Daichi, and O. Teruo, Appl. Phys. Express **6**, 113002 (2013).

41 X. Fan, J. Wu, Y. Chen, M. J. Jerry, H. Zhang, and J. Q. Xiao, Nat. Commun. **4**, 1799 (2013).

42 M. Hayashi, J. Kim, M. Yamanouchi, and H. Ohno, Phys. Rev. B **89**, 144425 (2014).

43 U. H. Pi, K. Won Kim, J. Y. Bae, S. C. Lee, Y. J. Cho, K. S. Kim, and S. Seo, Appl. Phys. Lett. **97**, 162507 (2010).

44 J. Kim, J. Sinha, M. Hayashi, M. Yamanouchi, S. Fukami, T. Suzuki, S. Mitani, and H. Ohno, Nat. Mater. **12**, 240 (2013).

45 T. Nan, S. Emori, C. T. Boone, X. Wang, T. M. Oxholm, J. G. Jones, B. M. Howe, G. J. Brown, and N. X. Sun, Phys. Rev. B **91**, 214416 (2015).

46 M. Akyol, J. G. Alzate, G. Yu, P. Upadhyaya, K. L. Wong, A. Ekicibil, P. Khalili Amiri, and K. L. Wang, Appl. Phys. Lett. **106**, 032406 (2015).

47 S. Y. Huang, X. Fan, D. Qu, Y. P. Chen, W. G. Wang, J. Wu, T. Y. Chen, J. Q. Xiao, and C. L. Chien, Phys. Rev. Lett. **109**, 107204 (2012).

48 H. Nakayama, M. Althammer, Y. T. Chen, K. Uchida, Y. Kajiwara, D. Kikuchi, T. Ohtani, S. Geprags, M. Opel, S. Takahashi, R. Gross, G. E. Bauer, S. T. Goennenwein, and E. Saitoh, Phys. Rev. Lett. **110**, 206601 (2013).

49 M. Weiler, M. Althammer, F. D. Czeschka, H. Huebl, M. S. Wagner, M. Opel, I. M. Imort, G. Reiss, A. Thomas, R. Gross, and S. T. Goennenwein, Phys. Rev. Lett. **108**, 106602 (2012).

50 Y.-T. Chen, S. Takahashi, H. Nakayama, M. Althammer, S. T. B. Goennenwein, E. Saitoh, and G. E. W. Bauer, Phys. Rev. B **87**, 144411

(2013).

51 M. Althammer, S. Meyer, H. Nakayama, M. Schreier, S. Altmannshofer, M. Weiler, H. Huebl, S. Geprägs, M. Opel, R. Gross, D. Meier, C. Klewe, T. Kuschel, J.-M. Schmalhorst, G. Reiss, L. Shen, A. Gupta, Y.-T. Chen, G. E. W. Bauer, E. Saitoh, and S. T. B. Goennenwein, Phys. Rev. B **87**, 224401 (2013).

52 C. Hahn, G. de Loubens, O. Klein, M. Viret, V. V. Naletov, and J. Ben Youssef, Phys. Rev. B **87**, 174417 (2013).

53 N. Vlietstra, J. Shan, V. Castel, B. J. van Wees, and J. Ben Youssef, Phys. Rev. B **87**, 184421 (2013).

54 S. Meyer, M. Althammer, S. Geprägs, M. Opel, R. Gross, and S. T. B. Goennenwein, Appl. Phys. Lett. **104**, 242411 (2014).

55 T. Lin, C. Tang, H. M. Alyahayaei, and J. Shi, Phys. Rev. Lett. **113**, 037203 (2014).

56 S. R. Marmion, M. Ali, M. McLaren, D. A. Williams, and B. J. Hickey, Phys. Rev. B **89**, 220404(R) (2014).

57 Y. Yang, B. Wu, K. Yao, S. Shannigrahi, B. Zong, and Y. Wu, J. Appl. Phys. **115**, 17C509 (2014).

58 J. H. Han, Y. Y. Wang, Q. H. Yang, G. Y. Wang, F. Pan, and C. Song, Phys. Status Solidi RRL **9**, 371 (2015).

59 M. Isasa, A. Bedoya-Pinto, S. Vélez, F. Golmar, F. Sánchez, L. E. Hueso, J. Fontcuberta, and F. Casanova, Appl. Phys. Lett. **105**, 142402 (2014).

60 Z. Ding, B. L. Chen, J. H. Liang, J. Zhu, J. X. Li, and Y. Z. Wu, Phys. Rev. B **90**, 134424 (2014).

61 C. O. Avci, K. Garello, A. Ghosh, M. Gabureac, S. F. Alvarado, and P. Gambardella, Nat. Phys. **11**, 570 (2015).

62 J. Kim, P. Sheng, S. Takahashi, S. Mitani, and M. Hayashi, Phys. Rev. Lett. **116**, 097201 (2016).

63 S. Cho, S. H. Baek, K. D. Lee, Y. Jo, and B. G. Park, Sci. Rep. **5**, 14668 (2015).

64 T. Shang, Q. F. Zhan, L. Ma, H. L. Yang, Z. H. Zuo, Y. L. Xie, H. H. Li, L. P. Liu, B. M. Wang, Y. H. Wu, S. Zhang, and R. W. Li, Sci. Rep. **5**, 17734 (2015).

65 T. Shang, Q. F. Zhan, H. L. Yang, Z. H. Zuo, Y. L. Xie, Y. Zhang, L. P. Liu, B. M. Wang, Y. H. Wu, S. Zhang, and R.-W. Li, Phys. Rev. B **92**, 165114 (2015).

66 Y. M. Lu, J. W. Cai, S. Y. Huang, D. Qu, B. F. Miao, and C. L. Chien, Phys. Rev. B **87**, 220409(R) (2013).

67 J. H. Han, C. Song, F. Li, Y. Y. Wang, G. Y. Wang, Q. H. Yang, and F. Pan, Phys. Rev. B **90**, 144431 (2014).

68 A. Kobs, S. Hesse, W. Kreuzpaintner, G. Winkler, D. Lott, P. Weinberger, A. Schreyer, and H. P. Oepen, Phys. Rev. Lett. **106**, 217207 (2011).

69 S. Velez, V. N. Golovach, A. Bedoya-Pinto, M. Isasa, E. Sagasta, M. Abadia, C. Rogero, L. E. Hueso, F. S. Bergeret, and F. Casanova, Phys. Rev. Lett. **116**, 016603 (2016).

70 T. Valet and A. Fert, Phys. Rev. B **48**, 7099 (1993).

71 Y. T. Chen, S. Takahashi, H. Nakayama, M. Althammer, S. T. Goennenwein, E. Saitoh, and G. E. Bauer, J. Phys.: Condens. Matter

28, 103004 (2016).

72 J. Kim, J. Sinha, S. Mitani, M. Hayashi, S. Takahashi, S. Maekawa, M. Yamanouchi, and H. Ohno, Phys. Rev. B **89**, 174424 (2014).

73 Y. Yang, Y. Xu, X. Zhang, Y. Wang, S. Zhang, R.-W. Li, M. S. Mirshekarloo, K. Yao, and Y. Wu, Phys. Rev. B **93**, 094402 (2016).

Chapter 3 Experimental Methods

This chapter gives a brief overview of the sample fabrication and characterization techniques mainly including sputtering, photolithography, lift-off, and magneto-transport measurements.

3.1 Sample fabrication

3.1.1 Substrate preparation

The samples were prepared on silicon substrates with 300 nm SiO_2. The substrates were cut into a dimension of 8 mm × 8 mm using dicer from the original 4 inch wafer. Subsequently, a thorough substrates cleaning was carried out in a cleanroom environment to remove any contaminations induced during the wafer handling, transport and cutting. The general cleaning procedures are as follows:

(1) Flush the substrates using deionized (DI) water (resistance > 15 MΩ);

(2) Perform 15 mins ultrasonic bath in acetone;

(3) Transfer the substrates from acetone to isopropyl alcohol (IPA);

(4) Perform 15 mins ultrasonic bath in IPA;

(5) Flush the substrates using deionized (DI) water for 30 s.

(6) Blow the substrates with nitrogen air gun.

3.1.2 Device patterning

After the cleaning process, the substrates were subsequently patterned into Hall bar devices for electrical measurements. The dimensions of the Hall bars are: central area: 2.3 mm × 0.2 mm and transverse electrodes: 0.1 mm × 1 mm. A Microtech laserwriter system with a 405 nm laser was employed to directly write the pattern on the substrate. The general lithography procedures using laserwriter are as follows:

1. A bilayer photoresist consisting of PGMI SF2 and negative resist Microposit S1805 was coated onto the substrates;
2. A pre-calibration was performed before actual exposure to optimize the exposure power and stage scanning speed;
3. The substrates were exposed subsequently using the optimized parameters obtained in the last step;
4. After the exposure, the substrates were soaked in developer MF319 for 90 s to develop S1805, and subsequently soaked in developer 101 for 5 mins to create an undercut with SF2.

The purpose of adopting the bilayer photoresist with the undercut is to avoid the side wall effect during the metal deposition and lift-off. The undercut is estimated to be around 300 nm. Metal deposition and lift-off (both will be discussed shortly) are followed by the lithography process. After forming the Hall bar, a second lithography process was performed to pattern the electrodes with a dimension of 0.5 mm × 0.5 mm. The laser writing conditions are similar to that presented above except for a larger exposure power and a faster scanning speed. Similarly, the second lithography is also followed by the electrode deposition and lift-off.

3.1.3 High vacuum sputtering

The film deposition in this work was carried out using a computer controlled magnetron sputtering system from AJA International, Inc. Fig. 3.1 shows a schematic of the system. It consists of two chambers: the loadlock chamber and the main chamber. Both rotary pump (RP) and turbo molecular pump (TMP) are used to evacuate the loadlock and the main chambers. It has a base and process pressure of 3×10^{-8} Torr and 3 mTorr, respectively. The main chamber has six confocal magnetron sputtering guns allowing uniform deposition over 3" wafer and co-sputtering.

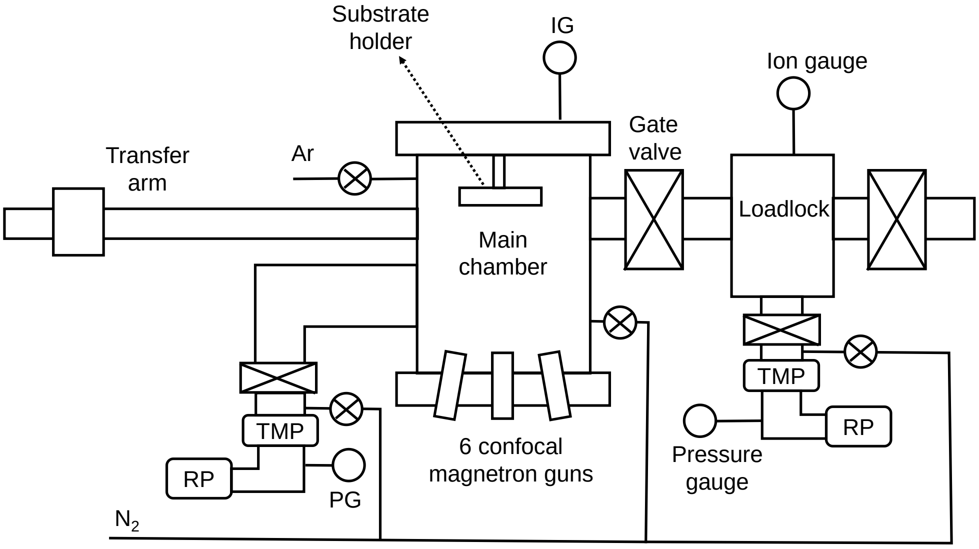

FIG. 3.1 Schematics of the AJA sputtering system.

The deposition power and rate of individual materials are optimized as shown in Table 3.1. All the depositions are performed at room temperature. During the deposition of NiFe and $[\mathrm{FeMn/Pt}]_n$ multilayer, an in-plane field of around 500 Oe was applied to induce the uniaxial anisotropy.

TABLE 3.1 Summary of the deposition power and rate of materials used in this work.

Material	Power (W)	Rate (nm/s)
Ta	200	0.130
Pt	50	0.075
FeMn	70	0.046
NiFe	120	0.055
Au	100	0.167

3.1.4 Lift off and wire bonding

For patterned devices, after each deposition, a lift-off process is performed to remove the photoresist layer. The steps are as follow:

1. Soak the samples in mixed solvent of PG remover and acetone with a volume ratio around 1:3 for 15 mins, and perform an ultrasonic bath of 5 mins;
2. Quickly transfer them to another beaker filled with acetone, and perform another ultrasonic bath of 5 mins;
3. Quickly transfer them to another beaker filled with IPA, and perform another ultrasonic bath of 5 mins;
4. Flush by running DI water for 30 seconds;
5. Check to ensure the quality of patterns with high resolution optical microscope.

For magneto-transport measurement, 200 nm thick Au contact pads with 10 nm Ta adhesion layer were deposited on devices. Except for those measured using probe station, the samples were mounted on 24-pin chip carriers (home-built transport measurement system) or sample pucks (VersaLab PPMS). The Au pads and the bonding pads of chip carriers (or sample pucks) were connected with Au wires by using a Kulicke & Soffa Wire Bonder 4524AD system. Au wires and pads ensure a stable connection during the subsequent measurements.

3.2 Sample characterization

3.2.1 Structural and magnetic properties characterization

The crystallographic texture of the samples was examined using X-ray diffraction (XRD), D8-Advance Bruker system with Cu Kα radiation. Atomic force microscopy (AFM), Veeco Dimension 3100 SPM, was used to characterize both the surface roughness and thickness of deposited films for optimization of the sputtering process. The magnetic properties were characterized using the VSM module of the VersaLab physical property measurement system (PPMS) from Quantum Design, Inc. Before measurement, the coupon films were cut into a size of 4 mm × 5 mm. The resolution of the system is better than 6×10^{-7} emu.

3.2.2 Magneto-transport measurements

As discussed in Chapter 2, various magneto-transport effects can be used to characterize magnetic materials and devices. Such electrical measurements are especially suitable for investigating spin-related phenomenon in AF because of its negligible net moment.[1-3] In this work, the magneto-transport measurements were performed in one of the systems including i) a probe station with electromagnet, ii) a home-built magneto-transport system, and iii) VersaLab PPMS.

Fig. 3.2 illustrates the setup for transport measurements, which generally consists of:

(1) AC – DC current source (Keithley 6221);

(2) Nanovolt meter (Keithley 2182);

(3) Electromagnet (2 kOe for probe station, 4 kOe for home-built system) + power supply (300 V – 5 A);

(4) Superconducting magnet (30 kOe for VersaLab PPMS) + power supply;

(5) Helmholtz coils (used in home-built system) + power supply

(Keithley 2440);

(6) Motorized rotation stage + DC servo controller (used in home-built system), horizontal rotator (used in VersaLab PPMS);

(7) National Instruments LABVIEW programs to coordinate the instrument operation and data acquisition.

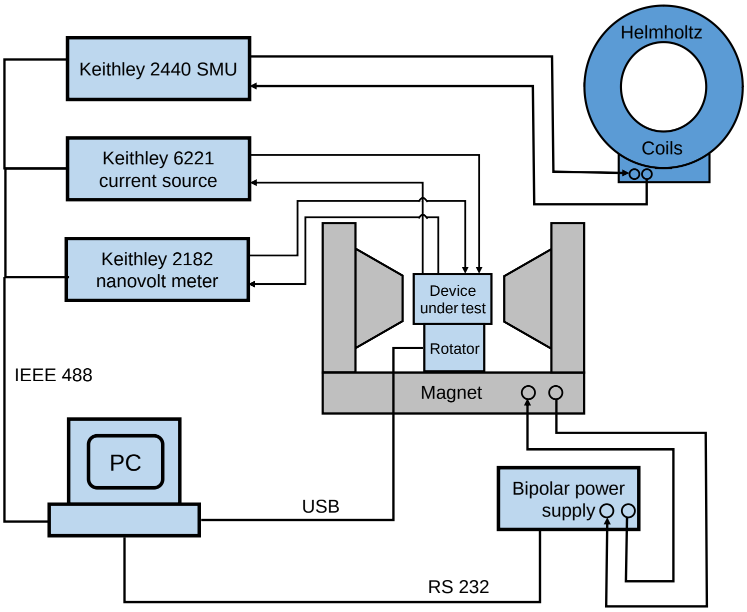

FIG. 3.2 Schematics of the setup for magneto-transport measurements.

3.2.2.1 Measurement of spin Hall magnetoresistance

The investigation SMR consists of two rounds of MR measurements: i) conventional field dependent MR measurements (FDMR) and ii) angle dependent MR measurement (ADMR). As shown in Fig. 3.3(a), in the former case, the longitudinal resistance R_{xx} is recorded with a sweeping magnetic field applied in a fixed direction. In the latter case, R_{xx} is recorded under a constant magnetic field rotating in different coordinate planes (xy, yz, xz) as depicted in Fig. 3.3(b) – (d). If the applied field H is sufficiently large to saturate the magnetization, the SMR ratio can be calculated from the relation $\Delta R/R_{xx} = \left(R_{xx}^{z} - R_{xx}^{y}\right)/R_{xx}^{y}$,[4-6] where R_{xx}^{z} and R_{xx}^{y} are R_{xx} obtained with H

applied in *z*- and *y*-direction, respectively.

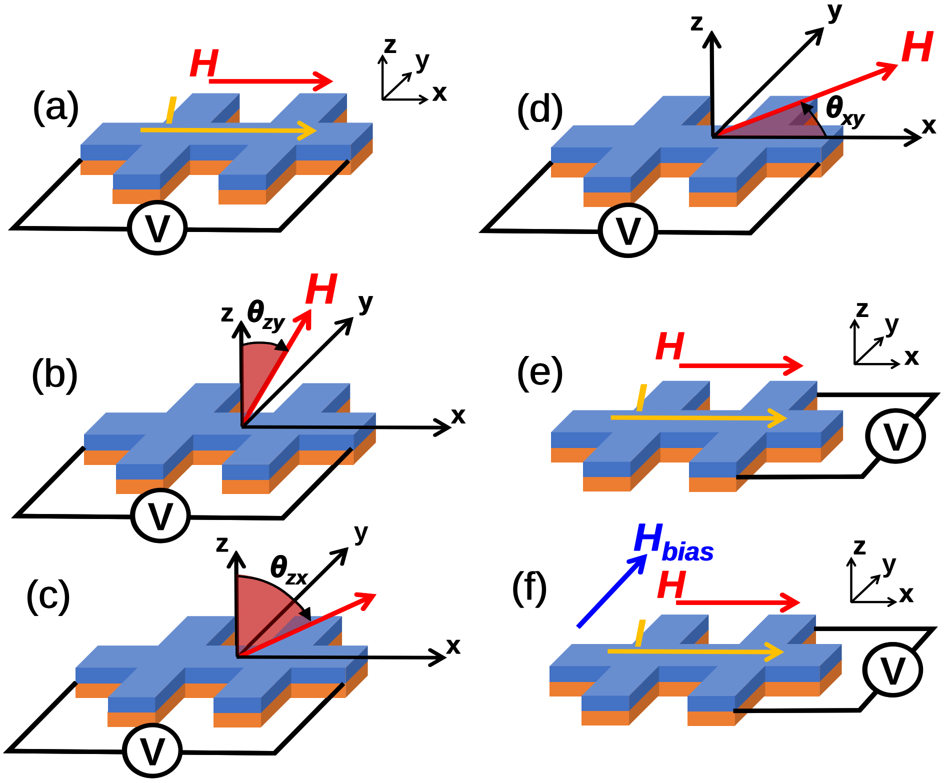

FIG. 3.3 (a) Conventional field dependent MR measurement geometry; (b) – (d) Angle dependent MR measurement geometry with constant magnetic field rotated in *zy*, *zx*, and *xy* plane, respectively; (e) Conventional field sweeping PHE measurement geometry; (f) Second order PHE measurement geometry with transverse bias field.

3.2.2.2 Quantification of spin orbit torque effective field

The SOT effect is investigated following the planar Hall effect measurement geometry, *i.e.*, supplying a DC bias current (I) to the Hall bar samples and measuring the Hall voltage (V_{xy}) while sweeping an external field (H) in x-axis. In the first round of measurements, only the magnitude of I was varied [see schematics in Fig. 3.3(e)].

To quantify the SOT effective field, 2nd order PHE measurements[7,8] were carried out using the external electromagnet with an additional transverse bias magnetic field [see schematic in Fig. 3.3(f)]. In this method, a set of 2nd order PHE voltages, defined as $\Delta V_{xy}(H_{bias}) = V_{xy}(+I, +H_{bias}, H) + V_{xy}(-I, -H_{bias}, H)$, are obtained from the algebraic sum of the first order Hall voltages measured at a positive (+*I*) and negative bias (-*I*) current, respectively, at three different transverse bias fields in *y*-axis direction: $-H_{bias}$, 0 and H_{bias}. Here, V_{xy} is the first order Hall voltage. Under the small perturbation assumption, *i.e.*, both the current induced field (H_{FL}) and applied transverse bias field (H_{bias}) are much smaller than *H*, the change in in-plane magnetization direction is proportional to $(H_I + H_{bias}) / H_{eff}$, where H_I is the sum of H_{FL} and Oersted field (H_{Oe}), and H_{eff} is the sum of *H* and anisotropy field (H_A). The linear dependence of second order PHE voltage on the algebraic sum of H_I and H_{bias} allows one to determine the effective field by varying H_{bias} as both fields play an equivalent role in determining the magnetization direction. After some algebra, it is derived that $\frac{\Delta V_{xy}(0)}{\Delta V_{xy}(H_{bias}) - \Delta V_{xy}(-H_{bias})} = \frac{H_{FL} + H_{Oe}}{2H_{bias}}$. By linearly fitting $\Delta V_{xy}(0)$ against $[\Delta V_{xy}(H_{bias}) - \Delta V_{xy}(-H_{bias})]$, the ratio of $(H_{FL} + H_{Oe})$ to $2H_{bias}$ can be determined from the slope of the curve. After subtracting of H_{Oe} from H_I, the current induced H_{FL} at a specific bias current can thus be obtained.

3.2.2.3 Magnetization switching measurements

Magnetization switching experiments were performed by sweeping a pulsed current and measuring the PHE signal. The measurement geometry is similar to that of the conventional PHE shown in Fig. 3.3(e), except that, instead of magnetic field, a pulsed current is swept to induce SOT switching of the magnetization. We also performed read/write measurement in which the measurement is performed by first rotating the magnetization by a larger current pulse and then reading the magnetization using a smaller current pulse, and repeating the same sequence for as many cycles as one wants.

In both experiments, the purpose of using pulsed current instead of continuous current is to suppress the current induced Joule heating. The pulsed current is supplied by Keithley 6221 with a constant duration of 5 ms and a duty ratio of 2.5%. The voltage reading is done by Keithley 2182 with a delay time of 2 ms after the application of each pulse. The voltage measurement is repeated and averaged for 5 times at each data point.

3.3 Summary

In this chapter, we described briefly the sample fabrication techniques including lithography and sputtering. Details were provided for ADMR and 2nd order PHE measurements, which are used for quantifications of the SOT effective field and SMR ratio for both FeMn/Pt bilayer and multilayer samples.

References

[1] A. B. Shick, S. Khmelevskyi, O. N. Mryasov, J. Wunderlich, and T. Jungwirth, Phys. Rev. B **81**, 212409 (2010).

[2] X. Marti, I. Fina, C. Frontera, J. Liu, P. Wadley, Q. He, R. J. Paull, J. D. Clarkson, J. Kudrnovsky, I. Turek, J. Kunes, D. Yi, J. H. Chu, C. T. Nelson, L. You, E. Arenholz, S. Salahuddin, J. Fontcuberta, T. Jungwirth, and R. Ramesh, Nat. Mater. **13**, 367 (2014).

[3] T. Jungwirth, X. Marti, P. Wadley, and J. Wunderlich, Nat. Nanotechnol. **11**, 231 (2016).

[4] H. Nakayama, M. Althammer, Y. T. Chen, K. Uchida, Y. Kajiwara, D. Kikuchi, T. Ohtani, S. Geprags, M. Opel, S. Takahashi, R. Gross, G. E. Bauer, S. T. Goennenwein, and E. Saitoh, Phys. Rev. Lett. **110**, 206601 (2013).

[5] M. Althammer, S. Meyer, H. Nakayama, M. Schreier, S. Altmannshofer, M. Weiler, H. Huebl, S. Geprägs, M. Opel, R. Gross, D. Meier, C. Klewe, T. Kuschel, J.-M. Schmalhorst, G. Reiss, L. Shen, A. Gupta, Y.-T. Chen, G. E. W. Bauer, E. Saitoh, and S. T. B. Goennenwein, Phys. Rev. B **87**, 224401 (2013).

[6] J. Kim, P. Sheng, S. Takahashi, S. Mitani, and M. Hayashi, Phys. Rev. Lett. **116**, 097201 (2016).

[7] X. Fan, J. Wu, Y. Chen, M. J. Jerry, H. Zhang, and J. Q. Xiao, Nat. Commun. **4**, 1799 (2013).

[8] X. Fan, H. Celik, J. Wu, C. Ni, K. J. Lee, V. O. Lorenz, and J. Q. Xiao, Nat. Commun. **5**, 3042 (2014).

Chapter 4 Field-like Spin Orbit Torque in Ultra-Thin Polycrystalline FeMn Films

As mentioned in Chapters 1 and 2, unlike FM, studies on the interactions between non-equilibrium spins or spin current with AF are quite limited at the time when this work was started. In this chapter, we present the study on the spin current induced SOT effect in FeMn/Pt bilayer and the quantification of the SOT effective field using 2nd order PHE measurements. The SOT effective field results corroborate with the spin Hall origin, and can be explained by taking into account the uncompensated moment in FeMn. The spin diffusion length in FeMn is estimated by quantification of SOT effect in NiFe/FeMn/Pt trilayers.

4.1 Sample structure

Two series of samples in the form of Hall bars were prepared on SiO_2(300 nm)/Si substrates with the following configurations: (i) Si/SiO_2/FeMn(t_{FeMn})/Pt(3) and (ii) Si/SiO_2/Ta (3)/NiFe(3)/FeMn(t_{FeMn})/Pt(3) (number in the parentheses indicates the thickness in nm). The thickness (t_{FeMn}) of FeMn was varied in the range of 0 - 15 nm to investigate its effect on transport properties. The devices were fabricated using combined techniques of sputtering and liftoff as discussed in Chapter 3. Besides the patterned devices for transport measurements, control samples of coupon films were also fabricated to study the structural and magnetic properties. During the deposition of the trilayers, an in-plane bias field of ~500 Oe was applied along the long axis of the Hall bar to induce an in-plane easy axis in NiFe. The resistivity of individual layers was extracted from the overall resistivity of bilayers with thicknesses in the same range of those for transport measurements but with different thickness combinations, and the obtained resistivity values are: ρ_{Ta} = 159 μΩ·cm, ρ_{NiFe} = 79 μΩ·cm, ρ_{FeMn} = 166 μΩ·cm, and ρ_{Pt} = 32 μΩ·cm.

4.2 Investigation of AF order in thin FeMn film

4.2.1 Structural and magnetic properties of FeMn

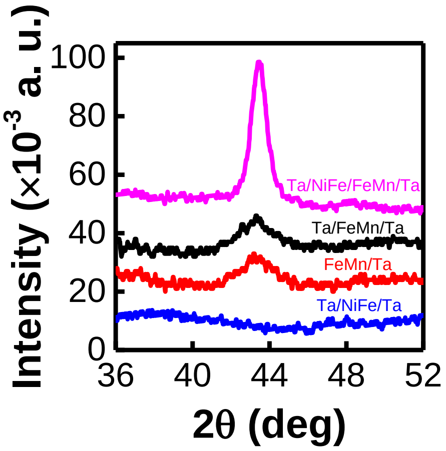

FIG. 4.1 XRD patterns for Ta(3)/NiFe(3)/FeMn(15)/Ta(3), Ta(3)/FeMn(15)/Ta(3), FeMn(15)/Ta(3) and Ta(3)/NiFe(3)/Ta(3) coupon films. Curves are vertically shifted for clarity.

Before proceeding to the electrical measurements, it is desirable to clarify the AF order in the as-deposited FeMn films. To do so, we studied both the structural and magnetic properties of the samples. Fig. 4.1 shows the XRD patterns of coupon films with different structures: (A) Si/SiO_2/Ta(3)/NiFe(3)/FeMn(15)/Ta(3), (B) Si/SiO_2/Ta(3)/FeMn(15)/Ta(3), (C) Si/SiO_2/FeMn (15)/Ta(3), and (D) Si/SiO_2/Ta(3)/NiFe(3)/Ta(3). The Ta capping layer is used to prevent the samples from oxidization. In order to obtain a certain level of signal strength, the thickness of FeMn was intentionally made thicker than those of the samples for electrical transport measurements. As can be seen from the figure, all the samples with a FeMn layer, namely, A, B, and C, exhibit a peak at 43.5°, corresponding to the (111) peak of FeMn. This indicates that the FeMn layer is well textured in [111] direction. The bottom Ta layer enhances the adhesion to the substrate, but it has negligible effect on the texture of FeMn as shown by the subtle difference between the peak intensities of XRD pattern B and C. Therefore, for electrical measurements, the Ta seed layer can be removed in order to avoid the formation of dead layer at the Ta/FeMn interface and also to eliminate any current induced effect from Ta. On the other hand, the insertion of a thin NiFe underlayer significantly enhances the [111] texture of FeMn, as can be seen from the significantly larger peak intensity of A as compared to B and D.

Next, magnetic measurements using VSM were performed on two series of coupon films: (i) a single layer of FeMn(3) covered by different capping layers: Pt(3), Ta(3), and Au(3); and (ii) a single layer of FeMn(t_{FeMn}) with t_{FeMn} = 1 - 15 nm capped by a Pt(3) layer. Fig. 4.2(a) shows the magnetization versus field (*M-H*) loops for the series i) of samples after subtracting the diamagnetic signal from the substrate. All the samples exhibit FM-like *M-H* curves with a negligible hysteresis but a large saturation field around 20 kOe. The samples capped with Pt and Au show similar *M-H* loops and saturation magnetization, whereas the sample capped by Ta exhibit an apparently different behavior: both the saturation field and magnetization are much smaller than those of the other two samples. As shown in the inset of Fig. 4.2(a), the saturation magnetization M_s (averaged over the field range from 20 kOe to 30 kOe) of Pt capped sample is slightly higher than that of the Au capped sample, and both are almost double of that of the Ta capped sample.

This is consistent with earlier reports that (i) Pt interfacial layer can be easily magnetized through proximity effect when contacting with a FM,[1,2] but the same type of effect is weak in Au,[3] and (ii) Ta can create magnetic dead layer in the adjacent FM.[4] Similar proximity effect has been observed at FeMn/Pt interfaces in previous studies on exchange bias.[5,6] Obviously the proximity effect induced moment in Pt alone is unable to account for the large saturation moment shown in Fig. 4.2(a).

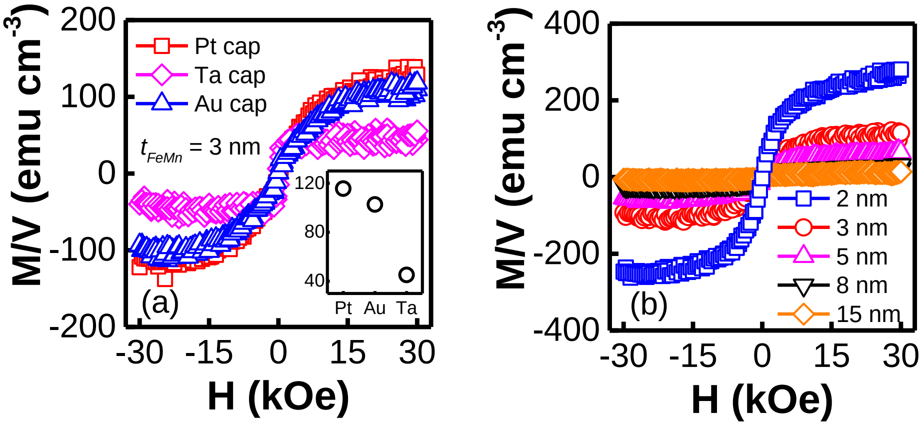

FIG. 4.2 (a) *M-H* loops for FeMn(3)/Pt(3), FeMn(3)/Ta(3), FeMn(3)/Au(3), respectively; (b) *M-H* loops for FeMn(t_{FeMn})/Pt with t_{FeMn} = 2 nm, 3 nm, 5 nm, 8 nm, and 15 nm. Inset of (a): M_s of bilayers with different capping layer.

In order to better understand the origin of the observed net moment, we investigated the series ii) of samples with varying FeMn thicknesses but a fixed Pt capping layer. Fig. 4.2(b) shows the typical examples of *M-H* loops of FeMn(t_{FeMn})/Pt(3) with t_{FeMn} = 2 nm, 3 nm, 5 nm, 8 nm, and 15 nm, respectively. Although the shape of the *M-H* loops looks quite similar among these samples, the saturation magnetization decreases quickly with increasing t_{FeMn}. The saturation magnetization of samples with t_{FeMn} = 1 - 15 nm is further summarized in Fig. 4.3(a). As can be seen, it drops to almost zero at t_{FeMn} = 8 nm. This thickness dependence of saturation magnetization suggests that the observed saturation magnetizations at small thicknesses (t_{FeMn} < 8 nm) are mainly due to canting of spin sub-lattices subject to a large external field [see the illustration in Fig. 4.3(b)]. Canting at a moderate field is only possible when FeMn is thin due to the reduced sub-lattice exchange field at small thickness. With the increase of thickness, a bulk-like AF order will eventually be full established. When this happens it would be difficult to cause any canting of the spin sub-lattices at a moderate field, leading to a vanishing saturation magnetization in the FeMn/Pt bilayer as observed for $t_{FeMn} > 8$ nm.

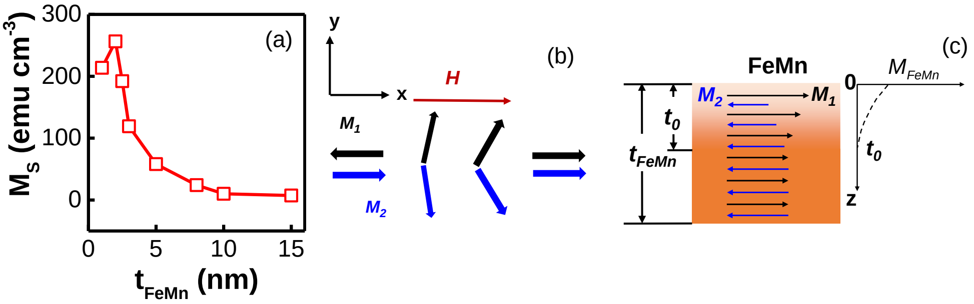

FIG. 4.3 (a) FeMn thickness dependence of M_s of FeMn(t_{FeMn})/Pt (3) bialyers; (b) Illustration of the canting of spin sub-lattices at small FeMn thicknesses; (c) Illustration of spin sub-lattices with unequal magnetizations in FeMn near the FeMn/Pt interface.

On the other hand, any residual saturation moment observed in samples with thick FeMn must come from both the proximity induced moment in Pt and the uncompensated spins from the interfacial layer of FeMn. These net moments are expected to decrease quickly from the interface. However, when t_{FeMn} is below t_0 (the critical thickness for establishing a rigid AF order at room temperature), as depicted in Fig. 4.3(c), the interaction between Pt and FeMn will lead to formation of two spin sub-lattices with unequal magnetizations. Although the net uncompensated moment is expected to decrease from the interface, for the sake of simplicity, we will assume that it is uniform throughout the FeMn when it is thin.

4.2.2 Exchange bias study of NiFe/FeMn/Pt trilayers

To further correlate the magnetic property of FeMn with the M-H loops in Figs. 4.2 and 4.3, magnetoresistance (MR) measurements [see Fig. 4.4(a)] were performed on NiFe(3)/FeMn(t_{FeMn})/Pt trilayer Hall bars with t_{FeMn} varying from 0 to 15 nm. Figs. 4.4(b) and (c) show the MR curves for samples with t_{FeMn} in the range of 0 – 5 nm and 8 – 15 nm, respectively. Since the MR from NiFe is significantly larger than that of FeMn, we can safely assume that the MR is dominated by the signal from NiFe for all the samples, regardless of the FeMn thickness. Shown in Fig. 4.4(d) are the coercivity of NiFe (H_c) and exchange bias field (H_{eb}) at the NiFe/FeMn interface extracted from the MR curves in Figs. 4.4(b) and (c). As can be seen from the results, the effect of FeMn on NiFe depends strongly on its thickness. For $t_{FeMn} < 2$ nm, there is neither H_c enhancement of NiFe nor observable H_{eb} at the NiFe/FeMn interface. This indicates that in this thickness region the blocking temperature (T_B) and possibly Neel temperature (T_N) of the magnetic grains are below room temperature (RT). In other words, the spin sub-lattices within each grain are weakly coupled and the entire film behaves more or less like a superpara-antiferromagnet. At t_{FeMn} of 3 - 5 nm, an increased H_c (around 8 – 270 Oe) and a small H_{eb} (around 1 – 3 Oe) were observed, suggesting the formation of AF order ($T_N > T_B >$ RT) as the thicknesses increases. In this case, the exchange coupling between the spin sub-lattices should have already been established in most of the grains, though its strength as well as the anisotropy remains small and varies among the different grains. Therefore, in this thickness region, the FeMn layer may be treated as an AF with a finite distribution of exchange coupling strength and anisotropy, with both having a small magnitude. As a consequence, the AF sub-lattices can be canted by an external magnetic field with a moderate strength, as shown in Figs. 4.3(b) and (c). The onset of a clear exchange bias, with the H_{eb} (~450 Oe) comparable to typical values reported in literature,[7] was observed for samples with $t_{FeMn} > 8$ nm. In this thickness range, the variation in exchange coupling among the grains may be ignored, and the entire film can be treated as an AF with a uniform exchange coupling strength, but having a finite distribution of anisotropy. As reproduced in the inset of Fig. 4.4(d), the observed thickness dependence of the AF order in our FeMn film is consistent with the previous theoretical calculation[8] of the thickness dependence of T_B.

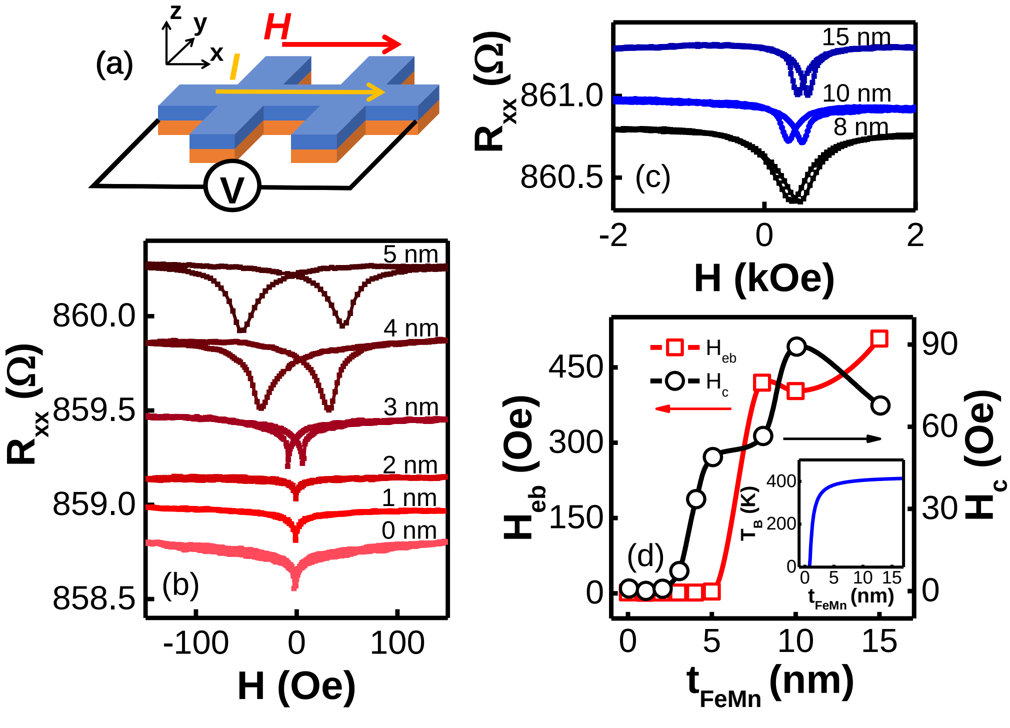

FIG. 4.4 (a) Schematics of field sweeping MR measurement; (b) MR curves for NiFe(3)/FeMn(t_{FeMn})/Pt trilayers with $t_{FeMn} = 0 - 5$ nm; (c) MR curves for NiFe(3)/FeMn(t_{FeMn})/Pt trilayers with $t = 8 - 15$ nm; (d) Dependence of H_c and H_{eb} on t_{FeMn} extracted from (b) and (c). Inset of (d): t_{FeMn}-dependence of T_B (reproduced from Ref. [8]).

It should be noted that the critical thickness for onset of clear exchange bias coincides with the thickness above which the saturation magnetization drops to a minimum in Figs. 4.3(a). This further affirms our explanation that the large saturation moments observed in thin FeMn are due to canting of the spin sub-lattices [see Fig. 4.3(b)]. As will be presented shortly, the current-induced PHE signal also vanishes as the thickness of FeMn exceeds the critical thickness in both bilayer and trilayer samples. Therefore, we focus the discussion hereafter mainly on ultra-thin FeMn films (1 – 5 nm). Although the FeMn layers in this thickness range are not normal AF in the strict sense, the improved response of AF spins to external field provides a convenient way to study the interaction of AF with spin current.

4.3 Magneto-transport results of FeMn/Pt bilayers

4.3.1 PHE measurements of FeMn/Pt bilayers

We now turn to the PHE measurement results of FeMn(t_{FeMn})/Pt(3) bilayer samples. The measurement geometry is shown in Fig. 4.5(a). As an example for the typical results obtained in bilayers, Fig. 4.5(b) shows the planar Hall resistance (ΔR_{xy}) versus field (H) curves obtained at different bias currents (I), for the t_{FeMn} = 3 nm sample. Here, the Hall resistance is given by $\Delta R_{xy} = [V_{xy}(+I,H) + V_{xy}(-I,H)]/2I$, which represents the change in Hall resistance caused by the current-induced effective field. As can be seen from Fig. 4.5(b), the overall shape of the PHE curves resembles that of a typical FM. The Hall signal is weak at low bias current and increases prominently with increasing the bias current. Moreover, the peak position of PHE shifts to larger field values as the bias current increases. Since the AF consists of grains with randomly distributed in-plane anisotropy axes, the PHE signal can be understood as resulting from two competing fields, *i.e.*, the externally applied field in x-direction and current-induced effective field in y-direction, acting on the spin sub-lattices of FeMn. The increase of PHE signal amplitude and shift of the peak position can be understood as being caused by the increase of H_I when the current increases. The role of H_I is confirmed by the observation that the PHE signal vanishes when the field is swept in *y*-direction, as shown in Fig. 4.5(c) for a bias current of 5 mA.

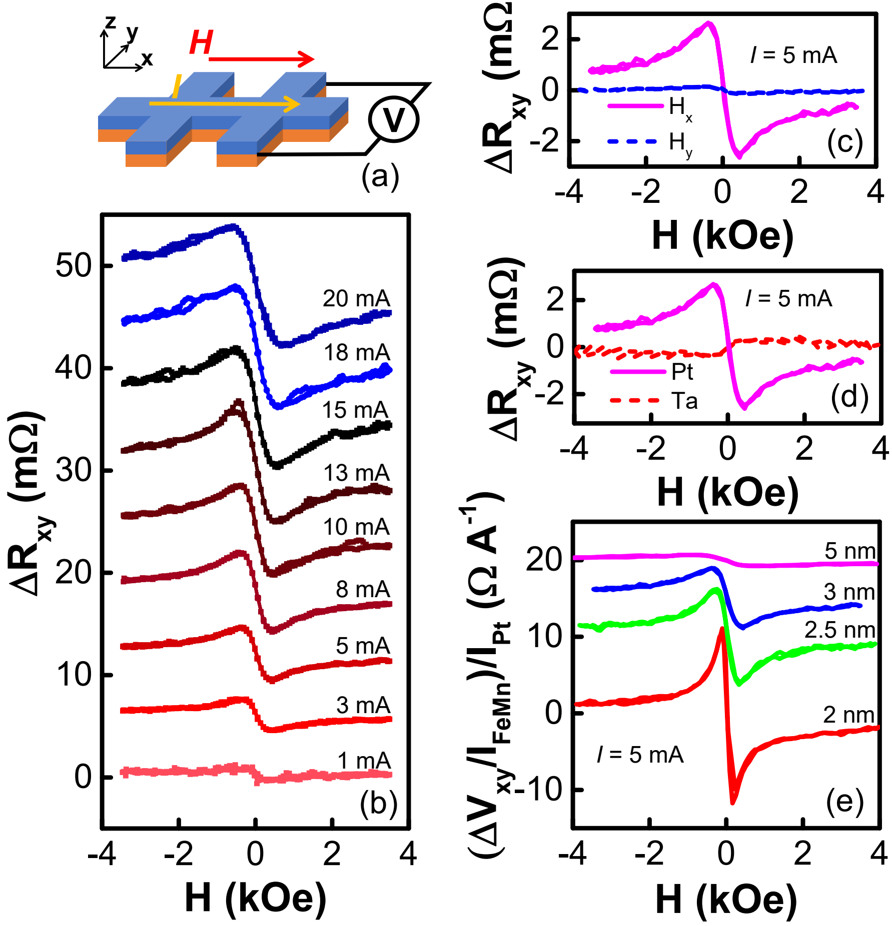

FIG. 4.5 (a) Schematic of PHE measurement at different bias currents; (b) PHE curves for FeMn(3)/Pt(3) at different bias currents; (c) PHE curves for FeMn(3)/Pt(3) obtained at 5 mA with field swept in *x*- and *y*-direction, respectively; (d) A comparison of PHE curves at 5 mA for FeMn(3)/Ta(3) (dashed line) and FeMn(3)/Pt(3) (solid line) with the field applied in *x*-direction; (e) Normalized PHE curves for samples with different FeMn thickness from 2 – 5 nm. Note that curves in (b) and (e) are vertically shifted for clarity.

To further demonstrate that H_I indeed originates from the spin Hall effect, we fabricated a Si/SiO$_2$/FeMn(3)/Ta(3) control sample. Fig. 4.5(d) shows the comparison of the PHE curves at 5 mA for both FeMn(3)/Ta(3) and FeMn(3)/Pt(3) samples. A similar FM-like PHE signal is observed in FeMn/Ta except that the magnitude is much smaller and its polarity is opposite to that of FeMn/Pt. The latter implies that the sign of H_I in FeMn/Ta is opposite to that of FeMn/Pt, which is consistent with the opposite sign of θ_{SH} for Pt and Ta. It can also be inferred from the results that Joule heating is not the major cause for the observation, because otherwise one would expect a PHE with same polarity in both FeMn/Pt and FeMn/Ta as the temperature gradient is not likely to change direction upon changing the top layer as both Pt and Ta have a lower resistivity as compared to FeMn. The bias current dependence of PHE for samples with different FeMn thickness is similar to the one shown in Fig. 4.5(b) except that its magnitude decreases with increasing the FeMn thickness.

Fig. 4.5(e) shows the FeMn thickness dependence of PHE voltage. To have a meaningful comparison, instead of showing the nominal Hall resistance by dividing the Hall voltage by the total current, we show the Hall voltage scaled by the currents in both the FeMn (I_{FeMn}) and Pt (I_{Pt}) layer. This makes sense because the PHE signal mainly comes from the FeMn layer but its amplitude is determined by the current-induced field (H_I) from the Pt layer. I_{FeMn} and I_{Pt} were calculated using three-dimensional (3D) finite element analysis by using the experimentally derived resistivity values for different layers given in Section 4.2. To shorten the simulation time, the Hall bar sample was scaled down to a strip with a length of 2 μm, a width of 0.2 μm and the thicknesses of each layer remained the same as the actual samples. As can be seen from Fig. 4.5(e), the PHE signal decreases with increasing the FeMn thickness, and it becomes vanishingly small at thicknesses above 8 nm (not shown here). This is in good agreement with the results of both the VSM and MR measurements, as discussed above. In other words, the PHE signal observed in FeMn/Pt bilayers are caused by the current-induced canting of spin sub-lattices with unequal magnetizations. The signal gradually decreases to zero as the AF hardens with increasing the thickness.

4.3.2 Quantification of SOT effective field in FeMn/Pt bilayers

In order to quantify the strength of H_I, we carried out the 2nd PHE measurements as described in Chapter 3. Figs. 4.6(a) – (d) show an example of one set of PHE curves with H_{bias} = 0 Oe, +10 Oe and – 10 Oe, respectively, at a bias current of 5 mA for FeMn(t_{FeMn})/Pt(3) samples with t_{FeMn} = 2 nm, 2.5 nm, 3 nm, and 5 nm, respectively. As can be seen, the magnitude of ΔV_{xy} changes with the total field in y-direction including both H_I and H_{bias}. The increase of ΔV_{xy} at H_{bias} = +10 Oe indicates that H_I is in positive y-direction. Figs. 4.6(e) – (h) show the linear fitting of $\Delta V_{xy}(0)$ against ΔV_{bias} = [ΔV_{xy}(+10 Oe) - ΔV_{xy}(-10 Oe)] using the data in Figs. 4.6(a) – (d), respectively. For a better linear approximation, the data at low fields were excluded and only the data at fields above ±1 kOe were used for the fitting.[9] H_I can be calculated from the slope k by using the relation $H_I = 2kH_{bias}$. The offset between the fitting lines at positive and negative region is understood to be caused by either H_{DL} or the thermal effect.[9,10] The small amplitude of the offset confirms again that the contributions from both effects are small in the PHE signals obtained from the FeMn/Pt bilayers.

The same experiments have been repeated for FeMn/Pt bilayers with different bias current in the range of 3 – 20 mA, and the results are summarized in Fig. 4.7(a). As can be seen, the H_I in all samples scales almost linearly with the bias current. After subtracting the Oersted field (H_{Oe}), the

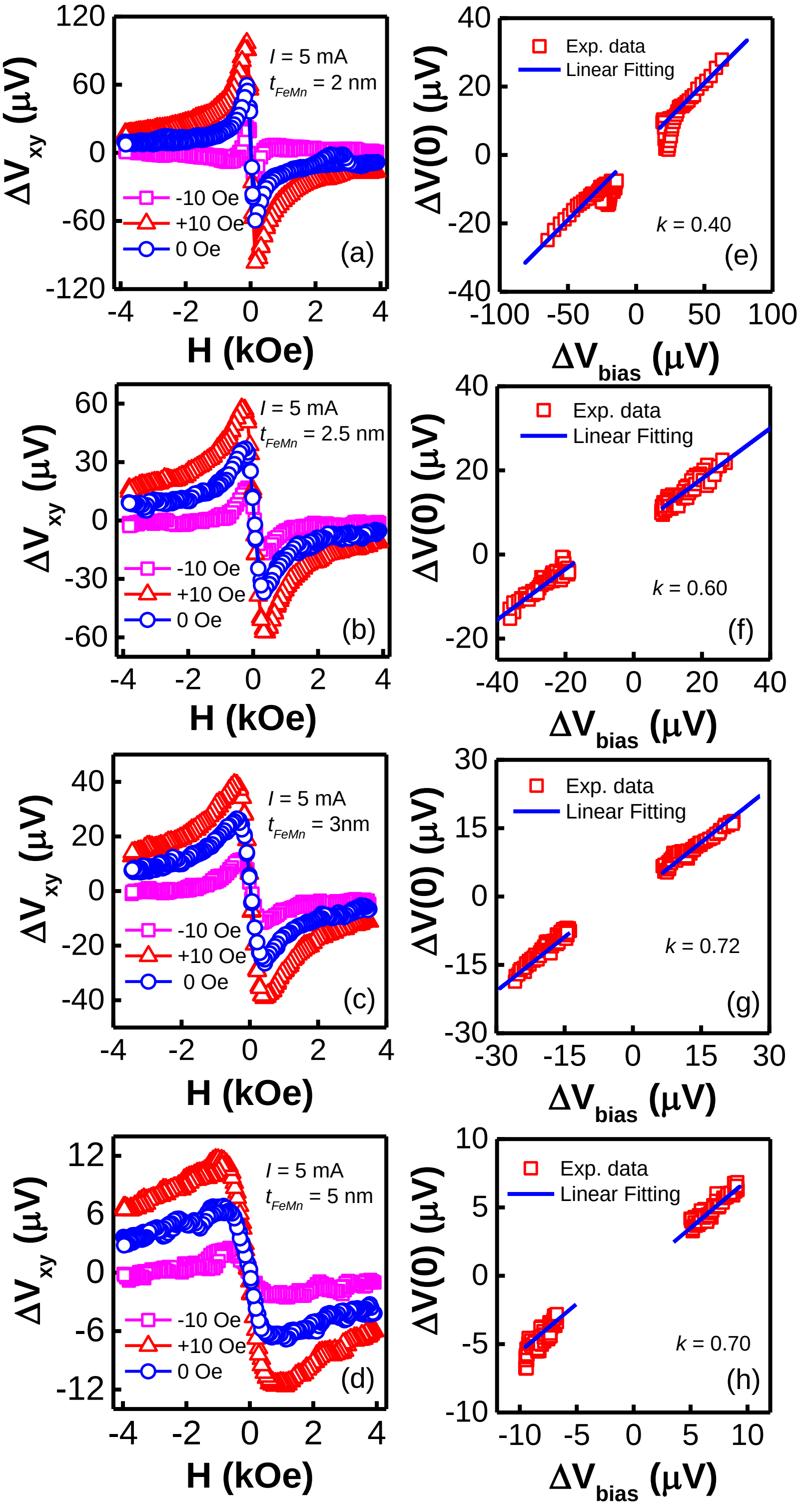

FIG. 4.6 (a) – (d) PHE curves for the FeMn(t_{FeMn})/Pt(3) bilayer measured at 5 mA with different transverse bias field (0 Oe, +10 Oe and -10 Oe) with (a) t_{FeMn} = 2 nm, (b) t_{FeMn} = 2.5 nm, (c) t_{FeMn} = 3 nm and (d) t_{FeMn} = 5 nm; (e) – (f) Linear fitting of ΔV_{xy} (0) against ΔV_{bias} = [ΔV_{xy} (H_{bias} = 10 Oe) - ΔV_{xy} (H_{bias} = -10 Oe)] to determine the ratio of the current-induced H_I to 2H_{bias} with (e) t_{FeMn} = 2 nm, (f) t_{FeMn} = 2.5 nm, (g) t_{FeMn} = 3 nm and (h) t_{FeMn} = 5 nm.

effective-field (H_{FL}) normalized to the current density in Pt is shown in Fig. 4.7(b). The Oersted field in the FeMn layer is calculated using 3D finite element analysis on scaled down strips with a dimension of 20 μm × 2 μm. As shown in the inset of Fig. 4.7 (b), the calculated Oersted field (H_{Oe}) (also normalized to the current density in Pt) in the order of 1×10^{-7} Oe (A^{-1} cm^{2}) is almost independent of the FeMn thickness and is much smaller than the measured H_I for all samples. As shown in in Fig. 4.7(b), the H_{FL}/j_{Pt} ratio (open square) is in the range of 2.05×10^{-5} - 2.44×10^{-5} Oe (A^{-1} cm^{2}) for FeMn/Pt bilayers; this is nearly two orders of magnitude larger than that of the NiFe/Pt control sample [4.01×10^{-7} Oe (A^{-1} cm^{2})]. Although the physical origin of the field-like effective field in FM/HM bilayers is still debatable, recent studies suggest that it can be written in the following form by taking into account the spin Hall current from the HM layer only:[11,12]

$$H_{FL}/j_c = \frac{\hbar}{2e}\frac{\theta_{SH}}{M_s t_{FM}}\left(1-\frac{1}{\cosh(d/\lambda_{HM})}\right)\times\frac{g_i}{(1+g_r)^2+g_i^2} \tag{4.1}$$

where $g_r = \mathrm{Re}[G_{MIX}]\rho\lambda_{HM}\coth(d/\lambda_{HM})$, $g_i = \mathrm{Im}[G_{MIX}]\rho\lambda_{HM}\coth(d/\lambda_{HM})$ with G_{MIX} the spin mixing conductance of FM/HM interface, ρ the resistivity of HM, and λ_{HM} the spin diffusion length in HM. The spin Hall origin of the field-like effective field is supported by several experimental studies,[10,13-15] especially when the FM layer is thick, based on the observation that the field directions are opposite to each other in Pt and Ta based FM/HM bilayers with a same FM. Following this scenario, the large effective field obtained in this study can be readily understood by substituting the relevant parameters into Eq. (4.1). These include the moment per unit area in NiFe ($M_s t_{NiFe}$) and FeMn ($M_{FeMn} t_{FeMn}$) and spin mixing conductance (G_{MIX}) at the NiFe/Pt and FeMn/Pt interfaces. If we assume a same G_{MIX} for the two types of interfaces and use the known M_s of NiFe of 800 emu/cm^3, the resultant net magnetization of FeMn, M_{FeMn}, is in the range of 10.5 – 29.3 emu/cm^3 with a thickness of 2 – 5 nm, as shown in Fig. 4.7(c) (open-square). Also shown in Fig. 4.7(c) (open circle) is the average magnetization extracted from the *M-H* curves shown in Fig. 4.3(b) at an applied field of 4 kOe (note: we use the magnetization at 4 kOe instead of the saturation magnetization because the maximum applied field in electrical measurements was 4 kOe). As can be seen from the figure, although the net magnetization from *M-H* loops is around 5 times larger than that calculated from the H_{FL}, both show very similar trend as long as FeMn thickness dependence is concerned. The difference in absolute values is understandable because in electrical measurements the magnetic moment that affects H_{FL} is mainly concentrated at the FeMn/Pt interface, whereas the VSM measurement detects the moment of the entire film. These results suggest that the small net moment is the determining factor that gives the large effective field to current ratio as compared to NiFe.

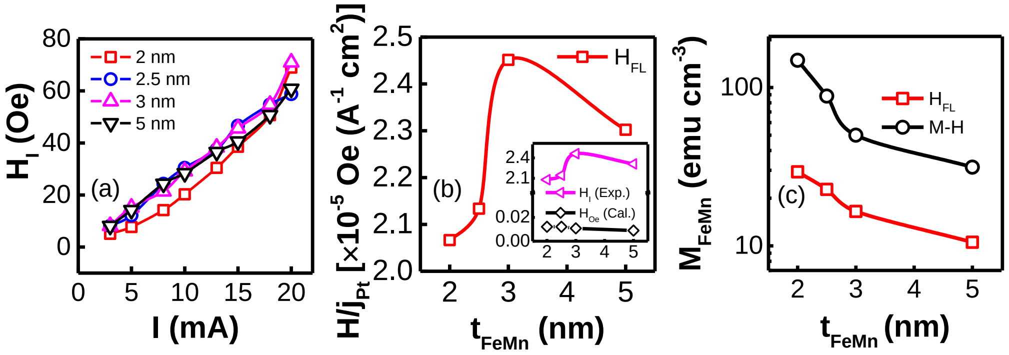

FIG. 4.7 (a) Extracted H_I for FeMn(t_{FeMn})/Pt(3) bilayers with t_{FeMn} = 2 – 5 nm; (b) H_{FL}/j_{Pt} (open square) as a function of t_{FeMn} after subtracting the Oersted field; (c) M_{FeMn} calculated from H_{FL} using Eq. (4.1) (open square) and M_{FeMn} extracted from the *M-H* loops at 4 kOe (open circle). Note that the data in (c) is plotted in log scale for clarity. Inset of (a): a comparison of experimental extracted H_I and calculated H_{Oe} with t_{FeMn} = 2 – 5 nm.

As shown in Fig. 4.7(b), the electrically derived H_{FL}/j_{Pt} ratio (open square) increases sharply with FeMn thickness below 3 nm and then decreases slowly as t_{FeMn} increases further. This is in sharp contrast with the monotonically decreasing dependence of H_{FL} on FM thickness (t_{FM}) in typical FM/HM heterostructures.[10,16] The latter is due to the fact when t_{FM} increases, the product of t_{FM} and M_{FM} increases accordingly, leading to a $1/t_{FM}$ dependence of H_{FL}. However, in the case of FeMn/Pt bilayers, the net magnetization M_{FeMn} decreases with t_{FeMn} (> 2 nm), as confirmed by the VSM measurement results shown in Fig. 4.7(c). This naturally leads to a peak in the curve in Fig. 4.7(b). The peak position of H_{FL} agrees well with the region where H_C is enhanced but clear exchange bias has yet to be established [see Fig. 4.4(d)]. This suggests that the enhancement of H_{FL} occurs in the region that AF order is just about to form and their spin sub-lattices can still be canted easily by either an external or effective field. We noticed that in early theoretical work on spin torque in AF, H_{FL} is treated as negligibly small.[17,18] This is valid for rigid AF systems. It should be pointed out that our results presented in Figs. 4.5 – 4.7 do not contradict these reports because the H_{FL} indeed vanishes when the FeMn thickness is above 8 nm. At such thickness, a rigid AF order is formed and any H_{FL} on the spin sub-lattices should have been cancelled out.

4.3.3 Macro-spin model of the FeMn layer

In order to have a more quantitative understanding of the *M-H* loops in Fig. 4.2(b) and PHE curves in Fig. 4.5(b) for the FeMn/Pt bilayers, we have simulated both curves using the macro-spin model. Although the spin state of bulk FeMn can take either a collinear or non-collinear configuration,[19-22] the spin configuration in an ultrathin film may differ from that of the bulk, especially when it interacts with FM or HM like Pt. In the case of FeMn/FM bilayer, it has been observed experimentally that the spin axis of FeMn is aligned to that of the FM layer from the interface.[23-25] In the case of FeMn/Pt bilayers, the situation can be more complicated due to the strong spin-orbit interaction of Pt. Determination of the exact spin configuration is beyond the scope of this work which certainly deserves further investigations. However, in order to simplify the problem yet without compromising the underlying physics, we treat ultrathin FeMn layer as being consisting of two collinear spin sub-lattices with unequal saturation magnetizations M_s. As we will show in this section, the good agreement between experimental and simulation results supports the collinear model. Under this assumption, the *M-H* loops and PHE curves of FeMn/Pt bilayers shown previously can be simulated through energy minimization. Based on the coordinate notation in Fig. 4.8(a), the free energy density *E* of a specific grain in the FeMn layer can be written as:[26]

$$\begin{aligned} E = J\left|\vec{M}_1\right|\left|\vec{M}_2\right|\cos(\theta_1-\theta_2) - H\left[\left|\vec{M}_1\right|\cos(\varphi-\theta_1)+\left|\vec{M}_2\right|\cos(\varphi-\theta_2)\right] \\ +K_u(\sin^2\theta_1+\sin^2\theta_2) \end{aligned} \tag{4.2}$$

where J is the sub-lattice exchange coupling constant, $\left|\vec{M}_1\right|$ and $\left|\vec{M}_2\right|$ are the magnitude of $\vec{M}_1$ and $\vec{M}_2$, respectively, θ_1 and θ_2 are the angles of $\vec{M}_1$ and $\vec{M}_2$ with respect to *y*-direction, respectively, φ is the angle between *y*-direction and *H*, and K_u is the uniaxial anisotropy constant. Eq. (4.2) can be solved numerically to find the steady-state values for θ_1 and θ_2, which in turn can be used to calculate the *M-H* curve. To facilitate the discussion, we introduce the following parameters: $N = \left|\vec{M}_1\right| / \left|\vec{M}_2\right|$, $H_A = K_u / \left|\vec{M}_2\right|$ and $H_{ex} = J\left|\vec{M}_2\right|$. It should be noted that Eq. (4.2) applies to a single grain with a specific anisotropy axis and exchange coupling strength. Considering the polycrystalline nature of the sample, ideally one should simulate the average *M-H* curve by taking into account the finite distribution of anisotropy axes and exchange field. We first start the simulation with the exchange field fixed and only a uniform distribution of the anisotropy axes is taken into consideration. As shown in the simulated *M-H* loops in Fig. 4.8(b), it is found that the

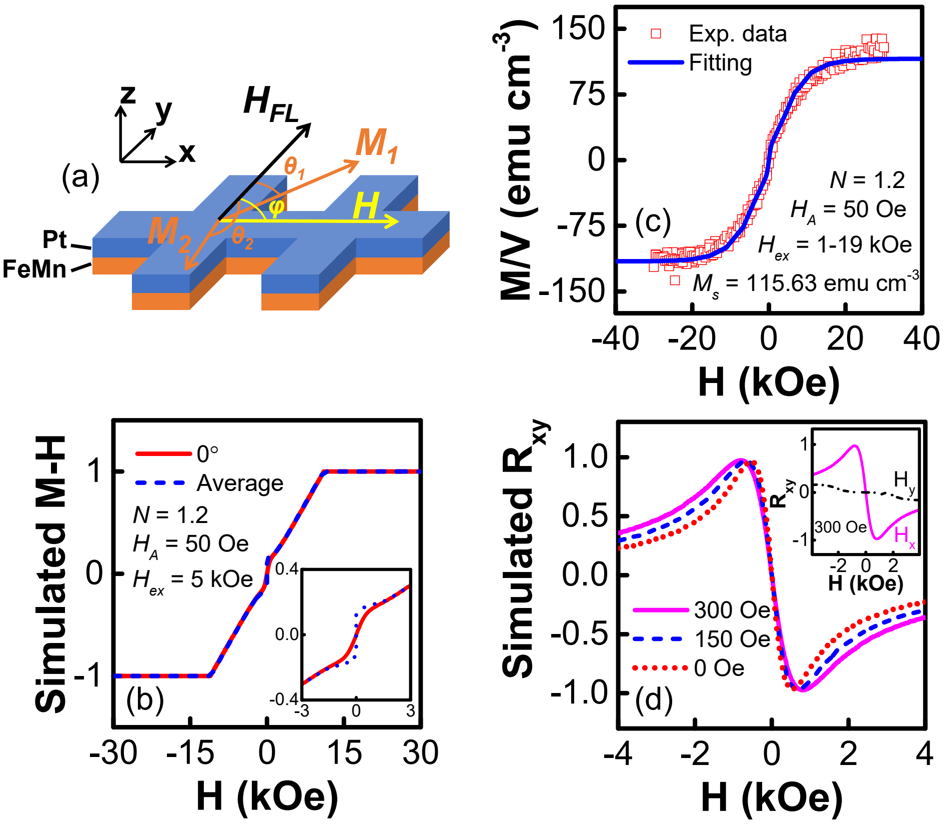

FIG. 4.8 (a) Illustration of the FeMn spin sublattice configuration, external field and current-induced H_{FL}; (b) Simulated *M-H* loop at fixed H_{ex} without anisotropy axes distribution (solid line) and with anisotropy axes distribution (dashed line); (c) *M-H* loop fitting using the macro-spin model for FeMn(3)/Pt(3); (d) Simulated PHE curves with different H_{FL} values (0 Oe, 150 Oe and 300 Oe). Inset of (b): Zoom in of the simulated *M-H* loop at 3 kOe for clarity. Inset of (d): Simulated PHE curves at H_{FL} = 300 Oe with the external field applied in *x* - and *y* - direction, respectively.

calculated curve with a fixed anisotropy axis at 0° (solid line) is very similar to the one that is obtained by assuming that the anisotropy axes is distributed from 0° – 90° at a step of 10° and then taking an average of the calculated curves at different angles (dashed line). Only a small difference exists at low field region [see the zoom-in plot in the inset of Fig. 4.8(b)]. This is due to the fact that K_u in ultra-thin FeMn is small, and its effect on steady-state magnetization direction is overtaken by the current-induced effective field. Therefore, for simplicity, in the subsequent simulations we assumed that the uniaxial anisotropy is along y-axis for all the grains.

To account for the variation of exchange field among different grains, a log-normal distribution was adopted for the exchange field (H_{ex}) distribution: $f(H_{ex}) = \frac{1}{H_{ex}\sigma\sqrt{2\pi}}\exp[-\frac{(\ln H_{ex}-\mu)^2}{2\sigma^2}]$, with μ = log(5000), and σ = 0.5 when H_{ex} is in unit of Oe. This is justifiable assumption based on the following two aspects: i) the grain size of sputtered polycrystalline films typically follows the lognormal distribution[27]; ii) the AF order is found to enhance with the increase of grain size.[28] In this way, the averaged M-H curve was obtained by assuming H_{ex} in the range of 1 – 19 kOe with a discrete step of 2 kOe. As can be seen from Fig. 4.8(c), a reasonably good agreement is obtained between the simulated (solid line) and experimental M-H curves for the t_{FeMn} = 3 nm sample by assuming N = 1.2, H_A = 50 Oe, and M_s = 115.83 emu cm^{-3}. This agreement affirms the above explanation that the net magnetization observed is due to the canting of the spin sub-lattices.

Next, we proceed to account for the spin current in the sample by introducing in Eq. (4.2) an additional Zeeman energy terms arising from H_{FL}, *i.e.* $-H_{FL}(|\vec{M}_1|\cos\theta_1 + |\vec{M}_2|\cos\theta_2)$. Similarly, θ_1 and θ_2 are determined numerically at different H_{FL} values which in turn are used to calculate the normalized PHE signal at different *H*: $PHE = \left(\left|\vec{M}_1\right|\sin 2\theta_1 + \left|\vec{M}_2\right|\sin 2\theta_2\right) / \left(\left|\vec{M}_1\right| + \left|\vec{M}_2\right|\right)$. Fig. 4.8(d) compares the simulated curves at different H_{FL} values with the field in *x*-direction. The simulated curve resembles typical PHE curve for a FM and the peak position increases with increasing H_{FL}, both of which agree well with experimental PHE curves obtained at different bias currents. As shown in the inset of Fig. 4.8(d), when the field is changed to *y*-direction, a vanished PHE is obtained. Therefore, the macro-spin model is able to account for the main experimental observations in FeMn/Pt bilayers. This strongly supports our arguments that the large field-like spin orbit torque in FeMn/Pt bilayers is caused by the relatively small magnetic moment in the FeMn, and resultant SOT is able to induce canting of the spin sub-lattices of the AF.

Before ending this section, we would like to comment on the validity of the macro-spin model. Although the films are polycrystalline, we argue that the macro-spin model is able to capture the essential physics of current-induced SOT in FeMn/Pt bilayers. As shown in the schematic of Fig. 4.9(a), unlike the charge current which flows in the lateral direction (*i.e.*, *x*-direction), the spin current generated from Pt flows mainly in *z*-direction (*i.e.*, in the sample normal direction). Since the FeMn thickness in the samples under investigation (2 – 5 nm) is comparable to the grain size, we can safely assume that the spin current is confined mostly inside a single crystal grain with negligible influence from the grain boundaries (different from the laterally flowing charge current). Therefore, as long as the polycrystalline film has a well-defined texture in the thickness direction which is the case in this study, it would appear locally as a “quasi-single crystal” to the vertically flowing spin-current [see schematic in Fig. 4.9(b)]. Compared to the true single crystal case, the only difference is that in the polycrystalline case, the SOT effect is further averaged over different grains due to the random distribution of crystalline anisotropy and exchange energy, which has been taken into account in the above discussion. Therefore, we believe the macro-spin model is appropriate for interpretation of the experimental results observed in this work.

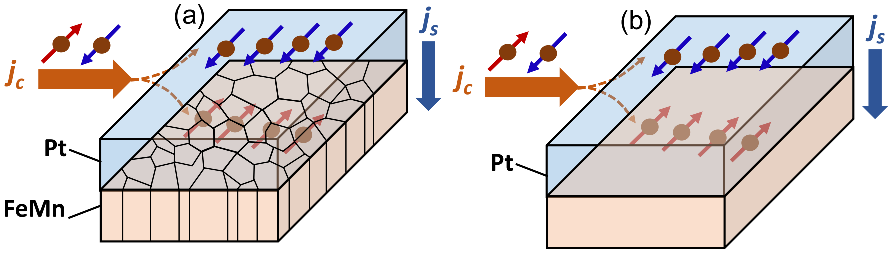

FIG. 4.9 (a) Schematic of charge current flowing in the Pt layer and spin current flowing in the polycrystalline film (real situation); (b) Schematic of charge current flowing in the Pt layer and spin current flowing in the single crystal film (ideal case).

4.4 Magneto-transport results of NiFe/FeMn/Pt trilayers

4.4.1 PHE measurements of NiFe/FeMn/Pt trilayers

To further demonstrate that the spin current generated in Pt is indeed largely absorbed by FeMn, we have fabricated NiFe(3)/FeMn(t_{FeMn})/Pt(3) trilayer Hall bars and studied SOT-induced magnetization rotation in NiFe. Fig. 4.10(a) shows the PHE curves at different bias currents (I) for the NiFe(3)/FeMn(3)/Pt(3) sample. Similar to the results shown in Fig. 4.5(b), the PHE signal increases prominently as I increases, indicating the presence of a current-induced effective field H_I in y-direction. The Hall signal is much larger than that of the FeMn/Pt bilayer in the same field range; therefore the signal from the trilayer is dominantly from the NiFe layer. The results can be qualitatively understood as follows. The spin current generated by the Pt layer travels through the FeMn spacer and induces SOT in the NiFe layer. The SOT will then cause a rotation of the NiFe magnetization, leading to the observed increase of PHE with the bias current. To have a more quantitative understanding of the current dependence of PHE signal, 3D micromagnetic modeling was performed on an NiFe element with and without a transverse field using OOMMF.[29] To shorten the computation time, in the simulation, the sample is scaled down to a strip with a dimension of 23 μm × 2 μm × 3 nm. The parameters used are: saturation magnetization $M_s = 8\times10^5$ A m^{-1}, exchange constant $J = 1.3\times10^{-11}$ J m^{-1}, damping constant $\alpha = 0.5$, anisotropy constant $K_u = 100$ J m^{-3} and unit cell size: 10 nm × 10 nm × 3 nm. A fixed bias

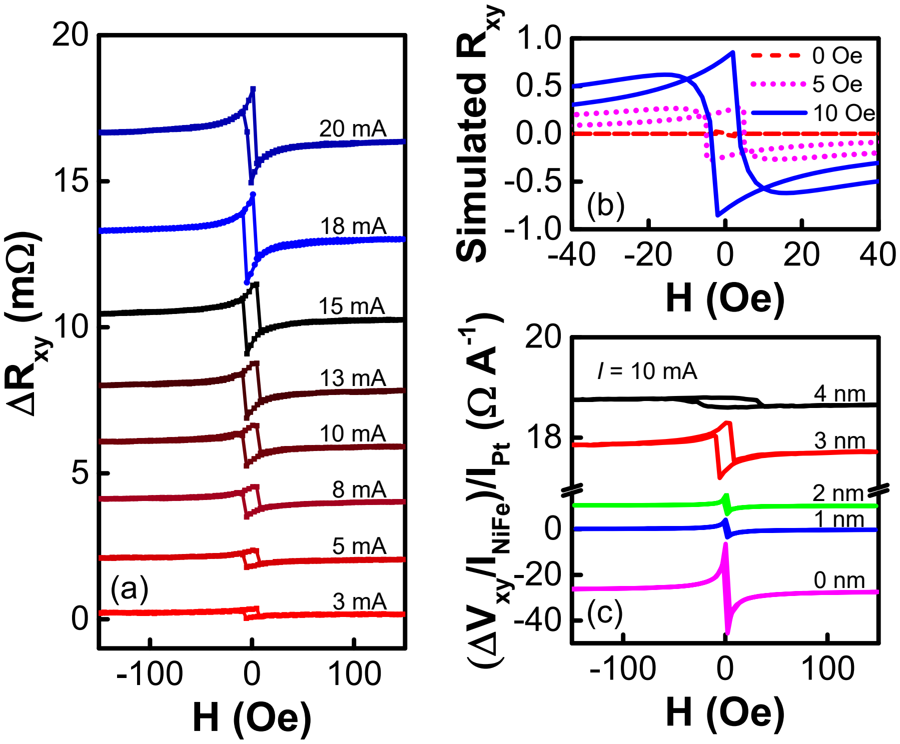

FIG. 4.10 (a) PHE curves at different bias currents for the NiFe(3)/FeMn(3)/Pt(3) trilayer; (b) Simulated PHE curves with 0 Oe, 5 Oe and 10 Oe bias field in *y*-direction; (c) Normalized PHE curves at 10 mA for the trilayer sample with FeMn thicknesses of 0 – 4 nm. Note that the curves in (a) and (c) are vertically shifted for clarity.

field in *y*-direction is used to simulate the effective field induced by the current. To account for the Hall measurement geometry, only the data at the center area of 1 μm × 2 μm representing the Hall bar cross is taken into consideration for the calculation of PHE signal. Fig. 4.10(b) shows the simulated PHE curves at bias fields of 0 Oe, 5 Oe and 10 Oe, respectively. Note that due to the much smaller size used in the simulation, the simulated H_c is much larger than the measured value, and therefore a large transverse bias field of 10 Oe was used in the simulation accordingly. Except for the large H_c, the simulated curves resemble well the measured PHE curves. Fig. 4.10(c) shows the normalized PHE curves for samples with different FeMn thicknesses at a bias current of 10 mA. As can be seen, the signal amplitude decreases as the thickness increases, indicating the decrease of the H_I at larger FeMn thickness. When the FeMn thickness exceeds 5 nm, the signal becomes vanishingly small, suggesting that the spin current cannot travel through the FeMn layer beyond this thickness.

4.4.2 Quantification of SOT effective field in NiFe of the trilayers

To quantity the strength of the field-like effective field in the NiFe layer, again we carried out the second order PHE measurements. Figs. 4.11(a) – (d) show one set of PHE curves for NiFe(3)/FeMn(t_{FeMn})/Pt(3) with t_{FeMn} = 1 nm, 2 nm, 3 nm and 4 nm, obtained at I = 10 mA, and H_{bias} = 0 Oe, +0.6 Oe and – 0.6 Oe, respectively. The flip of curve polarity at positive and negative bias field suggests that H_I is comparable to the applied bias field of 0.6 Oe. Figs. 4.11(e) – (h) show the linear fitting of $\Delta V_{xy}(0)$ against ΔV_{bias} using the data in Figs. 4.10(a) – (d). The slope k turns out to be much smaller than that obtained for the FeMn/Pt bilayers, as shown in Figs. 4.6(e) – (h). This in turn gives a

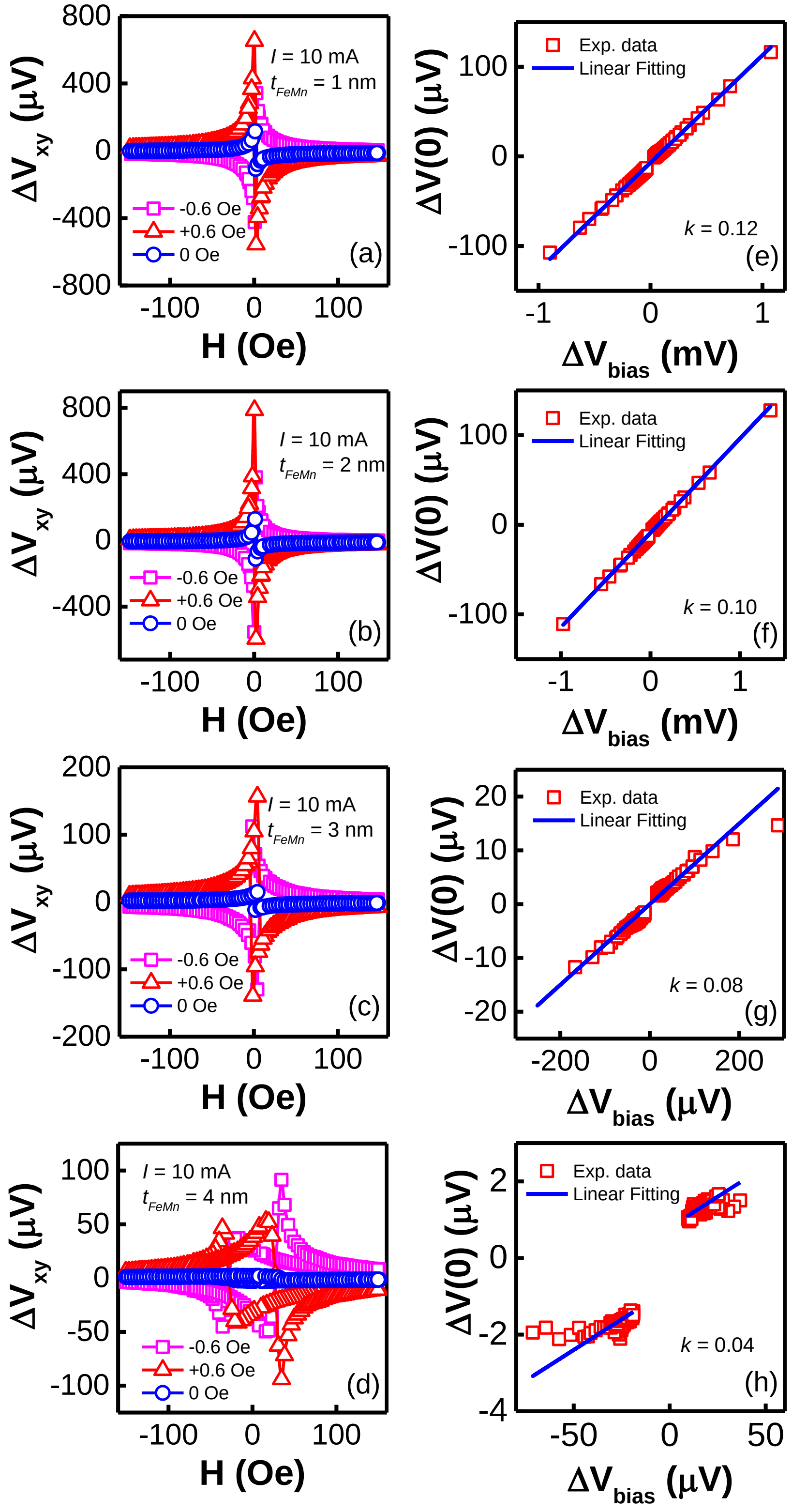

FIG. 4.11 (a) – (d) PHE curves for the NiFe(3)/FeMn(t_{FeMn})/Pt(3) trilayer measured at 10 mA with different transverse bias field (0 Oe, +0.6 Oe and -0.6 Oe) with (a) t_{FeMn} = 1 nm, (b) t_{FeMn} = 2 nm, (c) t_{FeMn} = 3 nm and (d) t_{FeMn} = 4 nm; (e) – (f) Linear fitting of ΔV_{xy} (0) against ΔV_{bias} = [ΔV_{xy} (H_{bias} = 0.6 Oe) - ΔV_{xy} (H_{bias} = -0.6 Oe)] to determine the ratio of the current-induced H_I to $2H_{bias}$ with (e) t_{FeMn} = 1 nm, (f) t_{FeMn} = 2 nm, (g) t_{FeMn} = 3 nm and (h) t_{FeMn} = 4 nm.

much smaller H_I for the trilayer samples with $t_{FeMn} = 0$ - 4 nm, as shown in Fig. 4.12(a). Similar to the case of FeMn/Pt bilayers, H_I for all samples scales almost linearly with the bias current. The $t_{FeMn} = 0$ sample corresponds to a Ta(3)/NiFe(3)/Pt(3) trilayer. The obtained H_I value of 0.52 Oe at a bias current of 10 mA is comparable to reported value for similar structure.[10] The H_I value drops sharply with the insertion of a 1 nm FeMn, and decreases further as the FeMn thickness increases. To quantify the current contribution directly from the Pt layer, we have to subtract from H_I two other contributions, *i.e.*, H_{Oe} in the NiFe layer and H_{FL} from the Ta seed layer. The total Oersted field in NiFe, H_{Oe}, is calculated using 3D finite element analysis, and the results are shown in the inset of Fig. 4.12(b) as a function of FeMn thickness (down triangle); it increases with FeMn thickness due to the increase of current in the FeMn layer. In order to estimate the contribution of current in the Ta layer to H_I, we have fabricated a NiFe(3)/Ta(3) control sample and measured the effective field using the same second order PHE measurement. The effective field to current ratio obtained is $H_{FL}(Ta)/j_{Ta} = 1.49\times10^{-7}$ Oe (A^{-1} cm^2). Based on this value, we can estimate the contribution of Ta current in the trilayers with different FeMn thicknesses. The results are shown in the inset of Fig. 4.12(b) in upper triangles. The value of $H_{FL}(Ta)$ is almost constant due to the much larger resistivity of Ta as compared to other layers. Also shown in the inset is the FeMn thickness dependence of H_I. The net effective field is obtained as $H_{FL} = H_I - H_{Oe} - H_{FL}(Ta)$. As shown in Fig. 4.10(d), all the samples exhibit a non-zero H_{FL} except for the $t_{FeMn} = 4$ nm sample in which H_I and H_{Oe} are comparable. As shown clearly in the inset of Fig. 4.12(b), the contribution of

Ta layer to the effective field is negligible.

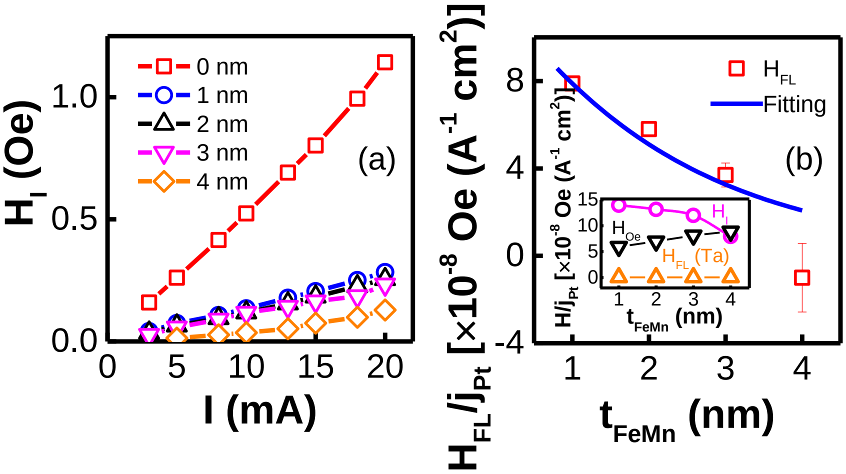

FIG. 4.12 (a) Extracted H_I for samples with t_{FeMn} = 0 nm – 4 nm; (b) Experimental values for H_I (open square) and fitting using Eq. (4.5) (solid line). Inset of (b): FeMn thickness dependence of H_I (circle), H_{Oe} in NiFe (down triangle) and H_{FL} from Ta (upper triangle), respectively. Note that the data in (b) are normalized to the current density in Pt.

After excluding the contribution from Ta as main source, the net H_{FL} must be induced by the spin current from the Pt layer since the spin Hall angle of FeMn is very small.[30,31] Considering the fact that the Pt layer has a same thickness in all the samples, it is plausible to assume that the spin Hall angle and thickness scaling factor $[1-1/\cosh(d/\lambda_{HM})]$ of Pt are the same among the different samples. We further assume that the moment per unit area of NiFe ($M_s t_{NiFe}$) is also a constant. Therefore, the decrease in effective field in the NiFe layer can only come from two sources: (i) relaxation of spin current in FeMn, and (ii) reduced spin mixing conductance (G_{MIX}) at the FeMn/Pt and NiFe/FeMn interfaces as compared to the single NiFe/Pt interface. Earlier reports[30,32] found that spin transport in FM/normal metal (NM)/FeMn structures is mainly dependent on the FM/NM interface and the spin relaxation inside FeMn. Therefore, rather than a dramatic modification of G_{MIX} at the interfaces with the presence of the FeMn layer, the absorption of spin current by FeMn is more likely the major cause for decreased spin current entering NiFe. This spin absorption explanation is also consistent with the large H_{FL} observed in FeMn/Pt bilayers.

4.4.3 Spin transport in NiFe/FeMn/Pt trilayer

The spin current in the NiFe layer induced by Pt in the NiFe/FeMn/Pt trilayer can be modeled using the drift-diffusion model. Due to the relatively large size of the Hall bar sample in the *xy* plane, the spin current can be treated as non-equilibrium spins flowing in *z*-direction with polarization in *y*-direction. Therefore, the spatial distribution of spin current in NiFe/FeMn can be written as:

$$j_i(\mathrm{z}) = -\frac{1}{2e\rho_i}\frac{\partial \Delta\mu_i(\mathrm{z})}{\partial \mathrm{z}} \tag{4.3}$$

where i = 1 refers to FeMn, i = 2 denotes NiFe, $\Delta\mu_i$ and j_i are the net spin accumulation and spin current density in layer i, respectively, and ρ_i is resistivity of layer i. The spin accumulation satisfies the following diffusion equation:[33]

$$\frac{\partial^2 \Delta\mu_i(\mathrm{z})}{\partial \mathrm{z}^2} = \frac{\Delta\mu_i(\mathrm{z})}{\lambda_i^2} \tag{4.4}$$

where λ_i is the spin diffusion length of layer i. The general solution for $\Delta\mu_i$ is $\Delta\mu_i(z) = A_i \exp(z/\lambda_i) + B_i \exp(-z/\lambda_i)$. To obtain specific solutions, we need to set up proper boundary conditions. As discussed above, the effect of Ta layer is negligible. In order to obtain a simple analytical solution, we assume that the spin current is zero at the NiFe/Ta interface. Based on this assumption, we adopted the following boundary conditions: $j_1(0) = j_0$, $j_2(t_2) = 0$, $j_1(t_1) = j_2(t_1)$ and $\Delta\mu_1(t_1) = \Delta\mu_2(t_1)$, where t_1 is the thicknesses of the FeMn

(t_{FeMn}), t_2 is the sum of the thickness of FeMn and NiFe layer ($t_{FeMn}+ t_{NiFe}$), and j_0 is the spin current generated by Pt entering FeMn. Substituting the boundary conditions into Eq. (4.3) and (4.4), the spin current density at the interface entering NiFe can be derived as:

$$j(t_1)/j_0 = \frac{2\lambda_1\rho_1 A(1-B^2)}{\lambda_1\rho_1(1+A^2)(1-B^2)+\lambda_2\rho_2(1-A^2)(1+B^2)} \tag{4.5}$$

where $A=\exp(t_{FeMn}/\lambda_1), B=\exp(t_{NiFe}/\lambda_2)$. Comparing it with Eq. (4.1), we can see that the spin absorption in FeMn layer gives an additional scaling factor for spin current to be delivered to the NiFe layer. In the extreme case when t_{NiFe} approaches infinite, *i.e.*, $B\to\infty$, Eq. (4.5) is reduced to $j(t_1)/j_0 \approx 1/A$, if $\lambda_1\rho_1 \approx \lambda_2\rho_2$, which is the exponential decay formula used in Ref. [32,34,35] to obtain the spin diffusion length in AFs. On the other hand, if $t_1 = 0$, $j(t_1)/j_0 = 1$, which means that the spin-current generated by Pt will enter NiFe directly without absorption in the FeMn layer. In our sample, since the NiFe thickness is comparable to that of FeMn, the effect of NiFe can no longer be ignored. Note that the difference in G_{MIX} of NiFe/Pt and FeMn/Pt interfaces is ignored for simplicity and we also assume that G_{MIX} is independent of FeMn thicknesses. Although G_{MIX} may be thickness dependent (*i.e.* j_0 is dependent on t_{FeMn}), in the above derivation we mainly focus on the spin current decay in FeMn and consider j_0 as a constant. By scaling the H_{FL} obtained in NiFe layer using the resistivity of the films obtained above and the spin diffusion length of NiFe (λ_2 = 3 nm),[36] as shown in Fig. 4.12(b), the spin diffusion length of FeMn (λ_1) is obtained as 2 nm. This value is comparable to earlier reports of 1.9 nm (Ref. [32]) and 1.8 ± 0.5 nm (Ref. [30]). The short spin diffusion length is consistent with the previous understanding of AF as a good “spin sink”.[37,38] The effective absorption of spin current by FeMn is consistent with the large SOT effect observed in FeMn/Pt bilayers. Although the spin configuration of FeMn in the bilayer sample may be different from that of the trilayer sample due to the insertion of the NiFe seed layer in the latter, we foresee that the difference, if any, is only qualitative; it will not affect the results and conclusion drawn in this section in a fundamental way.

The difference in FeMn thickness dependence of H_{FL} between the bilayer case [Fig. 4.7(b)] and trilayer [Fig. 4.12(b)] case can be understood as follows. As we discussed in Section 4.4, the H_{FL} in FeMn/Pt bilayer is mainly determined by the thickness dependence of the magnetic moment in FeMn ($M_{FeMn}t_{FeMn}$) [see Fig. 4.7(c)]. On the other hand, for the NiFe/FeMn/Pt trilayer case, H_{FL} is for the NiFe layer (the signal from FeMn is masked out by that of NiFe due to its much smaller magnetization), and thus it is a measure of spin current that travels across the FeMn layer and eventually enters the NiFe layer. As can be seen from Eq. (4.5), the spin current traveling in FeMn further decays by a factor of $\frac{2\lambda_1\rho_1 A(1-B^2)}{\lambda_1\rho_1(1+A^2)(1-B^2)+\lambda_2\rho_2(1-A^2)(1+B^2)}$ upon reaching the NiFe/FeMn interface. This decay gives the overall decay of spin current upon reaching the NiFe/FeMn interface. This spin current is further converted to H_{FL} in NiFe through the magnetic moment ($M_{NiFe}t_{NiFe}$). Since the NiFe thickness is fixed among the samples, the FeMn thickness dependence of H_{FL} in NiFe of the trilayers should be the same as that of the spin current reaching the NiFe/FeMn interface. This explains why the H_{FL} in NiFe decreases monotonically with the FeMn thickness, which is different from that in FeMn.

4.5 Summary

Clear FM-like PHE signals were observed in FeMn/Pt bilayers with the FeMn thicknesses ranging from 2 - 5 nm. Magnetometry measurements of coupon films suggest that the FM-like behavior originates from canting of spin sub-lattices in the FeMn layer. Using the second order PHE measurement method,[9,10] a field-like effective field to current ratio in the range of 2.05×10^{-5} - 2.44×10^{-5} Oe (A^{-1} cm^2) was extracted, which is nearly two orders of magnitude larger than the typical value of 4.01×10^{-7} Oe (A^{-1} cm^2) for NiFe/Pt bilayers. Fig. 4.13 summarizes the H_{FL} values obtained in this work and other in-plane anisotropy FMs. The significantly large effective field value is understood as a result of much smaller net moments from canting of the uncompensated spins in the AF as compared to its FM counterpart.

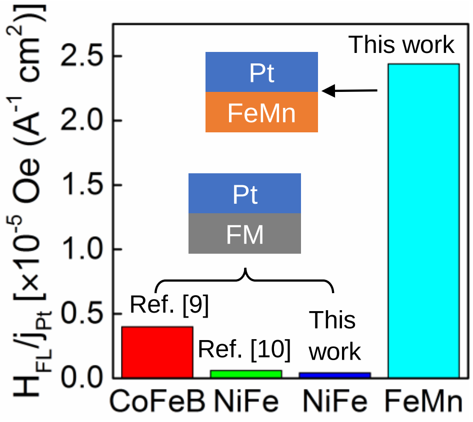

FIG. 4.13 Comparison of the H_{FL} values obtained in FeMn with that obtained in FMs with in-plane anisotropy.

Further investigations on NiFe/FeMn/Pt trilayers using the same PHE measurements confirm that the spin current generated by Pt is largely absorbed by FeMn and it can only travel through FeMn with a thickness of 1 - 4 nm. A spin diffusion length of around 2 nm in FeMn is obtained by quantifying the field-like effective field induced in NiFe, which is comparable to the ST-

FMR[32] and spin pumping[30] measurements. Our results suggest that in ultra-thin polycrystalline AFs, due to the relatively small exchange field between spin sub-lattices, the spin current can interact with AF, causing reorientation of the spin sub-lattices, in a similar way as it does with the FM.

Before we conclude, it is worth pointing out that the FeMn investigated in this work has a polycrystalline structure, and due to the ultra-thin thickness, the AF order may not be well defined as that in the bulk material. We foresee this as the main challenge in investigating and exploiting SOT effect in AF materials, *i.e.*, SOT is more prominent in ultra-thin layers, but most AF requires a finite thickness to develop a stable AF order at room temperature. To overcome this difficulty, it is necessary to development AF materials which allow effective generation of non-equilibrium spins in the bulk. One of the possible candidates is AF with bulk inversion asymmetry and strong spin orbit interaction.[17]

References

[1] S. Y. Huang, X. Fan, D. Qu, Y. P. Chen, W. G. Wang, J. Wu, T. Y. Chen, J. Q. Xiao, and C. L. Chien, Phys. Rev. Lett. **109**, 107204 (2012).

[2] Y. M. Lu, Y. Choi, C. M. Ortega, X. M. Cheng, J. W. Cai, S. Y. Huang, L. Sun, and C. L. Chien, Phys. Rev. Lett. **110**, 147207 (2013).

[3] D. Qu, S. Y. Huang, J. Hu, R. Wu, and C. L. Chien, Phys. Rev. Lett. **110**, 067206 (2013).

[4] M. Kowalewski, W. H. Butler, N. Moghadam, G. M. Stocks, T. C. Schulthess, K. J. Song, J. R. Thompson, A. S. Arrott, T. Zhu, J. Drewes, R. R. Katti, M. T. McClure, and O. Escorcia, J. Appl. Phys. **87**, 5732 (2000).

[5] Y. Liu, C. Jin, Y. Q. Fu, J. Teng, M. H. Li, Z. Y. Liu, and G. H. Yu, J. Phys. D: Appl. Phys. **41**, 205006 (2008).

[6] Y. Liu, Y. Q. Fu, S. Liu, C. Jin, M. H. Li, and G. H. Yu, J. Appl. Phys. **107**, 023912 (2010).

[7] R. Jungblut, R. Coehoorn, M. T. Johnson, J. aan de Stegge, and A. Reinders, J. Appl. Phys. **75**, 6659 (1994).

[8] X. Y. Lang, W. T. Zheng, and Q. Jiang, Nanotechnology **18**, 155701 (2007).

[9] X. Fan, H. Celik, J. Wu, C. Ni, K. J. Lee, V. O. Lorenz, and J. Q. Xiao, Nat. Commun. **5**, 3042 (2014).

[10] X. Fan, J. Wu, Y. Chen, M. J. Jerry, H. Zhang, and J. Q. Xiao, Nat. Commun. **4**, 1799 (2013).

[11] J. Kim, J. Sinha, S. Mitani, M. Hayashi, S. Takahashi, S. Maekawa, M. Yamanouchi, and H. Ohno, Phys. Rev. B **89**, 174424 (2014).

[12] Y.-T. Chen, S. Takahashi, H. Nakayama, M. Althammer, S. T. B. Goennenwein, E. Saitoh, and G. E. W. Bauer, Phys. Rev. B **87**, 144411 (2013).

[13] K. Garello, I. M. Miron, C. O. Avci, F. Freimuth, Y. Mokrousov, S. Blugel, S. Auffret, O. Boulle, G. Gaudin, and P. Gambardella, Nat. Nanotechnol. **8**, 587 (2013).

[14] K. Masashi, S. Kazutoshi, F. Shunsuke, M. Fumihiro, O. Hideo, M. Takahiro, C. Daichi, and O. Teruo, Appl. Phys. Express **6**, 113002 (2013).

[15] T. Nan, S. Emori, C. T. Boone, X. Wang, T. M. Oxholm, J. G. Jones, B. M. Howe, G. J. Brown, and N. X. Sun, Phys. Rev. B **91**, 214416 (2015).

[16] J. Kim, J. Sinha, M. Hayashi, M. Yamanouchi, S. Fukami, T. Suzuki, S. Mitani, and H. Ohno, Nat. Mater. **12**, 240 (2013).

[17] J. Železný, H. Gao, K. Výborný, J. Zemen, J. Mašek, A. Manchon, J. Wunderlich, J. Sinova, and T. Jungwirth, Phys. Rev. Lett. **113**, 157201 (2014).

[18] H. B. M. Saidaoui, A. Manchon, and X. Waintal, Phys. Rev. B **89**, 174430 (2014).

[19] M. Ekholm and I. A. Abrikosov, Phys. Rev. B **84**, 104423 (2011).

[20] P. Bisantit, G. Mazzonet, and F. Sacchettig, J. Phys. F: Met. Phys. **17**, 1425 (1987).

[21] K. Nakamura, T. Ito, A. J. Freeman, L. Zhong, and J. Fernandez-de-Castro, Phys. Rev. B **67** (2003).

[22] D. Spisak and J. Hafner, Phys. Rev. B **61**, 11569 (2000).

[23] W. J. Antel, F. P. Jr., and G. R. Harp, Phys. Rev. Lett. **83**, 1439 (1999).

[24] F. Y. Yang and C. L. Chien, Phys. Rev. Lett. **85**, 2597 (2000).

[25] V. S. Gornakov, Y. P. Kabanov, O. A. Tikhomirov, V. I. Nikitenko, S. V. Urazhdin, F. Y. Yang, C. L. Chien, A. J. Shapiro, and R. D. Shull, Phys. Rev. B **73**, 184428 (2006).

[26] A. G. Gurevich and G. A. Melkov, *Magnetization oscillations and waves*. (CRC press, Bacon Raton, 1996), p.59.

[27] G. Vallejo-Fernandez, L. E. Fernandez-Outon, and K. O'Grady, J. Phys. D: Appl. Phys. **41**, 112001 (2008).

[28] M. R. Fitzsimmons, J. A. Eastman, R. B. Von Dreele, and L. J. Thompson, Phys. Rev. B **50**, 5600 (1994).

[29] M. J. Donahue and D. G. Porter, OOMMF User's Guide **Version 1.2a5**, http://math.nist.gov/oommf.

[30] W. Zhang, M. B. Jungfleisch, W. Jiang, J. E. Pearson, A. Hoffmann, F. Freimuth, and Y. Mokrousov, Phys. Rev. Lett. **113**, 196602 (2014).

[31] C. Du, H. Wang, F. Yang, and P. C. Hammel, Phys. Rev. B **90**, 140407(R) (2014).

[32] P. Merodio, A. Ghosh, C. Lemonias, E. Gautier, U. Ebels, M. Chshiev, H. Béa, V. Baltz, and W. E. Bailey, Appl. Phys. Lett. **104**, 032406 (2014).

[33] A. Fert and H. Jaffrès, Phys. Rev. B **64**, 184420 (2001).

[34] H. Wang, C. Du, P. C. Hammel, and F. Yang, Phys. Rev. Lett. **113**, 097202 (2014).

[35] H. Wang, C. Du, P. C. Hammel, and F. Yang, Phys. Rev. B **91**, 220410(R) (2015).

[36] J. Bass and W. P. Pratt, J. Phys.: Condens. Matter **19**, 183201 (2007).

[37] R. Acharyya, H. Y. T. Nguyen, W. P. Pratt, and J. Bass, J. Appl. Phys. **109**, 07C503 (2011).

[38] H. Ulrichs, V. E. Demidov, S. O. Demokritov, W. L. Lim, J. Melander, N. Ebrahim-Zadeh, and S. Urazhdin, Appl. Phys. Lett. **102**, 132402 (2013).

Chapter 5 Thickness Dependence of Spin Hall Magnetoresistance in FeMn/Pt Bilayers

In the last chapter, we investigated the spin current interaction with FeMn sub-lattices mainly by quantification of the SOT effect in FeMn/Pt bilayers. Following the spin Hall effect argument, the observations can be reasonably explained by the macro-spin model. However, questions remain as to whether the simplified macro-spin treatment can fully account for the complicated spin configuration of FeMn, especially when it is in the form of ultra-thin film. In order to address this concern, we attempted to estimate the SOT strength from SMR, a complementary effect to SOT. Both effects arise from the spin current in Pt: the SOT is resulted from absorption of spin current by the FM, while the SMR is from the reflected spin current back to the HM. If this is also the case with FeMn/Pt, we may use the SMR to estimate the SOT strength in FeMn/Pt bilayers. To this end, in this chapter, we systematically analyze the strength of SMR in FeMn/Pt bilayers with different thicknesses, from which the SOT strength is extracted. The obtained values are consistent with the SOT effective field values extracted from the PHE measurements described in Chapter 4.

5.1 Sample structure

Two series of FeMn/Pt bilayer samples in the form of Hall bars were prepared on SiO_2(300 nm)/Si substrates (starting from the FeMn layer) using combined techniques of sputtering and photolithography. The two series of samples have the structure of (i) FeMn(t_{FeMn})/Pt(3) and (ii) FeMn(3)/Pt(t_{Pt}) (number inside the parentheses indicates the thickness in nm). The thicknesses of FeMn (t_{FeMn}) and Pt (t_{Pt}) were varied in the range of 0.5 – 15 nm and 1 – 15 nm, respectively. In addition, we also fabricated a series of NiFe(t_{NiFe})/Pt(3) control samples with t_{NiFe} = 0.5 – 15 nm for comparison purpose. The detailed conditions of deposition using sputtering and photolithography using laser wrtier are listed in Chapter 3.

5.2 Experimental results

5.2.1 Field dependent MR (FDMR) measurements

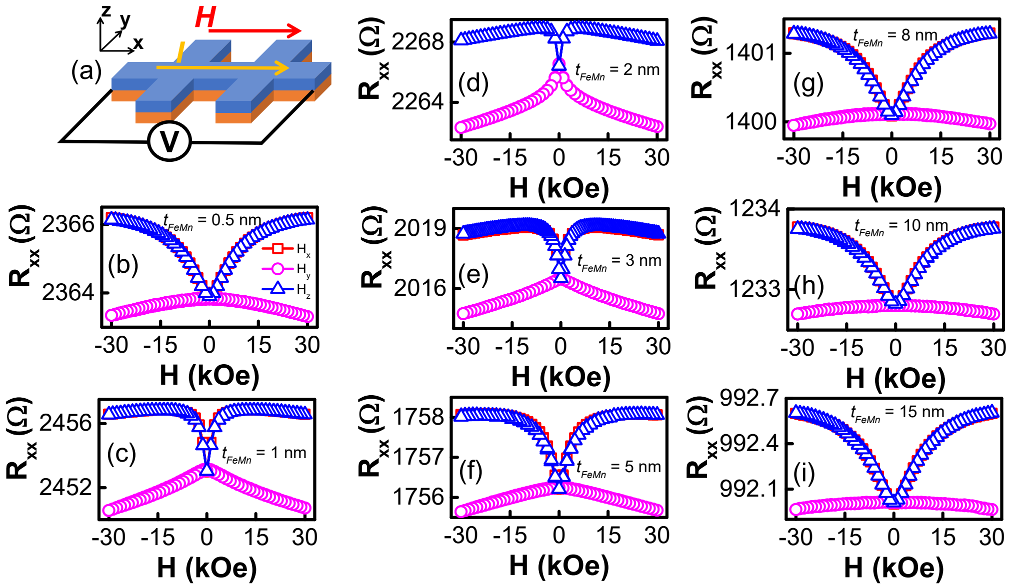

FIG. 5.1 (a) Schematic of field dependent MR measurement; Field-dependent MR for FeMn(t_{FeMn})/Pt bilayers with (b) t_{FeMn} = 0.5 nm; (c) t_{FeMn} = 1 nm; (d) t_{FeMn} = 2 nm; (e) t_{FeMn} = 3 nm; (f) t_{FeMn} = 5 nm; (g) t_{FeMn} = 8 nm; (h) t_{FeMn} = 10 nm; (i) t_{FeMn} = 15 nm.

As illustrated in Fig. 5.1(a), in the first round of measurements, conventional field-dependent MR measurements were performed on series (i) samples with t_{FeMn} = 0.5 – 15 nm with the sweeping magnetic field H applied in x-, y-, z- direction, respectively. Figs. 5.1(b) – (i) show the typical field-dependent MR results for samples with t_{FeMn} = 0.5 nm, 1 nm, 2 nm, 3 nm, 5 nm, 8 nm and 15 nm, respectively. The general observations are (i) the MRs in

x- and z-directions have the same polarity and are much larger than the MR in y-direction, and (ii) the MR in z-direction cannot be explained by the conventional anisotropic MR behavior,[1,2] which should give a negative MR in z-direction when the current is applied in x-direction. From the exchange bias study of FeMn/NiFe bilayers,[3] it was found that FeMn starts to show the onset of clear exchange bias only at a thickness around 4 - 5 nm. At t_{FeMn} = 0.5 nm, the FeMn can be considered as a superpara-antiferromagnet at room temperature when it is standalone; however, when contacted with Pt, it behaves more like a FM due to interaction with Pt. When t_{FeMn} increases to 5 nm, weak AF order appears as reflected in the enhancement of coercivity (H_c) in FeMn/NiFe bilayers. Therefore, in both the t_{FeMn} = 0.5 - 5 nm samples [Figs. 5.1(b) – (f)], there is significant amount of uncompensated spins in the FeMn layer and their spin sub-lattices can be rotated easily by the external field. The saturation of exchange bias was found at $t_{FeMn} > 8$ nm. In this sense, when t_{FeMn} increases further to 8 - 15 nm, the AF order becomes more rigid and is difficult to be rotated by the external field. In this case, it is the uncompensated spins at the interface that are responsible for the MR observed in Figs. 5.1(g) – (i).

On the other hand, the MR behavior of FeMn/Pt is found to be insensitive to the change in Pt thickness at a fixed FeMn thickness, except for an increased current shunting effect by thick Pt layer. Shown in Fig. 5.2(a) is an example of the MR curve of FeMn(3)/Pt(15) sample. As can be seen, the shape of MR is similar to that of FeMn(3)/Pt(3) sample [see Fig. 5.1(e)]. These observations are consistent with the magnetometer measurements of coupon films with different FeMn thicknesses presented in the last chapter.

Based on these considerations and the strong dependence of both the magnitude and curve shape of MR on t_{FeMn}, it is apparent that the MR observed in the FeMn/Pt samples is closely related to the spin configuration of FeMn. The same polarity of MR in *x*- and *z*-directions suggests that the MR observed is of SMR origin. Although the so-called Hanle effect MR induced in the Pt layer itself also has the same polarity,[4] its size on the order of 10^{-6}, as verified by a Pt(3)/SiO2/Si control sample [see Fig. 5.2(b)], is too small to account for the MR observed in FeMn/Pt bilayers.

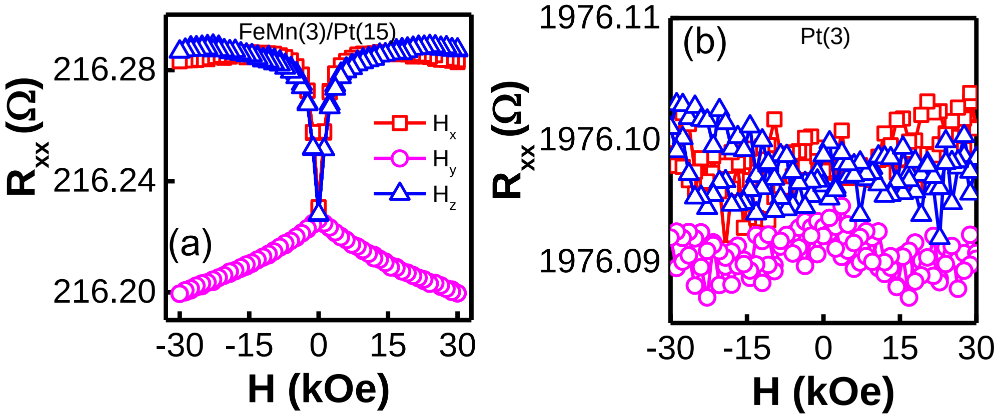

FIG. 5.2 (a) Field-dependent MR for FeMn(3)/Pt(15) bilayers; (b) Field-dependent MR for control sample of Pt(3) on SiO2/Si.

5.2.2 Angle dependent MR (ADMR) measurements

In order to extract the SMR contribution from the overall MR, ADMR measurements were performed on these bilayers. As illustrated in Fig. 5.3(a), the longitudinal resistance of the sample was measured while rotating a constant field *H* in *zy*, *zx*, and *xy* planes, respectively. The SMR ratio is calculated from the relation $\Delta R / R_{xx} = \left(R_{xx}^{z} - R_{xx}^{y}\right) / R_{xx}^{y}$, where R_{xx}^{z} and R_{xx}^{y} are the longitudinal resistance when the magnetization is saturated in *z*- and *y*-direction, respectively. Fig. 5.3(b) shows the ADMR curves for FeMn(3)/Pt(3) measured with a constant field of 30 kOe, which are representative of FeMn/Pt bilayers with different thickness combinations. From Fig. 5.1(e), it can be seen that 30 kOe is large enough to saturate the magnetization of the bilayers in the

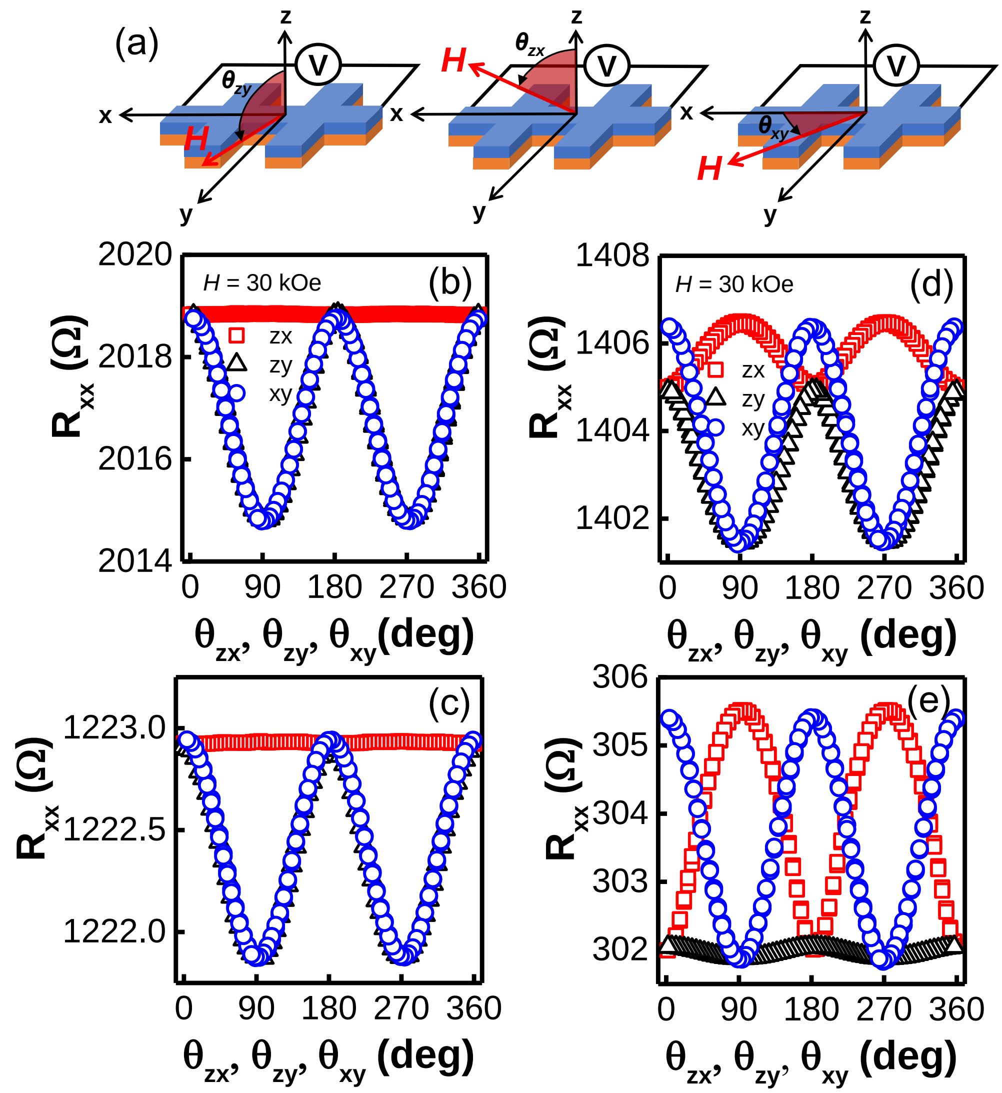

FIG. 5.3 (a) Schematics for ADMR measurement with the applied field rotating in *zy*, *zx*, and *xy* planes, respectively; (b) ADMR results for FeMn(3)/Pt(3) bilayer; (c) ADMR results for FeMn(10)/Pt(3) bilayer; (d) ADMR results for NiFe(3)/Pt(3) bilayer; (e) ADMR results for NiFe(15)/Pt(3) bilayer. The results of (b) - (e) are obtained with an applied field of 30 kOe.

field direction. The general features of the ADMR curves can be summarized as follows: (i) the θ_{zx}-dependence of MR is vanishingly small; (ii) θ_{zy}- and θ_{xy}-dependences of MR are much stronger than that on θ_{zx} and the two curves almost overlap with each other. The vanishing θ_{zx}-dependence of MR indicates that the conventional anisotropic magnetoresistance (AMR) is negligibly small in FeMn/Pt bilayers (note that the SMR should be zero in this measurement configuration). This in combination with the almost overlapping θ_{zy}- and θ_{xy}-dependence of MR again demonstrates clearly that the MR in FeMn/Pt is dominated by SMR. The SMR ratio, on the order of 10^{-3}, is one order of magnitude larger than that of the $SrMnO_3$/Pt system.[5]

The SMR dominating and AMR vanishing feature of the MR effect in FeMn/Pt bilayers is also observed in thick FeMn thickness as shown in Fig. 5.3(c) of a sample with FeMn(10)/Pt(3). The difference with the thinner FeMn sample is the reduced SMR ratio in the thicker sample here. In comparison, Fig. 5.3(d) and (e) show the ADMR results of NiFe(3)/Pt(3) and NiFe(15)/Pt(3) bilayers measured in the same configurations for comparison, respectively. As is clear, one of the main difference as compare to FeMn/Pt is that the AMR (θ_{zx}-dependence of MR) is much larger in this case, which causes a clear separation between the θ_{xy}- and θ_{zy}-dependence of MR curves. It is apparent that the sum of MR measured with the field rotating in the *zx* and *zy* plane is equal to that measured when the field rotates in the *xy* plane. Another sharp difference is that as the NiFe thickness increases, the AMR contribution increases and SMR contribution decreases until the latter finally vanishes and AMR becomes dominating [see Fig. 5.3(e)]. This is not the case with FeMn/Pt in which SMR is always dominating over the entire thickness we investigated. Despite these apparent differences, it is also worth noting that the magnitudes of SMR in both systems are of similar order, and decreases as the FeMn or NiFe thicknesses increases.

5.2.3 Pt-thickness dependence of SMR

To gain a more quantitative understanding of the SMR effect in FeMn/Pt bilayers, we investigated the thickness dependence of the effect for each layer. Fig. 5.4(a) shows the θ_{zy}-dependence of MR for the FeMn(3)/Pt(t_{Pt}) series of samples with t_{Pt} = 1 nm, 2 nm, 5 nm, 8 nm and 15 nm, respectively. As summarized in Fig. 5.4(b), the SMR ratio shows a non-monotonic dependence on the Pt thickness; it increases initially at small thicknesses, peaks at about 3 nm, and then decreases between 3 – 15 nm. The t_{Pt}-dependence of SMR is similar to those observed in CoFeB-based FM/HM bilayers.[6-8] When dealing with metallic FM/HM bilayers, one has to take into account both the charge current shunting effect[8] and the longitudinal spin current that travels into the metallic FM layer.[6,9] Following the drift-diffusion formalism, Kim *et al.* have derived an expression for SMR in FM/HM bilayers:[6]

$$\frac{\Delta R}{R_{xx}} = \theta_{SH}{}^{2}\frac{\lambda_N}{d_N}\frac{\tanh^2\left(d_N/2\lambda_N\right)}{1+\xi}\left[\frac{g_r}{1+g_r\coth(d_N/2\lambda_N)} - \frac{g_F}{1+g_F\coth(d_N/2\lambda_N)}\right] \tag{5.1}$$

with $g_r = \rho_N\lambda_N\,\mathrm{Re}[G_{MIX}]$, and $g_F = \dfrac{(1-P_C{}^2)\rho_N\lambda_N}{\rho_F\lambda_F\coth(d_F/\lambda_F)}$. Here, ρ_N (ρ_F), λ_N (λ_F) and d_N, (d_F) are the resistivity, spin diffusion length and thickness of HM (FM), respectively, Re[G_{MIX}] the real part of the spin mixing conductance, P_C the current spin polarization of FM. $\xi = \rho_N d_F/\rho_F d_N$ is introduced to take into account the current shunting effect by FM. The imaginary part of the spin mixing conductance Im[G_{MIX}] is ignored due to its small magnitude as compared to the real one. For the case of insulating FM/HM system, since $\xi = 0$ and g_F = 0 ($\rho_F \to \infty$), the SMR is only determined by the first term inside the square bracket of Eq. (5.1).[10] The second term is included to account for the longitudinal spin current traveling inside the FM driven by the spin accumulation at the FM/HM interface. Compared with the FM insulator case, the largest correction of SMR happens when P_C approaches 0. In this case, the FM layer is essentially a non-magnetic metal (NM); therefore, the SMR diminishes except for the very small Hanle MR.[4] On the other hand, when P_C approaches unity, the FM becomes a half-metal. In this case, the spin current cannot flow vertically in the FM layer due to lack of minority spin carriers and thus there will be no additional correction to SMR except for the current shunting effect. The situation is more complex in FeMn/Pt bilayers, in particular when FeMn is thin. In this case, the FeMn is neither a good AF nor an FM; its spin structure depends strongly on the thickness. Considering the much smaller spin Hall angle[11,12] and larger resistivity of FeMn as compared to Pt, the spin current generated in FeMn can be neglected. The SMR of FeMn/Pt bilayers is dominantly due to the spin current in Pt. Therefore, without losing generality, we may still use Eq. (5.1) to model the SMR dependence on FeMn thickness, but we have to introduce a thickness-dependent polarization for FeMn. This is a reasonable approach because when t_{FeMn} is large, a rigid AF order will form which results in diminishing polarization. On the other hand, when t_{FeMn} is small (*e.g.*, t_{FeMn} = 3 nm), the net magnetic moment induced by an external field shall lead to a non-zero P_C value. Based on these considerations, we first analyze the t_{Pt}-dependence of SMR with a constant P_C value and then discuss the t_{FeMn}-dependence by taking into account the thickness dependence of polarization, which can be inferred from the magnetization data.

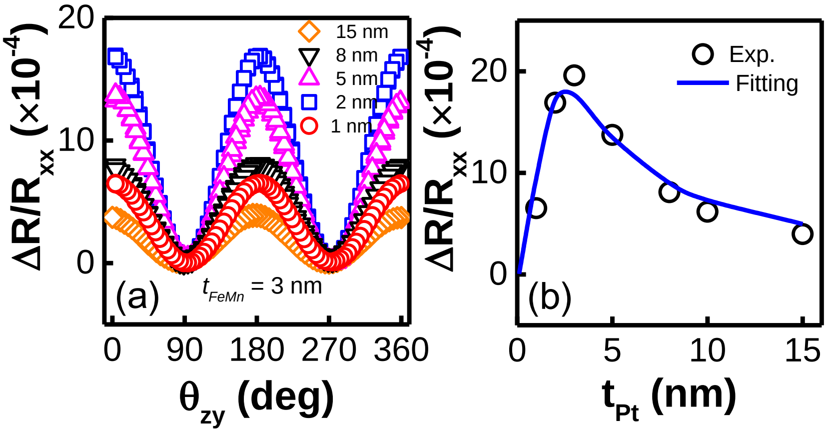

FIG. 5.4 (a) θ_{zy}-dependence of MR for FeMn(3)/Pt(t_{Pt}) bilayers with t_{Pt} = 1 nm, 2 nm, 5 nm, 8 nm and 15 nm, respectively; (b) Pt thickness dependence of SMR ratio for FeMn(3)/Pt(t_{Pt}) bilayers (open circle) and fitting results using Eq. (5.1) (solid line).

As shown in Fig. 5.4(b), the t_{Pt}-dependence of SMR can be fitted reasonably well using Eq. (5.1) (solid line) with fitting parameters: P_C = 0.37, θ_{SH} = 0.2, λ_{Pt} = 1.1 nm, λ_{FeMn} = 2.0 nm and Re[G_{MIX}] = 5.5 × 10^{14} Ω^{-1} m^{-2}. Note that the P_C value used here is obtained from the t_{FeMn}-dependence of magnetization which will be discussed shortly. It should also be noted that it is not possible to obtain θ_{SH} and Re[G_{MIX}] independently based only on SMR results since the value used for one would affect the other. Therefore, during the fitting, we set θ_{SH} = 0.2 and treat Re[G_{MIX}] as a fitting parameter. This is a reasonable assumption considering the fact that the intrinsic spin Hall angle for Pt is reported to be in the range of 0.15 - 0.3.[13-15] As can be seen from Fig. 5.4(b), the fitting agrees quite well with the experiment data. And the fitting values for λ_{Pt} and λ_{FeMn} are comparable with the reported values for Pt[16-18] and FeMn,[3,11,19] respectively. The results indicate that the drift-diffusion model can satisfactorily describe the spin current generation and transport in FeMn/Pt bilayers at a fixed FeMn thickness.

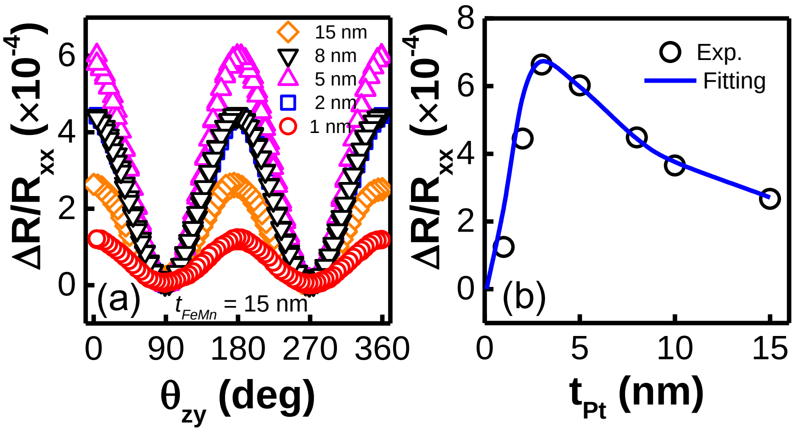

FIG. 5.5 (a) θ_{zy}-dependence of MR for FeMn(15)/Pt(t_{Pt}) bilayers with t_{Pt} = 1 nm, 2 nm, 5 nm, 8 nm and 15 nm, respectively; (b) Pt thickness dependence of SMR ratio for FeMn(15)/Pt(t_{Pt}) bilayers (open circle) and fitting results using Eq. (5.1) (solid line).

It should be noted that the above series of samples with t_{FeMn} = 3 nm correspond to poor AF order regime, *i.e.* the exchange field of sub-lattices is weak and they can be rotated at moderate external field. To further examine the validity of the treatment using Eq. (5.1), we performed the same ADMR measurement on another series of samples with t_{FeMn} = 15 nm (good AF regime) and varying Pt thicknesses. Fig. 5.5(a) shows the θ_{zy}-dependence of MR for the FeMn(15)/Pt(t_{Pt}) series of samples with different Pt thicknesses. Again as summarized in Fig. 5.5(b) (open circle), the SMR ratio also shows a non-monotonic dependence on the Pt thickness with a peak at about 3 nm. Similarly, a reasonably good fitting can be obtained using Eq. 5.1 [solid line in Fig. 5.5(b)]. Table 5.1 compares the fitting parameters obtained from the two series of sample, and also those values reported early in $SrMnO_3$/Pt bilayers.[5] As can be seen from the table, the values obtained in the two series of FeMn/Pt samples are similar to each other (within 15% difference), except for a different spin polarization value (which will be discussed shortly). It should be noted that in this case of t_{FeMn} = 15 nm, the P_C value used here is approaching zero, which is consistent with the fact that the AF order is much more rigid at this thickness. In addition, as is explained above, the slight difference of our values with those extracted from $SrMnO_3$/Pt[5] can be account for by the fact that θ_{SH} and $Re[G_{MIX}]$ are not fully independent. In other words, if one is set at a lower value, a higher value is needed for the other one. All these observations affirm the validity of applying Eq. (5.1) in the FeMn/Pt bilayer.

TABLE 5.1 Summary of the optimized fitting parameters used for the two series of samples with t_{FeMn} = 3 nm and 15 nm, respectively. The spin Hall angle and spin mixing conductance reported early in $SrMnO_3$/Pt are also included.

t_{FeMn} (nm)	P_C	θ_{SH}	λ_{Pt} (nm)	λ_{FeMn} (nm)	$Re[G_{MIX}]$ (Ω^{-1} m^{-2})
3	0.37	0.2	1.1	2.0	5.5×10^{14}
15	0.02	0.2	1.0	2.0	4.8×10^{14}
$SrMnO_3$	NA	0.11	NA	NA	1.34×10^{15}

5.2.4 FeMn-thickness dependence of SMR

We now turn to the t_{FeMn}-dependence of SMR in the bilayers. Fig. 5.6(a) shows the θ_{zy}-dependence of MR for FeMn(t_{FeMn})/Pt(3) bilayers with t_{FeMn} = 0.5 nm, 2 nm, 5 nm, 8 nm, and 15 nm, respectively. For comparison, we also show in Fig. 5.6(b) the θ_{zy}-dependence of MR for NiFe(t_{NiFe})/Pt(3) control samples with t_{NiFe} = 0.5 nm, 2 nm, 5 nm, 8 nm, and 15 nm, respectively. Both series of samples exhibit clear SMR behavior with its magnitude depending on the FeMn or NiFe thickness. It is worth noting that the maximum SMR ratios of the two series of samples are almost the same (2.54×10^{-3} for FeMn/Pt and 2.49×10^{-3} for NiFe/Pt). The detailed t_{NiFe} and t_{FeMn} dependences of SMR are shown in Fig. 5.6(c) and Fig. 5.6(d), respectively. Similar to the Pt thickness dependence shown in Fig. 5.4(b) and Fig. 5.5(b), a non-monotonic dependence on t_{FeMn} or t_{NiFe} is obtained.

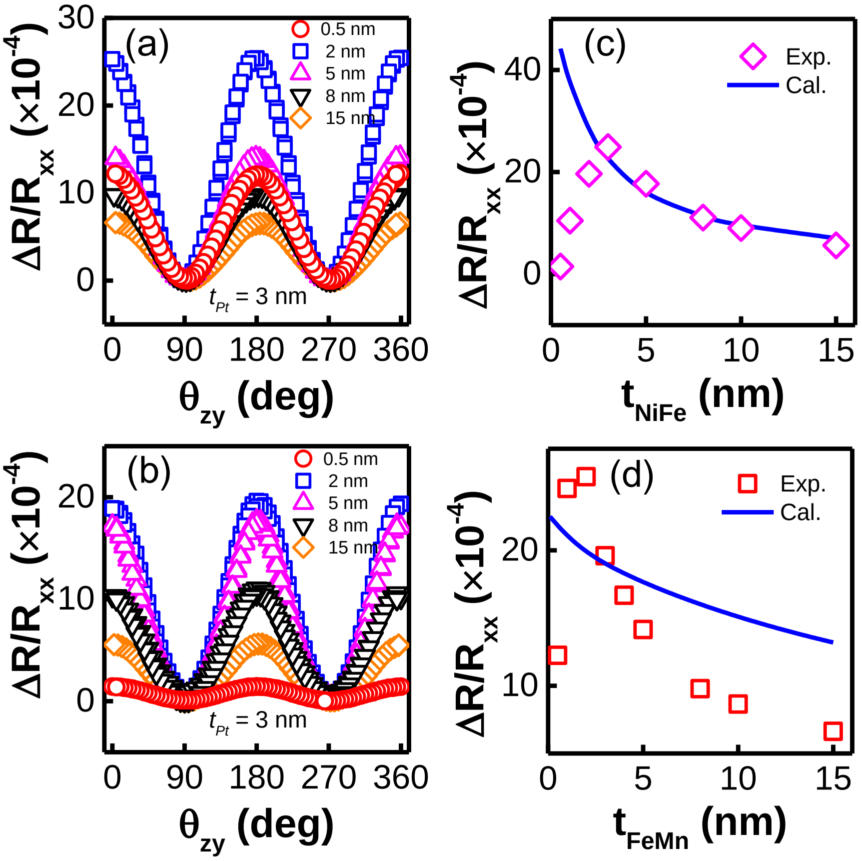

FIG. 5.6 (a) θ_{zy}-dependence of MR for FeMn(t_{FeMn})/Pt(3) bilayers with t_{FeMn} = 0.5 nm, 2 nm, 5 nm, 8 nm and 15 nm, respectively; (b) θ_{zy}-dependence of MR for NiFe(t_{NiFe})/Pt(3) bilayers with t_{NiFe} = 0.5 nm, 2 nm, 5 nm, 8 nm and 15 nm, respectively; (c) NiFe thickness dependence of SMR ratio for NiFe(t_{NiFe})/Pt(3) bilayers (open diamond) and fitting results using Eq. (5.1) (solid line); (d) FeMn thickness dependence of SMR ratio for FeMn(t_{FeMn})/Pt(3) bilayers (open square) and fitting results using Eq. (5.1) (solid line) with fixed $P_C = 0$.

Using Eq. (5.1), the t_{NiFe}-dependence of SMR at large t_{NiFe} can be well reproduced [solid line in Fig. 5.6(c)] with $P_C = 0.4$, $\theta_{SH} = 0.2$, $\lambda_{Pt} = 1.1$ nm, $\lambda_{NiFe} = 4.0$ nm and Re[G_{MIX}] = $1.2 \times 10^{15}\ \Omega^{-1}\ \mathrm{cm}^{-2}$. The P_C and λ_{NiFe} values are from literature. [20,21] The deviation at $t_{NiFe} < 3$ nm can also be attributed to the roughness and surface effect which has not been taken into account in Eq.

(5.1). On the contrary, despite the fact that both the t_{Pt}-dependence and t_{NiFe}-dependence of SMR can be explained reasonably well using Eq. (5.1) [Fig. 5.4(b), Fig. 5.5(b) and Fig. 5.6(c)], the same equation is unable to fit the t_{FeMn}-dependence if we use a fixed P_C value. As can be seen, the fitting in Fig. 5.6(d) (solid line) with a fixed $P_C = 0$ shows a large deviation with the experimental values (open square).

As mentioned above, to account for t_{FeMn}-dependence, it is necessary to use a t_{FeMn}-dependent P_C value for FeMn. It is noticed that in metallic FMs, the tunneling spin polarization (P_T) is approximately linear to the magnetization, *i.e.*, $P_T \propto M_s$.[22,23] As a first approximation, we assume that the same relation also holds for current spin polarization (P_C) used in Eq. (5.1) and net magnetization in thin AF layers. This is supported by the fact that: i) P_C determined by point-contact Andreev reflection spectroscopy is similar to P_T determined by the superconductor tunneling spectroscopy for many transition metallic FMs;[24] ii) sizable net moment can be induced in FeMn by an external field (30 kOe in the SMR measurement). In this sense, we may correlate P_C with the net magnetization M_s of FeMn obtained by magnetometry measurements. Fig. 5.7(a) shows the thickness dependence of M_s for FeMn at H = 30 kOe extracted from the M-H loops of coupon films with the same thickness combination as the Hall bar samples.[3] As can be seen, the non-monotonic t_{FeMn}-dependence of M_s resembles that of SMR [open square in Fig. 5.7(b)] with a peak at round 2 nm, which suggests that the t_{FeMn}-dependence of SMR is closely related to the spin structure of FeMn. More quantitatively, we introduce a phenomenological expression for the current spin polarization $P_C(t_{FeMn}) = \alpha M_s(t_{FeMn})$, where α is a fitting parameter and

$M_s(t_{FeMn})$ is the measured magnetization at different thicknesses. Using the parameters (θ_{SH}, Re[G_{MIX}], λ_{Pt}, λ_{FeMn}) obtained from the fitting of Fig. 5.4(b) and $M_s(t_{FeMn})$ in Fig. 5.7(a), as shown in Fig. 5.7(b), the t_{FeMn}-dependence can be reproduced well (solid line) with a constant α value of 3.1×10^{-3} emu^{-1} cm^3, especially at $t_{FeMn} > 2$ nm. The deviation at small t_{FeMn} below 2 nm may be caused by the roughness and surface effect. It is worth emphasizing again that the curve cannot be fitted at all if we use a constant P_C value. This suggests that the t_{FeMn}-dependence of SMR is mainly determined by the t_{FeMn}-dependence of net magnetization in FeMn induced by an external field. Similar thickness dependence has also been observed in the investigation of spin orbit torque effective field in FeMn/Pt bilayers.[3] These results imply that the SMR is not just an interface effect. The presence of magnetic moment in the layer adjacent to the heavy metal is crucial to obtain a large SMR. It also explains why the SMR is closely related to the spin orbit torque effect in FM/HM and AF/HM bilayers.

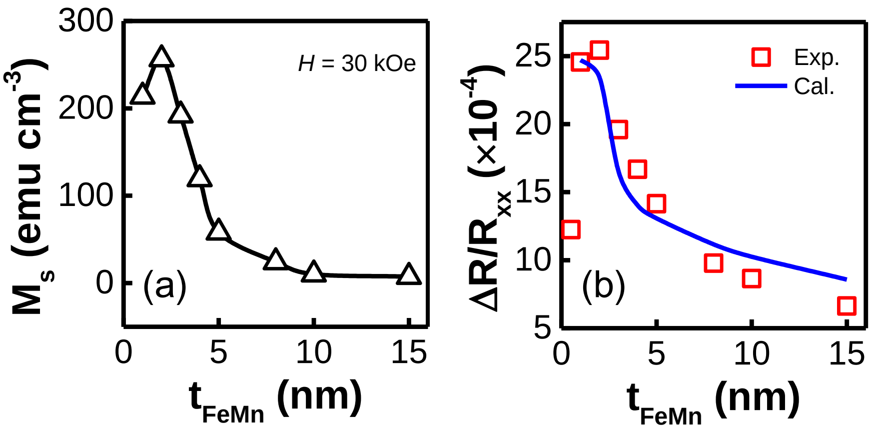

FIG. 5.7. (a) *Ms* at $H = 30$ kOe as a function of FeMn thickness; (b) Fitting of FeMn thickness dependence of SMR ratio with the consideration of thickness dependent P_C [open square: experimental data, solid line: fitting results using Eq. (5.1)].

Although Fig. 5.6(c) and Fig. 5.7(b) are able to reproduce the descending trend of the experimental results above a certain thickness of 2 – 3 nm, both fails at the small thickness range. As briefly mentioned, one of the possibilities is that the spin mixing conductance Re[G_{MIX}] shall be dependent on FM or AFM thickness as well. Recently, Manchon worked out a model for SMR in AFM/HM bilayer,[25] which applies to the collinear AFM with well defined Neel order $\vec{n} = \vec{m}_1 - \vec{m}_2$, where $\vec{m}_1$, $\vec{m}_2$ are the unit vector of the two spin sublattices, respectively. In general, similar to the case of FM/HM, the absorption/reflection of spin current depends on the angle between the spin polarization and the Neel order vector $\vec{n}$, and thus leads to the modulation of the resistance in HM. The SMR equation is express as:[25]

$$\frac{\Delta R}{R_{xx}} = \frac{\lambda_N \sigma_N}{d_N \sigma_N + d_{AF} \sigma_{AF}} {\theta_{SH}}^2 \left(1 - \cosh^{-1} \frac{d_N}{\lambda_N}\right)^2 \times \frac{(\gamma_{\parallel}\eta_{\parallel} - \gamma_{\perp}\eta_{\perp})}{(1 + \gamma_{\parallel}\eta_{\parallel} \tanh^{-1} \frac{d_N}{\lambda_N})(1 + \gamma_{\perp}\eta_{\perp} \tanh^{-1} \frac{d_N}{\lambda_N})} \tag{5.2}$$

where

$$\eta_{\parallel,\perp} = 1 + (r_{\parallel,\perp} \sigma_{\parallel,\perp}^{AF} / \lambda_{\parallel,\perp}^{AF}) \tanh(\frac{d_{AF}}{\lambda_{\parallel,\perp}^{AF}}) \tag{5.3}$$

$$\gamma_{\parallel,\perp} = (\lambda_{\parallel,\perp}^{AF} \sigma_N / \lambda_N \sigma_{\parallel,\perp}^{AF}) \tanh^{-1}(\frac{d_{AF}}{\lambda_{\parallel,\perp}^{AF}}) \tag{5.4}$$

with $\lambda_{\parallel}^{AF} = \sqrt{D_{\parallel}^{AF} \tau_{sf}^{AF}}$, $\lambda_{\perp}^{AF} = \sqrt{D_{\perp}^{AF} / (1/\tau_{sf}^{AF} + 1/\tau_{\varphi}^{AF})}$. Here, the subscript $\parallel(\perp)$ refers to the situation when the spin polarization aligns parallel (transverse) to the Neel order parameter, D^{AF} the electron diffusion coefficient in AF, τ_{sf}^{AF} the conventional isotropic spin relaxation time, τ_{φ}^{AF} the spin dephasing time that relaxes only the spin component that is transverse to the Neel order parameter, r the interfacial resistivity. As can be seen from the equation, in this model, the absorption of the transverse spin current at the interface ($\lambda_{\perp}^{AF}$) is separated from that of the longitudinal spin current in AF ($\lambda_{\parallel}^{AF}$). Moreover, as can be identified, the effective spin mixing conductance $\mathrm{Re}[G_{MIX}] = \frac{1}{2}\sigma_{\perp}^{AF}\tanh(\frac{d_{AF}}{\lambda_{\perp}^{AF}})/\lambda_{\perp}^{AF}$ is dependent on the AF thickness, which is a major difference as compared to the model discussed above.[6,9] If we further proceed to use this model for calculation, as shown in Fig. 5.8, both the experimental Pt and FeMn thickness dependence of SMR can be reasonably fitted, respectively. As summarized in Table 5.2, the parameters used are within the reasonable range for both materials. To facilitate the calculation, we used a spin polarization independent $D = 4\times10^{-4}\ \mathrm{m}^2\ \mathrm{s}^{-1}$, $r = 3\times10^{-16}\ \Omega\ \mathrm{m}^2$.

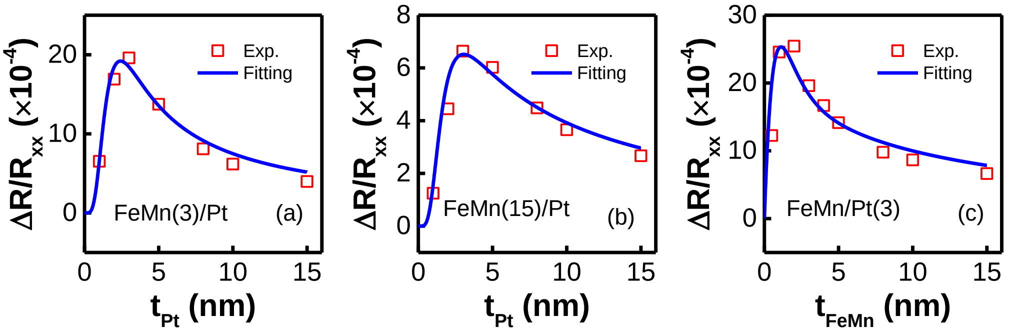

FIG. 5.8 Calculated Pt thickness dependence of SMR in (a) FeMn(3)/Pt, (b) FeMn(15)/Pt, and calculated FeMn thickness dependence of SMR in (c) FeMn/Pt(3) using Eq. (5.2).

Despite the successful reproduction of the experimental results, it should be noted that the spin configuration of FeMn is more complex than the two collinear sublattice used in the model. Moreover, at small thickness with poor sublattice exchange field, FeMn is not a rigid AFM, but rather an uncompensated AFM with sublattices that can be canted under a moderate magnetic field. On one hand, the canting of the sublattices and the respective direction of $\vec{n}$ shall affect the mount of the absorption/reflection of the spin current at the interface. On the other hand, the net moment in FeMn and its direction shall also modulate the absorption/reflection of the spin current.

Therefore, it is believed that the situation of SMR in FeMn/Pt is in between the two discussed models here, *i.e.* with both FeMn thickness dependent Re[G_{MIX}] and P_C.

TABLE 5.2 Summary of the optimized fitting parameters used for the Pt and FeMn thickness dependence of SMR, respectively.

Structure	λ_N (nm)	$\lambda_{\parallel}^{AF}$ (nm)	$\lambda_{\perp}^{AF}$ (nm)	θ_{SH}	τ_{sf}^{AF} (s)	τ_{φ}^{AF} (s)
FeMn(3)/Pt(t_{Pt})	1.0	4.00	1.63	0.27	4.0×10^{-14}	8.0×10^{-15}
FeMn(15)/Pt(t_{Pt})	1.0	4.00	1.75	0.25	4.0×10^{-14}	9.5×10^{-15}
FeMn(t_{FeMn})/Pt(3)	1.1	4.24	1.77	0.30	4.5×10^{-14}	9.5×10^{-15}

5.2.5 Correlation of SMR with SOT

Finally, we try to correlate the observed SMR effect with the SOT effect since both of them originate from SHE generated spin current and the interaction of the spin current with FeMn sub-lattices. As shown in Fig. 5.9(a), an important feature for the observed SOT is the non-monotonic FeMn thickness dependence of H_{FL} (t_{FeMn} = 2 – 5 nm), which is different from the case in FMs. It should be noted that in the following discussion, we focus on correlation of antidamping-like effective field H_{DL} with the SMR due to their common origin. This will not affect the validity of the discussion because H_{DL} and H_{FL} are of similar magnitude.[26-29] To this end, we use the SMR expression derived in Chapter 2 and is reproduced below[8,10]

$$\frac{\Delta R}{R_{xx}}=\theta_{SH}{}^{2}\frac{\lambda_N}{d_N}\frac{\tanh(d_N/2\lambda_N)}{(1+\xi)}(1-\frac{1}{\cosh(d_N/\lambda_N)})\times\frac{g_r(1+g_r)+g_i{}^{2}}{(1+g_r)^2+g_i{}^{2}} \tag{5.5}$$

where the g_F term related to the longitudinal spin current absorption by FeMn layer is ignored for simplicity. On the other hand, the antidamping-like effective field H_{DL} is given by[30]

$$H_{DL} / j_c = \frac{\hbar}{2e} \frac{\theta_{SH}}{M_s d_F} (1 - \frac{1}{\cosh(d_N / \lambda_N)}) \times \frac{g_r(1+g_r) + g_i^2}{(1+g_r)^2 + g_i^2} \tag{5.6}$$

The combination of Eq. (5.5) and (5.6) gives:[3]

$$H_{DL} / j_c = \frac{\hbar}{2e} \frac{1}{\theta_{SH} M_s d_F} \frac{d_N}{\lambda_N} \frac{1}{\tanh(d_N / 2\lambda_N)} \frac{\Delta R}{R_{xx}} \tag{5.7}$$

Note that we have set $\xi = 0$ in Eq. (5.7) since the current shunting effect included in the calculation of SMR has nothing to do with the reflection/transmission of spin current at the FeMn/Pt interface, or in any case, it is much smaller than unity due to the large difference in resistivity between Pt and FeMn. In this way, the thickness dependence of H_{DL}/j_c can be readily calculated from Eq. (5.7) by using the thickness dependence of SMR obtained in Fig. 5.6(d). Fig. 5.9(b) shows the normalized FeMn thickness dependence of H_{DL} calculated from Eq. (5.7). Note that ideally, we should use the moment of FeMn at the interface only for $M_{FeMn}t_{FeMn}$. However, as it is difficult to extract the interface moment independently, we used the volumetric M_{FeMn} instead, which was obtained by the VSM measurement in Fig. 5.7(a). Although it is not exactly the same, the thickness dependence of H_{DL} is indeed similar to the FeMn thickness dependence of H_{FL} presented in Fig. 5.9(a). Therefore, from the results obtained by second order PHE and ADMR measurements, we demonstrated clearly the existence of SOT effect in FeMn/Pt and the non-monotonic dependence of the SOT effective field on FeMn thickness.

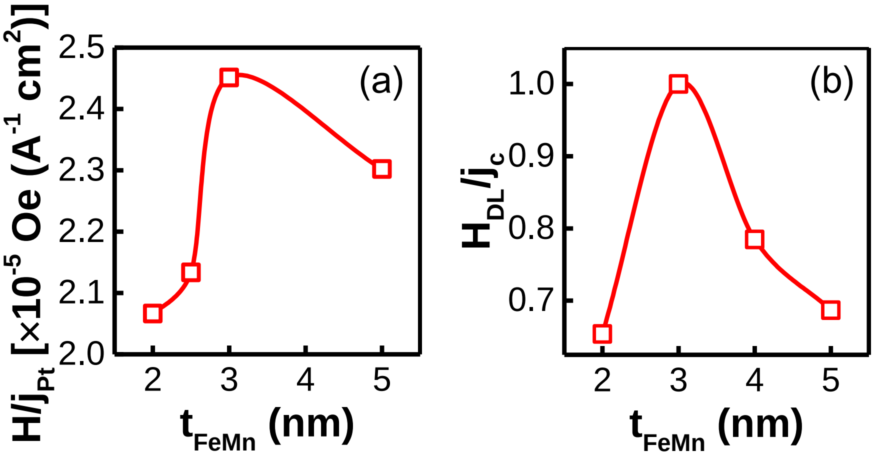

FIG. 5.9 (a) FeMn thickness dependence of H_{FL} extracted from the second order PHE measurements; (b) Calculated FeMn thickness dependence of H_{DL} using Eq. (5.7) from the experimental determined FeMn thickness dependence of SMR ratio and net magnetization.

5.3 Summary

In this chapter, we presented the results on SMR measurements in FeMn/Pt bilayers. The amplitude of the SMR is comparable to that of NiFe/Pt bilayers. A clear FeMn thickness dependence of SMR is observed, which is mainly attributed to the thickness dependence of the net magnetization in FeMn induced by an external field. This is different from the NiFe/Pt bilayers in which the NiFe thickness dependence of SMR is mainly caused by the spin transport in both layers. The close correlation between the SMR and field-like effective field discussed in Chapter 4 unambiguously demonstrated the existence of SOT effect in FeMn/Pt bilayers.

References

[1] H. Nakayama, M. Althammer, Y. T. Chen, K. Uchida, Y. Kajiwara, D. Kikuchi, T. Ohtani, S. Geprags, M. Opel, S. Takahashi, R. Gross, G. E. Bauer, S. T. Goennenwein, and E. Saitoh, Phys. Rev. Lett. **110**, 206601 (2013).

[2] Y. Yang, B. Wu, K. Yao, S. Shannigrahi, B. Zong, and Y. Wu, J. Appl. Phys. **115**, 17C509 (2014).

[3] Y. Yang, Y. Xu, X. Zhang, Y. Wang, S. Zhang, R.-W. Li, M. S. Mirshekarloo, K. Yao, and Y. Wu, Phys. Rev. B **93**, 094402 (2016).

[4] S. Velez, V. N. Golovach, A. Bedoya-Pinto, M. Isasa, E. Sagasta, M. Abadia, C. Rogero, L. E. Hueso, F. S. Bergeret, and F. Casanova, Phys. Rev. Lett. **116**, 016603 (2016).

[5] J. H. Han, C. Song, F. Li, Y. Y. Wang, G. Y. Wang, Q. H. Yang, and F. Pan, Phys. Rev. B **90**, 144431 (2014).

[6] J. Kim, P. Sheng, S. Takahashi, S. Mitani, and M. Hayashi, Phys. Rev. Lett. **116**, 097201 (2016).

[7] S. Cho, S. H. Baek, K. D. Lee, Y. Jo, and B. G. Park, Sci. Rep. **5**, 14668 (2015).

[8] J. Liu, T. Ohkubo, S. Mitani, K. Hono, and M. Hayashi, Appl. Phys. Lett. **107**, 232408 (2015).

[9] Y. T. Chen, S. Takahashi, H. Nakayama, M. Althammer, S. T. Goennenwein, E. Saitoh, and G. E. Bauer, J. Phys.: Condens. Matter **28**, 103004 (2016).

[10] Y.-T. Chen, S. Takahashi, H. Nakayama, M. Althammer, S. T. B. Goennenwein, E. Saitoh, and G. E. W. Bauer, Phys. Rev. B **87**, 144411 (2013).

[11] W. Zhang, M. B. Jungfleisch, W. Jiang, J. E. Pearson, A. Hoffmann, F. Freimuth, and Y. Mokrousov, Phys. Rev. Lett. **113**, 196602 (2014).

[12] C. Du, H. Wang, F. Yang, and P. C. Hammel, Phys. Rev. B **90**, 140407(R) (2014).

[13] C.-F. Pai, Y. Ou, L. H. Vilela-Leão, D. C. Ralph, and R. A. Buhrman, Phys. Rev. B **92**, 064426 (2015).

[14] T. Nan, S. Emori, C. T. Boone, X. Wang, T. M. Oxholm, J. G. Jones, B. M. Howe, G. J. Brown, and N. X. Sun, Phys. Rev. B **91**, 214416 (2015).

[15] W. Zhang, W. Han, X. Jiang, S.-H. Yang, and S. S. P. Parkin, Nat. Phys. **11**, 496 (2015).

[16] M. Althammer, S. Meyer, H. Nakayama, M. Schreier, S. Altmannshofer, M. Weiler, H. Huebl, S. Geprägs, M. Opel, R. Gross, D. Meier, C. Klewe, T. Kuschel, J.-M. Schmalhorst, G. Reiss, L. Shen, A. Gupta, Y.-T. Chen, G. E. W. Bauer, E. Saitoh, and S. T. B. Goennenwein, Phys. Rev. B **87**, 224401 (2013).

[17] N. Vlietstra, J. Shan, V. Castel, B. J. van Wees, and J. Ben Youssef, Phys. Rev. B **87**, 184421 (2013).

[18] S. R. Marmion, M. Ali, M. McLaren, D. A. Williams, and B. J. Hickey, Phys. Rev. B **89**, 220404(R) (2014).

[19] P. Merodio, A. Ghosh, C. Lemonias, E. Gautier, U. Ebels, M. Chshiev, H. Béa, V. Baltz, and W. E. Bailey, Appl. Phys. Lett. **104**, 032406

(2014).

20 J. Bass and W. P. Pratt, J. Phys.: Condens. Matter **19**, 183201 (2007).

21 J. S. Moodera and G. Mathon, J. Magn. Magn. Mater. **200**, 248 (1999).

22 D. Paraskevopoulos, R. Meservey, and P. M. Tedrow, Phys. Rev. B **16**, 4907 (1977).

23 A. T. Hindmarch, C. H. Marrows, and B. J. Hickey, Phys. Rev. B **72**, 100401(R) (2005).

24 R. J. Soulen Jr, J. M. Byers, M. S. Osofsky, B. Nadgorny, T. Ambrose, S. F. Cheng, P. R. Broussard, C. T. Tanaka, J. Nowak, J. S. Moodera, A. Barry, and J. M. D. Coey, Science **282**, 85 (1998).

25 A. Manchon, arxiv 1609.06521.

26 X. Fan, J. Wu, Y. Chen, M. J. Jerry, H. Zhang, and J. Q. Xiao, Nat. Commun. **4**, 1799 (2013).

27 K. Masashi, S. Kazutoshi, F. Shunsuke, M. Fumihiro, O. Hideo, M. Takahiro, C. Daichi, and O. Teruo, Appl. Phys. Express **6**, 113002 (2013).

28 X. Fan, H. Celik, J. Wu, C. Ni, K. J. Lee, V. O. Lorenz, and J. Q. Xiao, Nat. Commun. **5**, 3042 (2014).

29 K. Garello, I. M. Miron, C. O. Avci, F. Freimuth, Y. Mokrousov, S. Blugel, S. Auffret, O. Boulle, G. Gaudin, and P. Gambardella, Nat. Nanotechnol. **8**, 587 (2013).

30 J. Kim, J. Sinha, S. Mitani, M. Hayashi, S. Takahashi, S. Maekawa, M. Yamanouchi, and H. Ohno, Phys. Rev. B **89**, 174424 (2014).

Chapter 6 Magnetic Properties and Spin Orbit Torque in FeMn/Pt Multilayers

In Chapters 4 and 5, the SOT and SMR effects are investigated in the FeMn/Pt bilayers through the second order PHE and angle dependent MR measurements, respectively. We found both a large field-like SOT effective field and a sizable SMR in these bilayers. These results suggest that spin current can be effectively absorbed by the FeMn spin sub-lattices, which corroborates well with the spin Hall origin of both phenomena. Moreover, both effects are found to be closely related to the net moment inside the FeMn layer, which is determined by its thickness. Previously, it has been reported that proximity effect can induce magnetism in sub-1 nm Pt layer at FeMn/Pt interfaces.[1,2] This suggests that it might be possible to achieve global ferromagnetism in ultra-thin FeMn/Pt multilayers. If this indeed happens, it might be possible to have a ferromagnet with strong spin-orbit coupling due to the presence of Pt and its asymmetrical interfaces with the neighboring FeMn layers. To this end, we have fabricated FeMn/Pt multilayers and investigated their magnetic properties and SOT characteristics. This is the first time that such kind of multilayers have been fabricated and characterized. We will show that it is indeed possible to achieve both global ferromagnetic ordering and SOT-induced switching in the newly created multilayers.

6.1 Sample structure

The FeMn/Pt multilayers consisting of alternate and ultra-thin FeMn and Pt layers were deposited on SiO_2/Si substrates using DC magnetron sputtering with a base and working pressure of 2×10^{-8} Torr and 3×10^{-3} Torr, respectively.

An in-plane field of ~500 Oe was applied during the sputtering deposition to induce a uniaxial anisotropy. In the description hereafter, we adopted the notation [FeMn(t_1)/Pt(t_2)]$_n$ for the multilayer, where t_1, t_2 indicate the thickness of FeMn and Pt in nm, respectively, and n is the repeating period. The basic structural and magnetic properties of the multilayers were characterized on coupon films using XRD, XPS, and VSM. The electrical characterization involves the second order PHE and angle dependent MR measurements as what we did previously with the FeMn/Pt bilayers.

6.2 Experimental results

6.2.1 Structural properties

We first characterized the structural properties of the multilayer coupon films using combined X-ray techniques. Fig. 6.1(a) shows the XRD patterns of two coupon films: [FeMn(0.6)/Pt(0.6)]$_{20}$/Pt(3) (Curve A) and [FeMn(0.6)/Pt(0.6)]$_{20}$ (Curve B), covering the range of bulk fcc Pt (111) peak at 39.8° and bulk fcc FeMn (111) peak at 43.5°, using the Cu Kα radiation. Multilayers with a larger number of periods were used in order to ensure a reasonably good signal-to-noise ratio. The diffraction patterns for both films are dominated by a main peak at 40.2° - 40.3°, which is close to the bulk Pt (111) peak. The difference in the intensity of the two diffraction patterns [inset of Fig. 6.1(a)], *i.e.*, A-B, should be the contribution from the top Pt(3) layer of sample A. As can be seen from the inset, the peak position of the Pt(3) capping layer, 39.9°, is very close to that of the bulk Pt. The shift of the main peak of the multilayer from the bulk value indicates the presence of intermixing at Pt/FeMn interfaces. Same phenomenon has also been observed in Co/Pt multilayers.[9,10] The FeMn (111) peak is almost at the same level of the baseline, which is presumably caused by the combined effect of ultra-thin thickness, interface mixing and small scattering cross sections of Fe and Mn as compared to Pt.

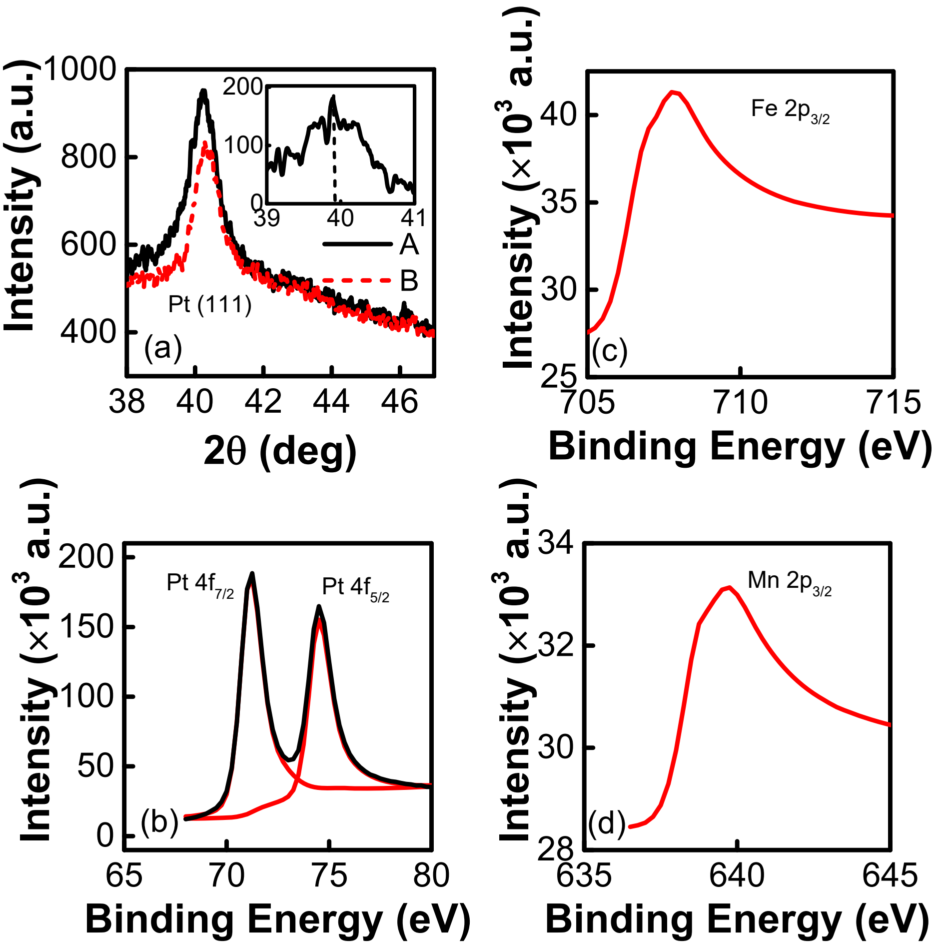

FIG. 6.1 (a) XRD patterns of the multilayer samples: $[FeMn(0.6)/Pt(0.6)]_{20}/Pt(3)$ (Curve A) and $[FeMn(0.6)/Pt(0.6)]_{20}$ (Curve B); (b) – (d) XPS spectra of the Pt(3)/[FeMn(0.6)/Pt(0.6)]20 sample. Inset of (a): intensity difference between A and B.

Figs. 6.1(b), (c) and (d) show the XPS spectra of the same sample. The Pt $4f_{7/2}$ and Pt $4f_{5/2}$ peaks appear to remain at their elemental positions without any obvious shift, while the Fe $2p_{3/2}$ and Mn $2p_{3/2}$ show both broadening and a blue-shift compared to their elemental peaks. The latter is presumably caused by interaction with Pt at interfaces. Oxidation of Fe and Mn is unlikely because the sample is covered by a 3 nm thick Pt layer. The XRD and XPS data demonstrate that the multilayers have a reasonably good (111) texture and sharp interfaces.

To further check the interface quality of the multilayers, we also carried out X-ray reflection (XRR) measurements on samples with same thickness combination but a repeating period $n = 30$ (for better signal to noise ratio). Fig. 6.2 shows the XRR pattern of a coupon film with the structure [FeMn(0.6)/Pt(0.6)]$_{30}$ (solid line). For comparison, the XRR of the co-sputtered FeMn-Pt alloy with the same equivalent composition and thickness (dashed line) as compared to the multilayer is also shown in the same figure. Both XRR spectra show well-defined fringe patterns which give a total thickness of about 34 nm. This is in good agreement with the preset values. For the multilayer sample, in addition to the high-frequency fringe patterns, there is also a broader peak appears at around 7.48°, corresponding to the period of the multilayer which is about 1.15 nm. As this peak is absent in the co-sputtered sample, we can conclude that the multilayers have a well-defined periodicity and sharp interfaces.

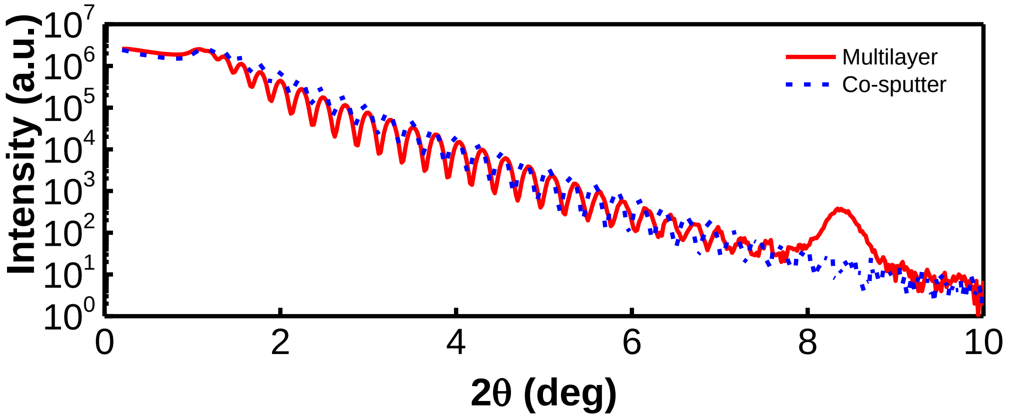

FIG 6.2 XRR patterns for [FeMn(0.6)/Pt(0.6)]$_{30}$ multilayer (solid line) and co-sputtered FeMn-Pt alloy (dashed line) with the same equivalent composition and thickness.

6.2.2 Magnetic properties

Next, the hysteresis (*M-H*) loops and temperature-dependence of magnetization (*M-T*) of [FeMn(t_1)/Pt(t_2)]$_n$/Pt(3) are characterized using coupon films by the VSM module of the VersaLab PPMS. The samples are all with a 3 nm Pt layer for protection. All the multilayer samples exhibit global ferromagnetic behavior with an in-plane anisotropy. Fig 6.3(a) shows a typical example of in-plane and out-of-plane hysteresis loops for the sample with t_1 = t_2 = 0.6 nm and n =5, measured at room temperature, respectively. As can be seen from the figure, the coercivity (H_c) and the saturation magnetization (M_s) of the sample are 1 Oe and 286.8 emu cm^{-3}, respectively. Both the small M_s and H_c facilitate SOT-induced magnetization switching with a small current. Although not show here explicitly, H_c and M_s increase to 108 Oe and 795.4 emu cm^{-3}, respectively as the temperature goes down to 50 K, both of which are typical behaviors for FM.

To better understand the origin of ferromagnetism in multilayer, the temperature dependence of M_s (the *M-T* curve) is measured for samples with varying FeMn and Pt thickness combination. Figs. 6.2(b)-(d) show the *M-T* curves of different multilayers with the legend denoting (t_1, t_2) × n. The curves were obtained by first cooling the sample from 300 K to 50 K and then recording the magnetic moment during warming up process from 50 K to 380 K with an applied in-plane field of 1000 Oe. As can be seen from Fig. 6.1(a), this field value was sufficient to saturate the magnetization in the field direction. We first start our discussion on the Pt-thickness of magnetic properties. Fig. 6.2(b) shows the *M-T* curves of samples with t_1 = 0.6 nm, n = 5, and t_2 = 0, 0.1, 0.2, 0.4, 0.6, and 1 nm, respectively. At intermedium Pt thickness (t_2 = 0.1 – 0.6 nm), M_s at 50 K gradually increases with t_1 from about 587.9 to 795.4 emu cm^{-3}, while the Curie temperature (T_C) falls in the range of 350 K – 420 K, which varies non-monotonically with t_2. However, T_C drops sharply to about 260 K for both samples with t_2 = 0 nm and t_2 = 1 nm. The former is essentially a FeMn(3)/Pt(3) bilayer. As we discussed in detail in Chapter 4, the sizable M_s below 260 K can be mainly attributed to the sub-lattice canting due to the softening of FeMn spin sub-lattices at small thickness. It should be noted that although it has been reported that Pt can be polarized easily when in contact with FMs[11-15], our control experiments using

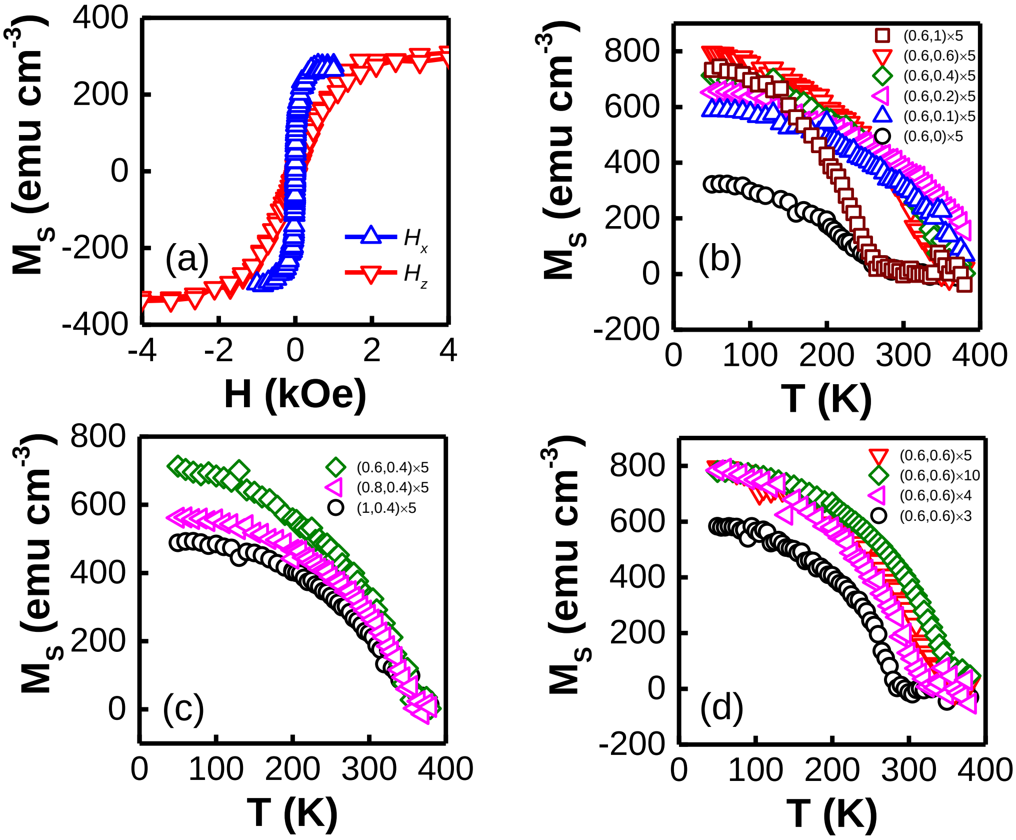

FIG 6.3 (a) Hysteresis loops of [FeMn(0.6)/Pt(0.6)]$_5$/Pt(3), measured at 300 K with in-plane field (H_x) and out-of-plane field (H_z); (b) - (d) Saturation magnetization of samples [FeMn(t_1)/Pt(t_2)]$_n$/Pt(3) as a function of temperature (M-T curve). The legend (t_1, t_2)×n denotes a multilayer with a FeMn thickness of t_1, Pt thickness of t_2, and a period of n.

FeMn/Au and FeMn/Ta revealed that such proximity effect induced magnetism in FeMn/Pt is small. Nevertheless, despite its small contribution to the magnetic moment, the Pt layer plays an important role in promoting FM order throughout the multilayers at Pt thickness below 0.6 nm. In this thickness range, the proximity effect from both sides of Pt is able to couple with each other, leading to the observed global FM order. On the other hand, when the thickness is beyond a certain threshold, the central regions of the individual Pt layers remain un-polarized, isolating the FM order at each side. This is the reason why T_C of the t_2 = 1 nm sample drops back to the same level of FeMn(3)/Pt(3), but its magnetization is much larger than that of the latter due both increased number of interfaces and further softening of the FeMn layers.

We now turn to the FeMn thickness dependence of magnetic properties. Fig 6.3(c) shows the *M*-*T* curves of samples with t_2 = 0.4 nm, n = 5, and t_1 = 0.6, 0.8, and 1 nm, respectively. As can be seen, the M_s at low temperature decreases with increasing t_1, but T_C remains almost the same. This suggests that FM order is weakened when the thickness of FeMn increases. However, unlike the case of increasing t_2, the increase of t_1 up to 1.0 nm does not lead to a sharp decrease of T_C. In other words, T_C is mainly determined by the degree of polarization of the Pt layer. The last factor investigated is the total thickness, as shown in Fig. 6.3(d). The decrease of n leads to gradual decrease of both M_s and T_C. Both the surface and size effect may play a role here. The multilayer is sandwiched between thin Pt layers at both the top and bottom. When n is small, the less polarized top and bottom Pt layer may affect the magnetic properties of the multilayer, leading to reductions of both M_s and T_C.

The T_C of an FM thin film can be estimated by scaling analysis, *i.e.*, $T_C(\infty) - T_C(d) \propto d^{-1/\upsilon}$, where $T_C(\infty)$ and $T_C(d)$ are the Curie temperature of bulk and thin film with a thickness d, respectively, and υ is the critical exponent of the bulk correlation length in the range of 0.5 to 0.705 (Ref. [16], [17]). The fitting of our data to this equation gives a υ value of 1.6, which is much larger than values obtained for Ni ($\upsilon = 1$) and Gd ($\upsilon = 0.625$) thin films.[16] As we will discuss shortly, this is presumably caused by the finite distribution of T_C itself in the multilayers.

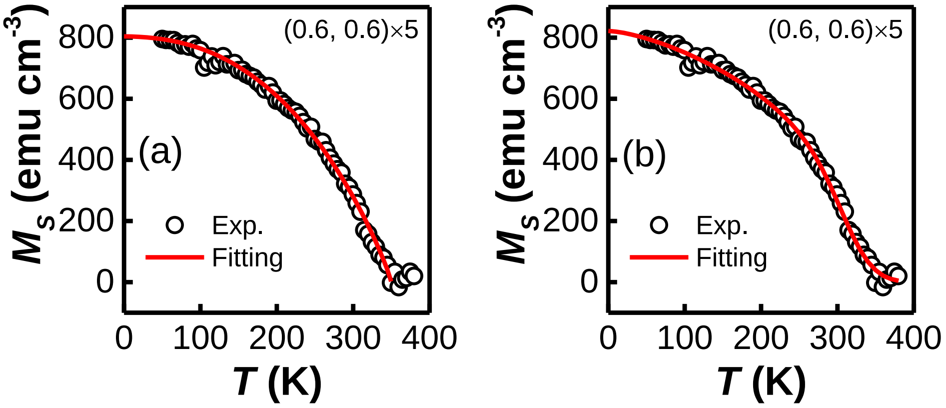

FIG 6.4 (a) Fitting of M-T curve of [FeMn(0.6)/Pt(0.6)]$_5$/Pt(3) sample using Eq. (6.1); (b) Fitting of M-T curve of [FeMn(0.6)/Pt(0.6)]$_5$/Pt(3) sample using Eq. (6.2) with T_C distribution and a β value of 0.365.

As the FeMn/Pt multilayers are new, it is of importance to study their critical behavior so as to have a better understanding of their magnetic properties. The M-T curve of FM generally follows the semi-empirical formula:[18]

$$M(T) = M(0)\left[1 - s\left(\frac{T}{T_C}\right)^{3/2} - (1-s)\left(\frac{T}{T_C}\right)^{5/2}\right]^{\beta} \tag{6.1}$$

where $M(0)$ is the magnetization at zero temperature, T_C is the Curie temperature, β is the critical exponent representing the universality class that the material belongs to, and s is a fitting constant. Fig. 6.4(a) shows an example for the *M-T* curve curving of the sample with [FeMn(0.6)/Pt(0.6)]$_5$/Pt(3) using Eq. (6.1). In general, the *M-T* curves shown in Fig. 6.3 can be fitted reasonably well except that the β values used are 0.68 - 0.9, which are 2 - 3 times larger than that of bulk FM. Since the fitting result is very sensitive to β, the large value used here must be a characteristic of the multilayer sample. Although we notice that β is typically in the range of 0.7 – 0.89 for surface magnetism,[19-22] our multilayers are different from surface magnetism due to their relatively large thickness.

On the other hand, we noticed that T_C of the multilayers depends strongly on the individual thickness (see Fig. 6.3); therefore, it is plausible to assume that there is a finite distribution of T_C inside the multilayer due to the thickness fluctuation induced by the interface roughness. If we assume that T_C follows a normal distribution, Eq. (6.1) can be modified as:

$$\begin{aligned} M(T) = M(0)\int_0^\infty & \left[1 - s\left(\frac{T}{T_C}\right)^{3/2} - (1-s)\left(\frac{T}{T_C}\right)^{5/2}\right]^\beta \\ & \times \frac{1}{\sqrt{2\pi}\Delta T_C}\exp\left[-\frac{(T_C - T_{C0})^2}{2\Delta T_C^{\ 2}}\right] dT_C \end{aligned} \qquad (6.2)$$

where T_{C0} is the mean value of T_C, and ΔT_C is its standard deviation. As shown in Fig. 6.4(b), a better fitting can be achieved in this way, especially in the high temperature region. By assuming a normal distribution of T_C and using β = 0.365 for all the samples (note that β = 0.365 is the critical exponent for *M-T* dependence based on three-dimensional (3D) Heisenberg model). Table 6.1 summarizes the fitting parameters for all the samples. As can be seen, the width of T_C distribution agrees very well with the range of T_C observed in Fig. 6.3 for different samples. These detailed analyses revealed that FeMn/Pt multilayers are 3D FMs with a finite T_C distribution.

TABLE 6.1 Summary of fitting parameters for *M*-*T* curves using Eq. (6.2)

Sample structure	$M(0)$ (emu cm^{-3})	s	T_{C0} (K)	ΔT_C (K)
(0.6,1)×5	790	1.30	245	24
(0.6,0.6)×5	822	1.35	322	30
(0.6,0.4)×5	742	1.55	345	27
(0.6,0.2)×5	675	1.70	400	44
(0.6,0.1)×5	610	1.15	362	57
(0.6,0)×5	338	0.90	242	40
(0.8,0.4)×5	595	1.30	345	25
(1,0.4)×5	515	1.15	337	37
(0.6,0.6)×3	610	1.20	274	16
(0.6,0.6)×4	823	1.50	300	25
(0.6,0.6)×10	804	0.77	339	36

6.2.3 MR and Hall measurements

After clarifying that global FM order exists in the multilayer, we proceed to characterize the Hall bar devices using electrical measurements. Figs 6.5(a) and (b) show the field dependent MR of four devices with the structure Ta(3)/[FeMn(0.6)/Pt(0.6)]$_n$/Pt(3) with n = 4, 5, and 6, measured at a bias current of 1 mA with sweeping magnetic field applied in *x*-direction (H_x) [Fig. 6.5(a)] and *z*-direction (H_z) [Fig. 6.5(b)], respectively. It should be noted that all these devices have a Pt (3) capping layer and a Ta (3) seed layer. As can be seen, the MR with field applied in *x*-direction shows a negative peak at low field with negligible H_c. Although it is not shown here, the MR with field applied in *y*-direction shows a positive peak at low field with similar magnitude. Both observations corroborate with typical AMR behavior of FM. However, on the contrary, the MR with filed applied in *z*-direction shows a characteristic “W” shape below the saturation field [Fig. 6.5(b)], which cannot be explained by the conventional AMR behavior alone.

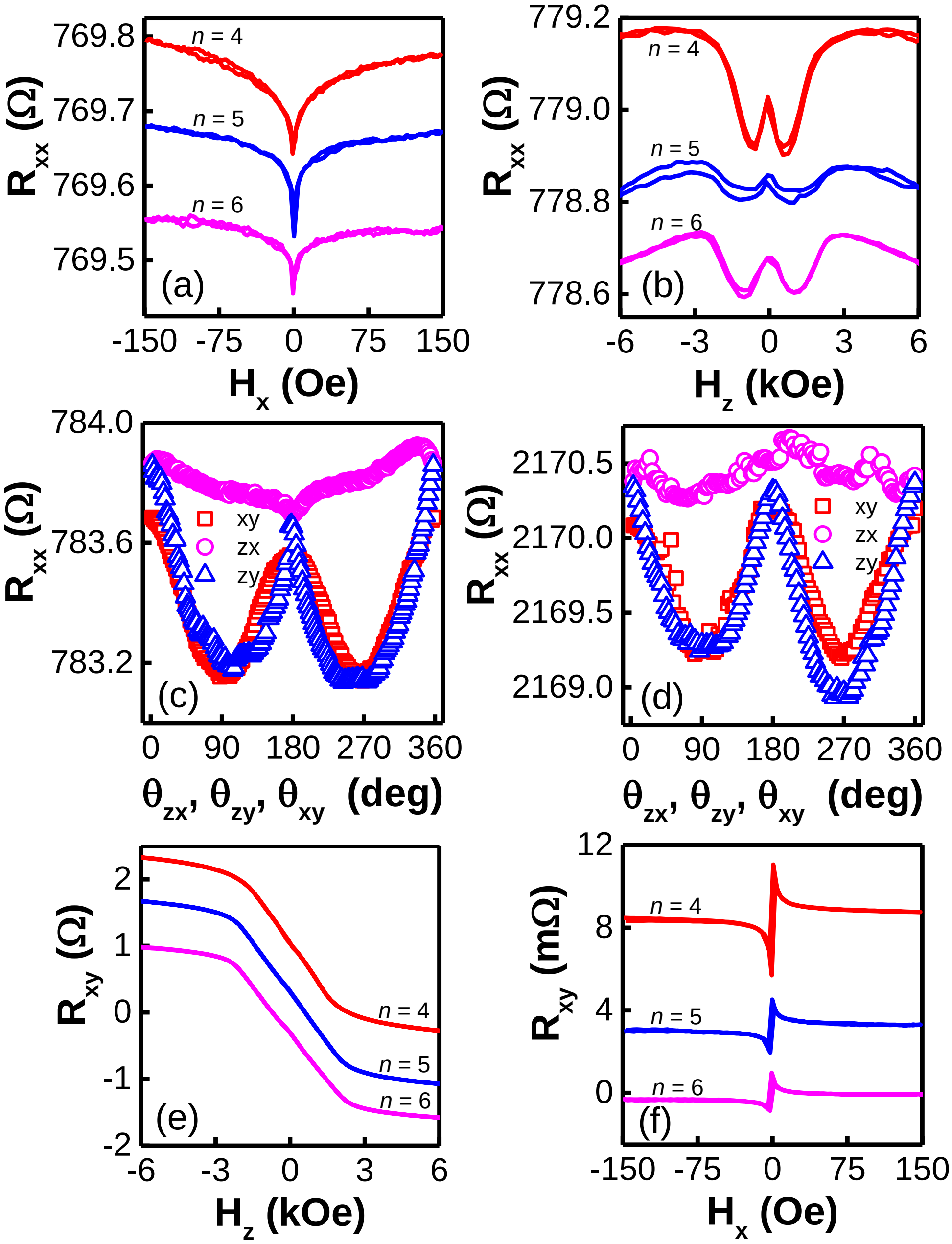

FIG 6.5 MR of Ta(3)/[FeMn(0.6)/Pt(0.6)]$_n$/Pt(3) with *n* = 4, 5, and 6, measured by sweeping the field in (a) *x*-direction and (b) *z*-direction. Angle dependent MR for (c) Ta(3)/[FeMn(0.6)/Pt(0.6)]$_6$/Pt(3) and (d) [FeMn(0.6)/Pt(0.6)]$_6$/Pt(1). (e) – (f) PHR and AHR for the same set of samples shown in (a) and (b). Note that all but the *n* = 6 curve in (a), (b), (e), (f) are vertically shifted for clarity. The zero-field resistance for samples with *n* = 4, 5, and 6 are 912.6, 871.3 and 769.5 Ω, respectively.

The “W” shaped out-of-plane MR curve suggests the presence of another contribution to the MR effect observed here. Considering the previous work with FeMn/Pt bilayer, it is most likely the SMR effect also exists in the multilayer, and entangled with the AMR effect, leading to the unconventional MR shape. In order to verify this hypothesis, we carried out angle dependent MR measurement by recording the longitudinal resistance while rotating a constant field of 3 kOe in *zy*, *zx* and *zy* planes, respectively. The results are shown in Figs. 6.5(c) and (d) for Ta(3)/[FeMn(0.6)/Pt(0.6)]$_6$/Pt(3) and [FeMn(0.6)/Pt(0.6)]$_6$/Pt(1), respectively. The purpose of including the second sample with a minimum Pt capping thickness of 1 nm is to exclude any effects from the capping and seed layers since both Pt and Ta may lead to a sizable SMR effect.[23-26] As can be seen, the amplitude of θ_{zx}-dependence of MR (AMR) on the order of 10^{-5} is much smaller than that of θ_{zy}-dependence of MR (SMR) on the order of 10^{-4}, which indicates that the MR observed in Fig. 6.5(a) and (b) is dominated by SMR. Moreover, the comparable SMR ratio of [FeMn(0.6)/Pt(0.6)]$_6$/Pt(1) (6.1×10^{-4}) with Ta(3)/[FeMn(0.6)/Pt(0.6)]$_6$/Pt(3) (7.9×10^{-4}) further demonstrates that the observed SMR is mainly from the multilayer itself. Although it has been argued that other than SMR[27], spin-dependent scattering due to spin-orbit coupling[28] at the FM/HM interface can also give rise to similar angle dependence of MR, we believe that the SMR scenario is more relevant in the multilayer structures. In these samples, the individual Pt layers serves as a source for both SHE and ISHE. The FeMn layer in between serves as a “spin-current valve”, which controls the relative amount of spin currents that can reach a specific Pt layer from the neighboring Pt layers. The reflected and transmitted spin-currents combined entering the specific Pt layer will determine the size of the SMR. One more thing to notice is that albeit small (10^{-5}), the AMR contribution (θ_{zx}-dependence) in the multilayers is not vanished as compared to that of the FeMn/Pt bilayer case (10^{-6}). The presence of small AMR and SMR together with the possible small misalignment of the sample with the field direction result in the "W" shaped out-of-plane MR, which we will discuss shortly.

Fig 6.5(e) and (f) show the dependence of planar Hall resistance (PHR) and anomalous Hall resistance (AHR) with magnetic field applied in x- and z-direction, respectively, for the same set of samples as shown in Fig. 6.5(a) and (b). PHR and AHR are obtained by dividing the measured planar and anomalous Hall voltage by the current flowing only inside the multilayer instead of the total current. Phenomenologically, the PHR and AHR have a characteristic polar and azimuth angle dependence, *i.e.*, PHR $\propto \sin 2\varphi$ and AHR $\propto \cos\theta$, respectively, where φ is the angle between the magnetization and positive x direction and θ is the angle between the magnetization and z direction.[29] In general, the PHE curves shown in Fig. 6.5(e) resemble the typical PHE signal of an FM with small coercivity. These curves are essentially proportional to the first order derivatives of the MR curves shown in Fig. 6.5(a). On the other hand, the AHE signal increases linearly at low field and saturate at about ±2 kOe which correlates well with the out-of-plane *M-H* curve in Fig. 6.3(a). The nearly linear increase of the AHE signal from -2 kOe to 2 kOe and clear saturation beyond this field range shows that FM order is developed throughout the multilayer structure, consistent with the magnetic measurement results.

6.2.4 SOT in multilayers

The observation of SMR behavior suggest the presence of SOT in the multilayers as well. To get a quantitative understanding, second order PHE measurements[29,30] were then performed to quantify the strength of current-induced effective field H_{FL} in different samples. Fig. 6.6(a) shows an example of one set of PHE curves with H_{bias} = 0 Oe, + 0.5 Oe and – 0.5 Oe, respectively, at a bias current of 10 mA for the Ta(3)/[FeMn(0.6)/Pt(0.6)]$_6$/Pt(3) sample. As can be seen, the PHE signal magnitude changes with the total field in *y*-direction including both H_I and H_{bias}. The increase of PHE at H_{bias} = + 0.5 Oe indicates that H_I is in positive *y*-direction. Fig. 6.6(b) shows the linear fitting of $\Delta V_{xy}(0)$ against ΔV_{bias} = [ΔV_{xy}(+ 0.5 Oe) - ΔV_{xy}(- 0.5 Oe)] using the data in Fig. 6.6(a). H_I can be calculated from the slope *k* by using the relation $H_I = 2kH_{bias}$. After subtracting the Oersted field (H_{Oe}), the effective-field (H_{FL}) can be obtained. By repeating the process, the H_{FL} in different samples can be extracted.

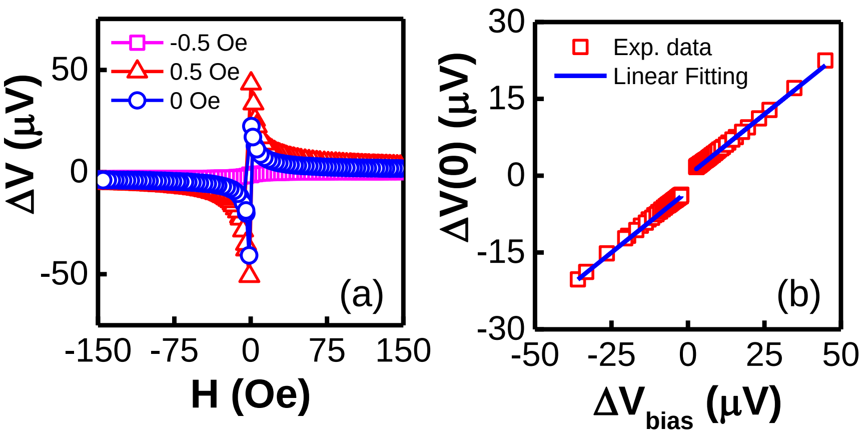

FIG 6.6 (a) One set of PHE curves from Ta(3)/[FeMn(0.6)/Pt(0.6)]$_6$/Pt(3) sample at 10 mA bias current with different transverse bias field (0, +0.5 and -0.5 Oe); (b) Linear fitting of ΔV (H_{bias} = 0 Oe) against [ΔV (H_{bias} = 0.5 Oe) - ΔV (H_{bias} = -0.5 Oe)] to determine the ratio of H_I to H_{bias}.

Fig. 6.7(a) shows the H_{FL} values for [FeMn(0.6)/Pt(0.6)]$_6$/Pt(1) and Ta(3)/[FeMn(0.6)/Pt(0.6)]$_6$/Pt(3) samples. H_{FL} is plotted against the current density in the multilayer portion of the samples (j_{mul}). It is worth noting that the effective fields of both samples are comparable with the samples, especially at low current density regime. This suggests that the effective field is mostly generated inside the multilayer itself; the effect of spin current generated by the thick Pt layer is largely confined near its interface with the multilayer. To further affirm this, Fig. 6.7(b) compares H_{FL} values from the samples $[\text{FeMn}(t_1)/\text{Pt}(t_2)]_5/\text{Pt}(1)$ with fixed FeMn thickness (t_1 = 0.6 nm), but varying Pt thickness (t_2 = 0.2 nm, 0.4 nm, 0.6 nm). As can be seen, H_{FL} increases as the Pt thickness increases, which clearly suggests that the spin current from the Pt layer inside multilayer is responsible for the observed SOT effect. Moreover, as shown in Fig. 6.7(c) for $\text{Ta}(3)/[\text{FeMn}(0.6)/\text{Pt}(0.6)]_n/\text{Pt}(3)$ with n = 4, 5, 6, H_{FL} decreases as the increase of the repeating period. Following the spin Hall effect picture of H_{FL}, the results can be understood as the increasing of the moment per area in the sample as n increases, which is manifest from Fig. 6.3(d). Finally, it is worth noting that H_{FL} obtained in multilayers is generally larger than that from the FM counterpart. Fig. 6.7(d) compares H_{FL} values of $[\text{FeMn}(0.6)/\text{Pt}(0.6)]_4/\text{Pt}$ with that of Ta(3)/NiFe(4.8)/Pt(3) trilayer by plotting it against the current density in the multilayer itself for the former and that in Pt layer for the latter. The thickness of the multilayer (excluding the 1 nm Pt capping layer) is intentionally made the same as that of NiFe in the trilayer structure. As can be seen, at the same current density, the effective field of the multilayer is about 4 times larger than that of the trilayer and the difference is even larger if we take into account only the current flowing through the individual Pt layers inside the multilayer.

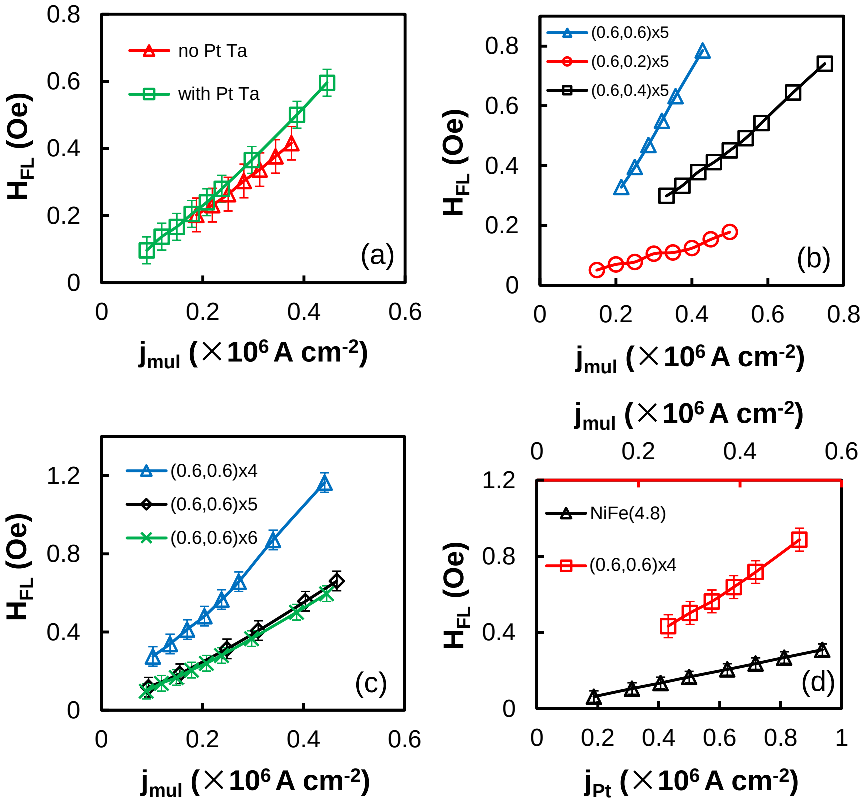

FIG 6.7 (a) A comparison of H_{FL} values for samples with and without Ta seed and Pt capping layer; (b) H_{FL} values for [FeMn(0.6)/Pt(t_2)]$_6$/Pt(1) with t_2 = 0.2 nm, 0.4 nm, 0.6 nm; (c) H_{FL} values for Ta(3)/[FeMn(0.6)/Pt(0.6)]$_n$/Pt(3) with n = 4, 5, 6; (d) A comparison of H_{FL} values for multilayer and NiFe with equivalent FM thickness.

6.2.5 Magnetization switching using SOT

After quantifying the SOT effective field, we now turn to the investigation of magnetization control in multilayers by the SOT effect. As a start, the current sweeping PHE measurements was performed using pulsed DC current with a constant duration of 5 ms and a duty ratio of 2.5%. To ensure good reproducibility, we always started the sweeping from zero current and then gradually increased it to a preset value in both positive and negative directions with a fixed step size. The PHE resistance was obtained by dividing the voltage with the peak value of pulsed current. Figs. 6.8(a) and (b) show the

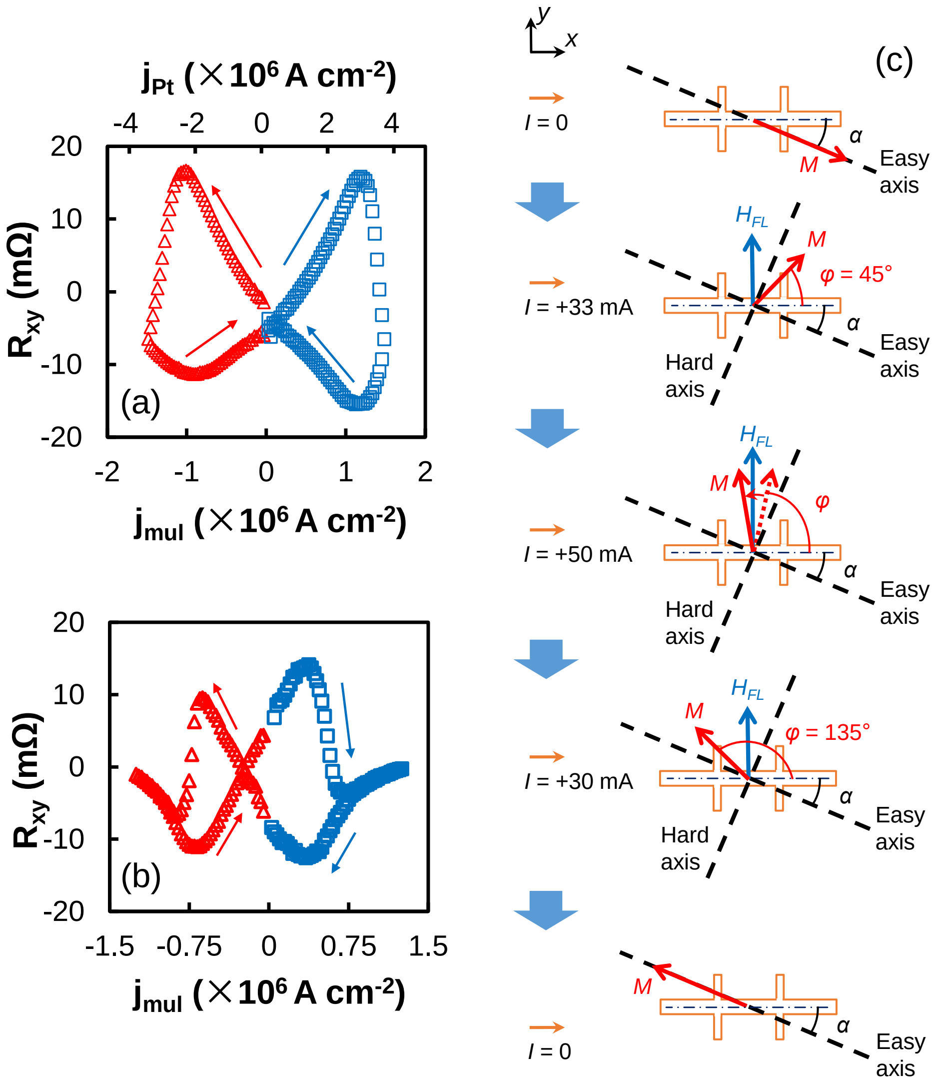

Fig 6.8 (a) Current sweeping PHE curves for (a) Ta(3)/[FeMn(0.6)/Pt(0.6)]$_6$/Pt(3), and (b) [FeMn(0.6)/Pt(0.6)]$_6$/Pt(1); (c) Schematics of the magnetization switching process assisted by anisotropy misalignment, where *I* represents the total current used in (a).

obtained PHE curves as a function of current density in devices with structures of (a) Ta(3)/[FeMn(0.6)/Pt(0.6)]$_6$/Pt(3), and (b) [FeMn(0.6)/Pt(0.6)]$_6$/Pt(1), respectively. Due to the large resistivity of Ta as compared to Pt, current passes through the Ta layer can be ignored in the former device. To facilitate the comparison between the two devices, in Fig. 6.8(a), we show the current density in the multilayer in the lower horizontal axis and the current density in the Pt layer in the upper horizontal axis. The detailed measurement sequence is as follow: the pulsed current is first swept from 0 to a positive preset current [50 mA for (a) and 20 mA for (b)], then to the negative preset current with the same peak value by passing zero, and finally back to zero.

The overall shape of the PHE curves can be qualitatively understood after taking into consideration both the current induced H_{FL} and the slight misalignment of the uniaxial anisotropy axis with x-axis. As illustrated in Fig. 6.8(c), following the macro-spin model, at zero pulsed current, with the small anisotropy of the multilayer, it is reasonable to assume that the magnetization of the cross area of the Hall bar lies at an effective easy axis that is slightly away from the x-axis with an angle α (*e.g.*, − 10°). As the current increases gradually, the increased H_{FL} competes with the effective anisotropy field (H_A), leading to an in-plane rotation of the magnetization towards y-direction to an angle of $\varphi - \alpha$, where φ is the angle between the magnetization and x-axis. The PHE resistance reaches the first positive maximum when $\varphi = 45^\circ$. At the preset value (50 mA in this case), the magnetization aligns at a direction that is slightly passing over the y-axis towards the negative x-direction due to the presence of the uniaxial H_A. When the current gradually decrease from this preset value, the magnetization will continue to be rotated in anticlockwise direction and settle down in the opposite direction, *i.e.*, $\varphi = 180^\circ + \alpha$. After the current returns to zero, the magnetization will align at the opposite direction along the effective easy axis. During this quadrant of sweeping, a negative peak in PHE resistance appears when $\varphi = 135^\circ$. Following the above scenario, the magnetization will continue to be rotated in anticlockwise direction when the current is swept from zero to − 50 mA and then back to zero. During this process, the PHE resistance first reaches a positive maximum at φ = 225° and then a negative maximum at φ = 315° (not shown here). The magnetization will go back to the initial equilibrium direction after a full cycle of current sweeping. Therefore, the results in Figs. 6.8(a) and (b) demonstrate clearly that the magnetization of the multilayer device can be switched from one direction to its opposite, and then back to its initial direction. It is worth noting that such kind of reversible switching can also be realized in a bare multilayer without an additional thick Pt layer [see Fig. 6.8(b)]. Furthermore, the threshold current density is even smaller than that of the samples with an additional thick Pt layer.

To further demonstrate reversible magnetization switching of the multilayer, PHE measurements were performed on $[\mathrm{FeMn}(0.6)/\mathrm{Pt}(0.6)]_6/\mathrm{Pt}(1)$ with alternate write and read pulse as shown schematically in the upper panel of Fig. 6.9(a). The measurement began with the supply of + 20 mA (corresponding to a current density of 1.25×10^6 A cm^{-2}) write current pulse (I_w) with a duration of 5 ms to saturate the magnetization into a specific easy axis direction. Consequently, the reading of this magnetization state is done by measuring the Hall voltage with a 5 ms read current pulse (I_r) of + 2 mA. The reading process was repeated 13 times, and the PHE resistance results are shown in the lower panel of Fig. 6.9(a). Subsequent to this, a negative current pulse of − 20 mA was applied to reverse the magnetization and then read with the same 2 mA current pulse. The write and read cycles were repeated 8 times, as shown in Fig. 6.8(a). Apparently, by doing so, two PHE resistance states are successfully realized. In particular, the readout process can be readily understood with the assistance of the schematic diagram in Fig. 6.9(b). During

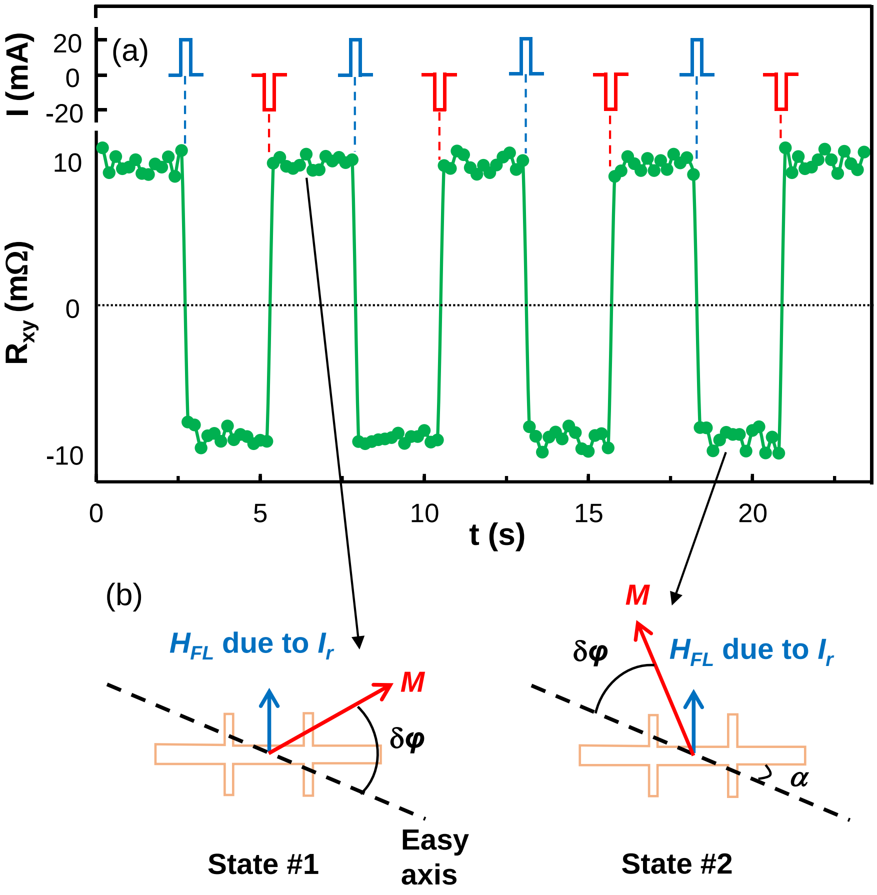

Fig 6.9 (a) Illustration of write current pulses (20 mA with a duration of 5 ms) applied to the [FeMn(0.6)/Pt(0.6)]$_6$/Pt(1) sample (upper panel) and readout signals in terms of PHE resistance (lower panel). Reading is performed with a 2 mA pulse which is repeated 13 times after each writing process; (b) Schematics of magnetization rotation during reading at two states with opposite equilibrium magnetization directions.

readout, the read current pulse (+ 2 mA) induces a small rotation ($\delta\varphi$) of the magnetization towards $+y$ direction from its equilibrium positions, one at angle α (State #1) and the other at α + 180° away from $+x$ direction (State #2). When the read current is chosen properly for a specific value, the magnetization will be rotated to the first octant for State #1 but remains in the second octant for State #2. This leads to Hall resistance of different polarity for the two states, positive for State #1 and negative for State #2. The absolute value of PHE resistance depends on the readout current and misalignment angle α, as shown clearly in Fig. 6.8. The results shown in both Figs 6.8 and 6.9 demonstrated unambiguously reversible switching of magnetization solely by a current without the assist of the external field.

6.2.6 Discussion

We first discuss the unconventional "W" shaped out-of-plane MR [Fig. 6.5(b)]. As is observed from the angle dependent MR measurements [Fig. 6.5(c) and (d)], both AMR and SMR exists in the multilayer sample. It has been reported that the AMR and SMR can be given by $\rho = \rho_0 + \Delta\rho_{AMR}(\vec{m}\cdot\vec{j})^2$ and $\rho = \rho_0 - \Delta\rho_{SMR}[\vec{m}\cdot(\vec{z}\times\vec{j})]^2$,[25] respectively, where $\vec{m}$ and $\vec{j}$ are unit vectors in the direction of magnetization and current, respectively, $\vec{z}$ denotes the normal direction of multilayer stack, ρ_0 is the isotropic longitudinal resistivity, and $\Delta\rho_{AMR}$ ($\Delta\rho_{SMR}$) represents the size of the AMR (SMR) effect. Combining the two effects, the total resistivity of the multilayer can be given by:

$$\rho = \rho_0 + \Delta\rho_{AMR}\sin^2\theta\cos^2\varphi - \Delta\rho_{SMR}\sin^2\theta\sin^2\varphi \tag{6.3}$$

The MR ratio is thus given by:

$$\frac{\rho-\rho_0}{\rho_0} = \frac{\Delta\rho_{AMR}}{\rho_0}\sin^2\theta\cos^2\varphi - \frac{\Delta\rho_{SMR}}{\rho_0}\sin^2\theta\sin^2\varphi \tag{6.4}$$

In order to calculate the overall MR, one has to find the equilibrium values for θ and φ at different applied field based on the energy minimization method. By taking into account the Zeeman energy, anisotropy energy and demagnetizing energy, the energy density can be written as:

$$\frac{E}{M_s} = -\vec{H}\cdot\vec{m} - \frac{H_K}{2}\sin^2\theta\cos^2(\varphi-\alpha) + \frac{H_d}{2}\cos^2\theta \tag{6.5}$$

where $\vec{m}=(\sin\theta\cos\varphi,\sin\theta\sin\varphi,\cos\theta)$, α is the misalignment of effective easy axis from x-direction due to the Hall bar shape, $H_K = 2K_u / M_s$ is the anisotropy field and H_d is the demagnetizing field. In addition, to account for the possible misalignment of external field from z-direction, we use following expression for the external field:

$$\vec{H} = H(\sin\gamma\cos\chi,\sin\gamma\sin\chi,\cos\gamma) \tag{6.6}$$

where γ and χ are the misaligned polar and azimuth angles, respectively. Eq. (6.5) can be solved numerically to obtain the equilibrium angle φ and θ at a specific H value. The MR ratio can then be calculated from Eq. (6.4). In our samples, $\rho_0 \approx \rho_z$, where ρ_z is the longitudinal resistivity when the magnetization is aligned with the z-direction. By using $\frac{\Delta\rho_{AMR}}{\rho_0} = 3.85\times10^{-4}$ and $\frac{\Delta\rho_{SMR}}{\rho_0} = 7.91\times10^{-5}$ extracted from the experimental results in Fig. 6.5(c)

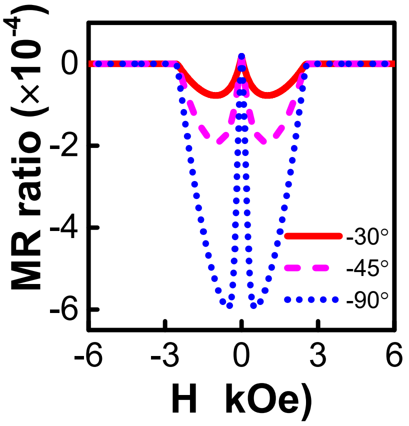

FIG 6.10 Simulated MR ratio of multilayers as a function of sweeping field in z-direction with H_k = 1 Oe and different angle χ (-30°, -45°, -90°).

of the main text, we obtained the simulated MR curves shown in Fig. 6.10. The parameters used are: H_d = 2500 Oe [from Fig. 6.5(f)], α = -10°, γ = 0.1°, χ = -30°, -45°, -90° and H_k = 1 Oe. As can been from the figure, the “W-shape”

MR curve can be reproduced well when there is a slight misalignment of H from the z-axis (γ). On the other hand, the misalignment in xy-plane (χ) changes the amplitude of the signal, but the overall shape still remains almost the same.

The next question is: what could be the SOT generation mechanism in the multilayer without an additional Pt layer, *e.g.*, in the case of [FeMn(0.6)/Pt(0.6)]$_6$/Pt(1)? The observation of clear SMR suggests that spin current is present inside the multilayer. Considering the fact that FeMn has a very small spin Hall angle,[31] we may assume that the spin current is dominantly from the Pt layers. Since both the Pt and FeMn layers are very thin, we may treat the entire multilayer as an FM with a large spin Hall angle. When a charge current is applied to the multilayer in x-direction, the SHE generates a spin current flowing in z-direction with the spin polarization in y-direction, thereby building up spin accumulations at both the top and bottom surfaces. At steady state and under the boundary conditions, $j_{sy}^{z}(0) = j_{sy}^{z}(d) = 0$, the spin current can be calculated from the drift-diffusion equation:

$$j_{sy}^{z}(z) = j_{s0}^{SH}\left[\sinh\frac{z}{\lambda} - \sinh\frac{z-d}{\lambda}\right]\Big/\sinh\frac{d}{\lambda} - j_{s0}^{SH} \tag{6.7}$$

where j_{s0}^{SH} is the SHE spin current, λ is the average spin diffusion length and d is the thickness of the multilayer stack. In the strict sense, Eq. (6.7) is valid only for a pure paramagnet like Pt. In the current case, in addition to Pt, we also have FeMn layers and the entire multilayer is FM. Therefore, the SHE spin current will be partially absorbed and converted to SOT. The absorption is strongest when the polarization of spin current is perpendicular to the magnetization direction and smallest when they are parallel, thereby inducing the SMR-like magnetoresistance. It should be pointed out that in the latter case, spin current can travel through the multilayer because it behaves like a single phase FM, which is different from a FM/HM bilayer. In the extreme case, we may assume that the spin current generated by the Pt layers is completely absorbed by the FeMn layers locally when the polarization of spin current is perpendicular to the local magnetization direction. Under this assumption, there will be no spin accumulation at the two surfaces. The difference in spin current between these two cases gives the SMR as follows:

$$\frac{\Delta R_{xx}}{R_{xx}} = \frac{2\lambda\eta\theta_{SH}{}^{2}}{d}\left(\cosh\frac{d}{\lambda}-1\right) \tag{6.8}$$

Here, $\eta < 1$ describes the efficiency of spin current absorption in realistic situations. If we use the following parameters: $\eta = 0.5$, $\lambda = 1.5$ nm, $d = 8.2$ nm (total thickness of [FeMn(0.6)/Pt(0.6)]$_6$/Pt(1)), and $\frac{\Delta R}{R_{xx}}$ = 0.0610% [calculated from Fig. 6.5(d)], we obtain an effective spin Hall angle θ_{SH} = 0.058 for this sample. With this spin Hall angle, the antidamping-like effective field to current ratio can be calculated as:

$$H_{DL} / j_c = \frac{\hbar}{2e}\frac{2\eta\theta_{SH}\lambda}{d\mu_0 M_s t_{FeMn}}\left(\cosh\frac{d}{\lambda}-1\right)\Big/\sinh\frac{d}{\lambda} \tag{6.9}$$

If we use the following parameters: $\mu_0 M_s$ = 0.32 T (experimental value), t_{FeMn} = 3.6 nm (total thickness of FeMn) and θ_{SH} = 0.058, we have H_{DL}/j_c = 3.78×10^{-7} Oe/(A/cm^2). Although this value is around 2 - 3 times smaller than the experimentally observed value of H_{FL}/j_c, it is a reasonable estimation considering the fact that the field-like and antidamping-like effective fields are typically on the same order in FM/HM bilayers.[30,32-34].

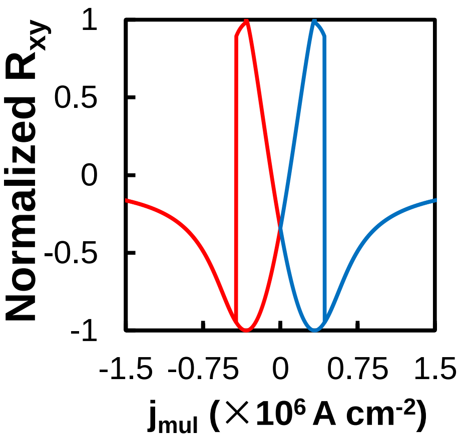

FIG 6.11 Simulated PHE curve as a function of current density in the multilayer using energy minimization.

Lastly, after clarifying the origin of the SOT, the pulsed current sweeping PHE resistance is simulated by taking into account the additional Zeeman energy induced by the SOT effective field. In this way, the energy density of the multilayer can be written as:

$$E / M_s = -H_{FL} \sin\varphi + \frac{1}{2} H_A \sin^2(\varphi - \alpha) \tag{6.10}$$

where $H_A = 2K_u / M_s$ with K_u the anisotropy constant. The magnetization direction with respect to x-direction (φ) at different bias current can be obtained through energy minimization. The normalized PHE resistance is thus calculated following $R_{xy} \propto \sin 2\varphi$. Fig. 6.11 shows the calculated results by using the parameters H_A = 1 Oe, α = -10° and H_{FL}/j_{mul} = 1×10^{-6} Oe (A^{-1} cm^2). As can be seen, the calculated PHE curve agrees qualitatively well with the experimental results shown in Figs. 6.8(a) and (b).

6.3 Summary

We have observed both global FM order and SOT effect in FeMn/Pt multilayers consisting of ultrathin Pt and FeMn layers. The former is characterized by a 3D Heisenberg critical behavior with a finite distribution in T_C. The SOT effect can be understood as the local generation and absorption of spin current by the ultra-thin Pt and its neighboring FeMn layer, respectively. This is different from the FM/HM bilayer case where spin current generated from HM diffuses into FM before it is non-locally absorbed by FM. Such kind of "built-in" SOT in a single FM has important implications for spintronics applications.

References

[1] Y. Liu, C. Jin, Y. Q. Fu, J. Teng, M. H. Li, Z. Y. Liu, and G. H. Yu, J. Phys. D: Appl. Phys. **41**, 205006 (2008).

[2] Y. Liu, Y. Q. Fu, S. Liu, C. Jin, M. H. Li, and G. H. Yu, J. Appl. Phys. **107**, 023912 (2010).

[3] S. Bandiera, R. C. Sousa, B. Rodmacq, and B. Dieny, Appl. Phys. Lett. **100**, 142410 (2012).

[4] K. S. Ryu, L. Thomas, S. H. Yang, and S. Parkin, Nat. Nanotechnol. **8**, 527 (2013).

[5] S. K. Kim, Y. M. Koo, V. A. Chernov, and H. Padmore, Phys. Rev. B **53**, 11114 (1996).

[6] K.-F. Huang, D.-S. Wang, H.-H. Lin, and C.-H. Lai, Appl. Phys. Lett. **107**, 232407 (2015).

[7] C. Hin Sim, J. Cheng Huang, M. Tran, and K. Eason, Appl. Phys. Lett. **104**, 012408 (2014).

[8] M. Jamali, K. Narayanapillai, X. Qiu, L. Loong, A. Manchon, and H. Yang, Phys. Rev. Lett. **111**, 246602 (2013).

[9] J. C. A. Huang, M. M. Chen, C. H. Lee, T. H. Wu, J. C. Wu, and C. M. Fu, J. Magn. Magn. Mater. **239**, 326 (2002).

[10] J.-H. Park, C. Park, T. Jeong, M. T. Moneck, N. T. Nufer, and J.-G. Zhu, J. Appl. Phys. **103**, 07A917 (2008).

[11] T. McGuire, J. Aboaf, and E. Klokholm, J. Appl. Phys. **55**, 1951 (1984).

[12] S. Rüegg, G. Schütz, P. Fischer, R. Wienke, W. Zeper, and H. Ebert, J. Appl. Phys. **69**, 5655 (1991).

[13] P. Poulopoulos, M. Angelakeris, D. Niarchos, R. Krishnan, M. Porte, C. Batas, and N. Flevaris, J. Magn. Magn. Mater. **148**, 78 (1995).

[14] C.-J. Lin, G. Gorman, C. Lee, R. Farrow, E. Marinero, H. Do, H. Notarys, and C. Chien, J. Magn. Magn. Mater. **93**, 194 (1991).

[15] S. Emori and G. S. Beach, J. Appl. Phys. **110**, 033919 (2011).

[16] R. Zhang and R. F. Willis, Phys. Rev. Lett. **86**, 2665 (2001).

[17] P. Jensen, H. Dreyssé, and K. Bennemann, Europhys. Lett. **18**, 463 (1992).

[18] M. Kuz'min, Phys. Rev. Lett. **94**, 107204 (2005).

[19] S. Alvarado, M. Campagna, and H. Hopster, Phys. Rev. Lett. **48**, 51 (1982).

[20] J. Voigt, R. Fink, G. Krausch, B. Luckscheiter, R. Platzer, U. Wöhrmann, X. Ding, and G. Schatz, Phys. Rev. Lett. **64**, 2202 (1990).

[21] K. Namikawa, J. Phys. Soc. Jpn. **44**, 165 (1978).

[22] M. Krech, Phys. Rev. B **62**, 6360 (2000).

[23] C. O. Avci, K. Garello, A. Ghosh, M. Gabureac, S. F. Alvarado, and P. Gambardella, Nat. Phys. **11**, 570 (2015).

[24] C. Hahn, G. de Loubens, O. Klein, M. Viret, V. V. Naletov, and J. Ben Youssef, Phys. Rev. B **87**, 174417 (2013).

[25] H. Nakayama, M. Althammer, Y. T. Chen, K. Uchida, Y. Kajiwara, D. Kikuchi, T. Ohtani, S. Geprags, M. Opel, S. Takahashi, R. Gross, G. E. Bauer, S. T. Goennenwein, and E. Saitoh, Phys. Rev. Lett. **110**, 206601 (2013).

[26] Y. Yang, B. Wu, K. Yao, S. Shannigrahi, B. Zong, and Y. Wu, J. Appl. Phys. **115**, 17C509 (2014).

[27] H. Nakayama, M. Althammer, Y.-T. Chen, K. Uchida, Y. Kajiwara, D. Kikuchi, T. Ohtani, S. Geprägs, M. Opel, and S. Takahashi, Phys. Rev. Lett. **110**, 206601 (2013).

[28] S. S. L. Zhang, G. Vignale, and S. Zhang, Phys. Rev. B **92**, 024412 (2015).

[29] X. Fan, J. Wu, Y. Chen, M. J. Jerry, H. Zhang, and J. Q. Xiao, Nat. commun. **4**, 1799 (2013).

[30] Y. Fan, P. Upadhyaya, X. Kou, M. Lang, S. Takei, Z. Wang, J. Tang, L. He, L.-T. Chang, M. Montazeri, G. Yu, W. Jiang, T. Nie, R. N. Schwartz, Y. Tserkovnyak, and K. L. Wang, Nat. Mater. **13**, 699 (2014).

[31] W. Zhang, M. B. Jungfleisch, W. Jiang, J. E. Pearson, A. Hoffmann, F. Freimuth, and Y. Mokrousov, Phys. Rev. Lett. **113**, 196602 (2014).

[32] K. Garello, I. M. Miron, C. O. Avci, F. Freimuth, Y. Mokrousov, S. Blugel, S. Auffret, O. Boulle, G. Gaudin, and P. Gambardella, Nat. Nanotechnol. **8**, 587 (2013).

[33] J. Kim, J. Sinha, M. Hayashi, M. Yamanouchi, S. Fukami, T. Suzuki, S. Mitani, and H. Ohno, Nat. Mater. **12**, 240 (2013).

[34] K. Masashi, S. Kazutoshi, F. Shunsuke, M. Fumihiro, O. Hideo, M. Takahiro, C. Daichi, and O. Teruo, Appl. Phys. Express **6**, 113002 (2013).

Chapter 7 Conclusions and Recommendations for Future Work

7.1 Conclusions

In this work, we have investigated the spin current interaction with the spin sub- lattices of FeMn in both FeMn/Pt bilayers and multi-layers. The main findings are summarized as follows:

Firstly, through 2nd order PHE measurement, in FeMn/Pt bilayers, a field-like SOT effective field of 2.05×10^{-5} - 2.44×10^{-5} Oe (A^{-1} cm^2) was observed with FeMn thickness in the range of 2 – 5 nm, which is nearly two orders of magnitude larger than that obtained from NiFe/Pt bilayers. The large value is attributed to the small net moment in FeMn. By taking into account the SOT effective field, the experimental observations can be well explained using the macro-spin model by treating FeMn as consisting of two spin sub-lattices. In addition, through the characterization of effective field in NiFe/FeMn/Pt trilayers and analysis based on drift-diffusion formalism, we obtained a spin diffusion length of 2 nm for FeMn. The large SOT effective field and short spin diffusion length in FeMn suggest that it is an effective spin current absorber, which is consistent with previous reports.[1,2]

Secondly, an SMR ratio on the order of 10^{-4} was obtained in FeMn/Pt bilayers, which is comparable to the SMR in NiFe/Pt bilayers. The observation of SMR effect affirms the presence of SOT in the bilayers, since both effects are coming from the spin current and its interaction with FeMn spin sub-lattices. From the Pt thickness dependence of SMR, spin transport parameters in FeMn/Pt bilayer are extracted as follows: θ_{SH} = 0.2, λ_{Pt} = 1.1 nm and Re[G_{MIX}] = 5.5×10^{14} Ω^{-1} m^{-2}. More importantly, it was found that the FeMn thickness dependence of SMR is strongly related to the thickness dependence of net magnetization in FeMn, which is consistent with the extracted thickness dependence of SOT effective field.

Finally, by stacking ultra-thin FeMn and Pt layers into multilayers, we found that global FM order could be realized in these structures with properly chosen thickness combinations. Through systematically varying the thickness of each layer, it was found that the individual Pt layer promotes the FM order by proximity effect from both sides of FeMn, while the uncompensated FeMn layer contributes mainly to the moment of the multilayer. From 2nd order PHE measurements, it was found that the field-like effective field in these structures is about 4 times larger than that of NiFe/Pt with an equivalent FM thickness. The non-zero SOT is attributed to the asymmetry between the top and bottom interfaces. The observation of sizable SMR in the multilayer suggests that the SOT can be understood as being caused by the local generation and absorption of spin current by the ultra-thin Pt and its neighboring FeMn layer, respectively. We have demonstrated that magnetization of the multilayer can be switched reversibly by the current-induced SOT without any external field.

7.2 Recommendations for future work

The results obtained in this work demonstrate that FeMn spin sub-lattices can effectively interact with spin current when it is very thin. Further work may be carried out in the following few aspects.

Firstly, a three-terminal device involving heterostructure of Pt/FeMn/MgO/Pt may be fabricated on Si/SiO_2, similar to the spin-valve-like structure reported in Ref. [3]. In Ref. [3], the IrMn spin configuration is altered through exchange coupling with the bottom NiFe layer through the external field. Here in Pt/FeMn/MgO/Pt, it is possible to rotate the spin sub-lattices of FeMn by the bottom Pt layer through applying an in-plane current. The change of spin configuration can then be read from the tunneling AMR across the stacking direction. As compared to the FeMn/Pt bilayer case, the main advantage of this device is the possibility of obtaining a larger readout signal from tunneling AMR as has been reported in Ref. [3]. Moreover, as mentioned in Chapter 1, the tunneling junctions are more practical for future spintronic devices as compared to metallic junctions.

Secondly, the heterostructure, consisting of Pt/FeMn/FM with reasonable magnitude of exchange coupling between FeMn and FM, may be designed to reduce the critical current density for FM magnetization switching. The consideration is that a giant exchange coupling torque has been recently reported to exist in structures consisting of two antiparallel coupled Co/Ni multilayers separated by Ru.[4] The giant torque can drive the domain walls to move in a very efficient way. In the case of Pt/FeMn/FM here, it is possible that the giant torque also exists at FeMn/FM interface and automatically switches the FM magnetization once the FeMn spin spin-lattices are rotated by Pt. Since a larger SOT effective field is observed in the FeMn/Pt bilayer, the reduction of the FM switching current may be achieved in this heterostructure.

Thirdly, spin valve structures, consisting of $[\mathrm{FeMn/Pt}]_n$ multilayers as FM electrodes, may be fabricated. In principle, the magnetization of multilayer electrodes can be controlled by the in-plane current. In this way, it may be possible to have a spin valve structure with different resistance states that are fully controlled by current.

Finally, the same method of studying FeMn, *i.e.*, the combination of magnetometry measurement and electrical measurements including PHE and ADMR may be applied to other AF materials, such as Cr, IrMn, PtMn, NiO and *etc*. It may be possible to elucidate the spin transport mechanisms and parameters as well in these AFs by use of the techniques and treatments that have already been adopted for FeMn.

References

[1] W. Zhang, M. B. Jungfleisch, F. Freimuth, W. Jiang, J. Sklenar, J. E. Pearson, J. B. Ketterson, Y. Mokrousov, and A. Hoffmann, Phys. Rev. B **92**, 144405 (2015).

[2] P. Merodio, A. Ghosh, C. Lemonias, E. Gautier, U. Ebels, M. Chshiev, H. Béa, V. Baltz, and W. E. Bailey, Appl. Phys. Lett. **104**, 032406 (2014).

[3] B. G. Park, J. Wunderlich, X. Marti, V. Holy, Y. Kurosaki, M. Yamada, H. Yamamoto, A. Nishide, J. Hayakawa, H. Takahashi, A. B. Shick, and T. Jungwirth, Nat. Mater. **10**, 347 (2011).

[4] S. H. Yang, K. S. Ryu, and S. Parkin, Nat. Nanotechnol. **10**, 221 (2015).